Title
Isolated photon-jet correlations in 5.02 TeV Pb-Pb collisions with ALICE

Permalink
https://escholarship.org/uc/item/3k8106pv

Author
Liu, Alwina

Publication Date
2022

Peer reviewed|Thesis/dissertation

Isolated photon-jet correlations in 5.02 TeV Pb–Pb collisions with ALICE

by

Alwina Liu

A dissertation submitted in partial satisfaction of the

requirements for the degree of

Doctor of Philosophy

in

Physics

in the

Graduate Division

of the

University of California, Berkeley

Committee in charge:

Professor Barbara Jacak, Chair
Professor Marjorie Shapiro
Professor Karl van Bibber

Fall 2022

Isolated photon-jet correlations in 5.02 TeV Pb–Pb collisions with ALICE

Abstract

Isolated photon-jet correlations in 5.02 TeV Pb–Pb collisions with ALICE

by

Alwina Liu

Doctor of Philosophy in Physics

University of California, Berkeley

Professor Barbara Jacak, Chair

Jets correlated with isolated photons are a promising channel to study jet quenching in heavy-ion collisions, as photons do not participate in the strong interaction and therefore constrain the Q^2 of the initial hard scattering. We present isolated photon-jet correlations measured in Pb–Pb collisions at $\sqrt{s_{\mathrm{NN}}} = 5.02$ TeV by the ALICE collaboration. We study correlations of isolated photons with $28 < p_{\mathrm{T}} < 40$ GeV/c with charged-particle jets with $p_{\mathrm{T}} > 10$ GeV/c reconstructed with the anti-k_{T} algorithm and report the azimuthal correlation and p_{T} asymmetry. The correlations probe the lowest jet p_{T} range ever measured at LHC energies, and larger modifications due to the QGP are expected in the lower p_{T} regime. We see no trend in the away-side yield with centrality, but do see a change in the distribution of the p_{T} asymmetry consistent with increasing jet energy loss in more central collisions.

Contents

List of Figures

List of Tables

Acknowledgments

There were many people who have helped me accomplish this goal, and it really is important to me that I express gratitude towards them, even briefly. It was a long journey, often difficult, rather pandemic-y, and I couldn't have done it without them.

Thanks to Barbara for your guidance and care throughout this whole time. To the various people in and around the group over these past years, thank you as well for our conversations and discussions and even meetings; I learned a lot from you all: Beatrice, Dhruv, Emma, Ezra, Fernando, Miguel, Minjung, Preeti, Rey, Wenqing, Yue Shi, James, Leo, Mateusz, Nikki, Peter, Raymond, Spencer, Anjali, Tucker, Michael, Adriana, Benjamen, Berenice, Charlie, Cristian, Drew, Erica, Fernando, Ivan, Ivan, Jonas, Jose, Kirill, Kyle, Richard, Stuti, Winston, Youqi, and I hope I didn't forget anyone, but I probably did. I appreciate you too! Particular thanks to Rey for reading and giving feedback on the earliest draft of this thesis.

Thanks to my family and friends for helping to keep me sane through this process in various ways: Grace, Mom, Dad, Troy, Bryce, Becki, Phil, V, Charlie, Sierra, Zack, Kat, Daniel, Megan, Christine, Michael, Stephen, Sola, Logan, Mick, Alec, Rebecca, Paul, Jennet, Patrick, Maria, mosspink, derelyct, SleepyPachirisu, bluecorvus, and other people who I've definitely forgotten to name (sorry!). Thanks also to the various mental health professionals who've helped to keep me sane in other ways: Stephen, Julie, Angelica. Take care of your brain, everyone. You only really get one and it's rather hard to live without it.

Chapter 1

Introduction

Particle physics is the effort to understand the universe in terms of its most fundamental components and their interactions with each other. Our current understanding is encapsulated in the Standard Model of particle physics, which, while known to be incomplete, describes most relevant experimental data [72]. Notable exceptions include neutrino mass and gravity. One way to visualize the Standard Model is Figure 1.1 [47]. It shows the elementary particles, how they are grouped, and how they interact with each other. In this thesis, I will focus on the upper right of Figure 1.1, with quarks and gluons and the strong interaction.
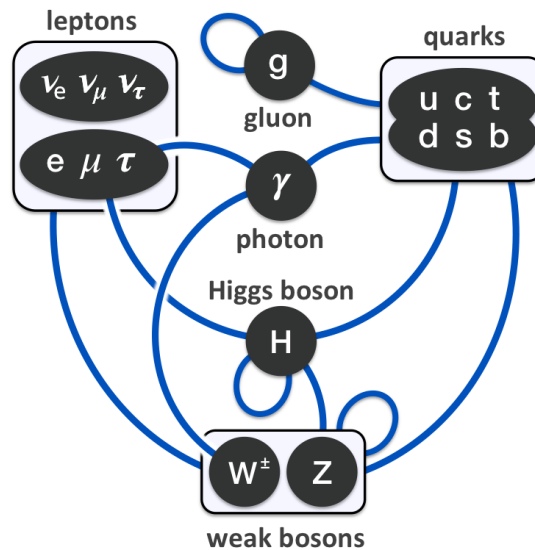
Figure 1.1: A diagram showing the elementary particles and their interactions in the Standard Model. Taken from Ref. [47]

1.1 QCD and the strong interaction

There are four fundamental interactions in particle physics: gravity, electromagnetism, the weak interaction, and the strong interaction. The Standard Model includes the latter three of these; gravity is not included. At a distance of about 1 fm, if the strength of the strong interaction is 1, the strength of electromagnetism is 10^{-3}, the strength of the weak interaction is 10^{-8}, and the strength of gravity is 10^{-37}. However, electromagnetism and gravity can operate at large distances, whereas the weak interaction is short-range because the weak bosons have mass, and the strong interaction is also short-range for reasons I will describe below.

The strong interaction is the fundamental interaction mediated by gluons that affects particles that carry what is known as color charge. It is what holds quarks and gluons together to form protons and neutrons and other hadrons. Only quarks and gluons, collectively called partons, carry color charge, so only they are involved in the strong interaction at the fundamental level. The nucleons in a nucleus are bound together through the exchange of pions and other neutral mesons, which is also due to the strong interaction, overcoming the electromagnetic repulsion of the protons from each other.

There are three color charges known as red, green, and blue; there are also three anti-color charges known as anti-red, anti-green, and anti-blue. Color-neutral combinations of color include blue + anti-blue as well as red + green + blue or anti-red + anti-green + anti-blue. Quarks can come in any of these colors; gluons come in 8 combinations[1] of color and anti-color, following the SU(3) algebra.

Quantum chromodynamics, or QCD, is the quantum field theory that describes the strong interaction. The QCD Lagrangian arises from the requirement of local SU(3) gauge invariance[2] and can be written as

$$\mathcal{L}_{\mathrm{QCD}} = -\frac{1}{4}\sum_a F^a_{\mu\nu}F^{a\ \mu\nu} + \sum_{f=1}^{N}\bar{\psi}\left(i\gamma^\mu\partial_\mu - g\gamma^\mu A^a_\mu\frac{\lambda^a}{2} - m_f\right)\psi. \tag{1.1}$$

f labels the quarks up to the $N = 6$ known quarks; ψ is the fermion (quark) field with mass m_f; A_μ is the gluon field, with a labeling the 8 generators of SU(3) or, equivalently, the 8 different combinations of color and anti-color; g is the coupling of the theory (which will be discussed further); and $F^{\mu\nu}$ is the gluon field strength tensor, which can be written as

$$F^a_{\mu\nu} = \partial_\mu A^a_\nu - \partial_\nu A^a_\mu + g f_{abc}A^b_\mu A^c_\nu, \tag{1.2}$$

---

[1] If the 9th state, a color singlet state that actually has no net color charge, existed, we would have long-range strong interactions the way we have long-range electromagnetic interactions. This would be a rather unpleasant universe for us to live in; the interaction is always attractive, and it is called the "strong" interaction for a reason

[2] We can derive the behavior of the universe by just requiring that we're allowed to freely spin around in space in some particularly funky way. Wild.

where f_{abc} are the structure constants of SU(3).

From this Lagrangian, we can draw the 3 Feynman diagrams representing the fundamental vertices of the strong interaction, shown in Figure 1.2. In standard Feynman diagram notation, straight lines with arrows represent fermions (in this case quarks), helices represent gluons, and wavy lines (which we'll see later) represent photons. The first vertex in Figure 1.2 is the coupling of quarks with a gluon, which is similar to the vertex in quantum electrodynamics (QED) with charged particles and photons. The other two are called the "gluon self-interactions."
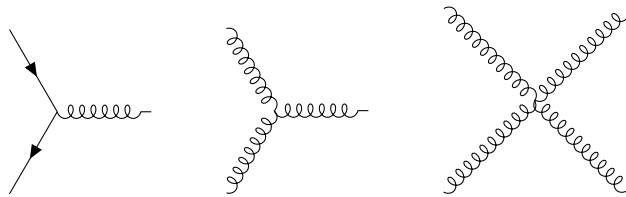
Figure 1.2: Vertices of the strong interaction

Gluons interact with other gluons because they also carry color charge, unlike photons in QED, which are electrically neutral. This gluon self-interaction is the heart of the complexity of QCD. Even in a "simple" quantum field theory like QED, the strength of the interaction depends on the energy scale of interest because of higher-order corrections to the propagator. In QED, this comes only from fermion loops, which causes $\alpha_{\rm EM}$, the strength of the interaction, to increase slightly with increasing energy. Because of the self-interaction of gluons, there are boson loops as well in QCD, which results in drastically different behavior. In QCD, this "running" of the coupling constant can be written as

$$\alpha_s(Q^2) = \frac{4\pi}{\left(11 - \frac{2}{3}N_f\right)\ln\left(Q^2/\Lambda_{\rm QCD}^2\right)}, \tag{1.3}$$

where Q^2 refers to the energy scale of interest, N_f is the number of quarks, and $\Lambda_{\rm QCD}$ is the QCD scale parameter, which is approximately the scale at which QCD switches from a perturbative regime to a non-perturbative regime[3]. Typically, one reports α_s at some particular value of Q^2 instead of a value for $\Lambda_{\rm QCD}$ [82] because one would have to specify a renormalization scheme and the number of active quark flavors, but, for example, in the modified minimal subtraction renormalization scheme with 2 flavors, one can calculate $\Lambda_{n_f=2}^{\bar{MS}} = 261(17)(26)$ MeV [52]. The PDG review [82] has compiled different measurements of α_s at different values of Q^2 into Figure 1.3. We see that the strength of the interaction increases with decreasing energy and vice versa. Note that g from Equations 1.1 and 1.2 and α_s are simply related by $\alpha_s \equiv g^2/4\pi$.

Decreasing Q^2 is equivalent to increasing the distance, so one description of the running of α_s is that the strength of the QCD interaction increases as the distance between two

---

[3]It's not quite such a hard cutoff in real life, but it's a decent way to think about it
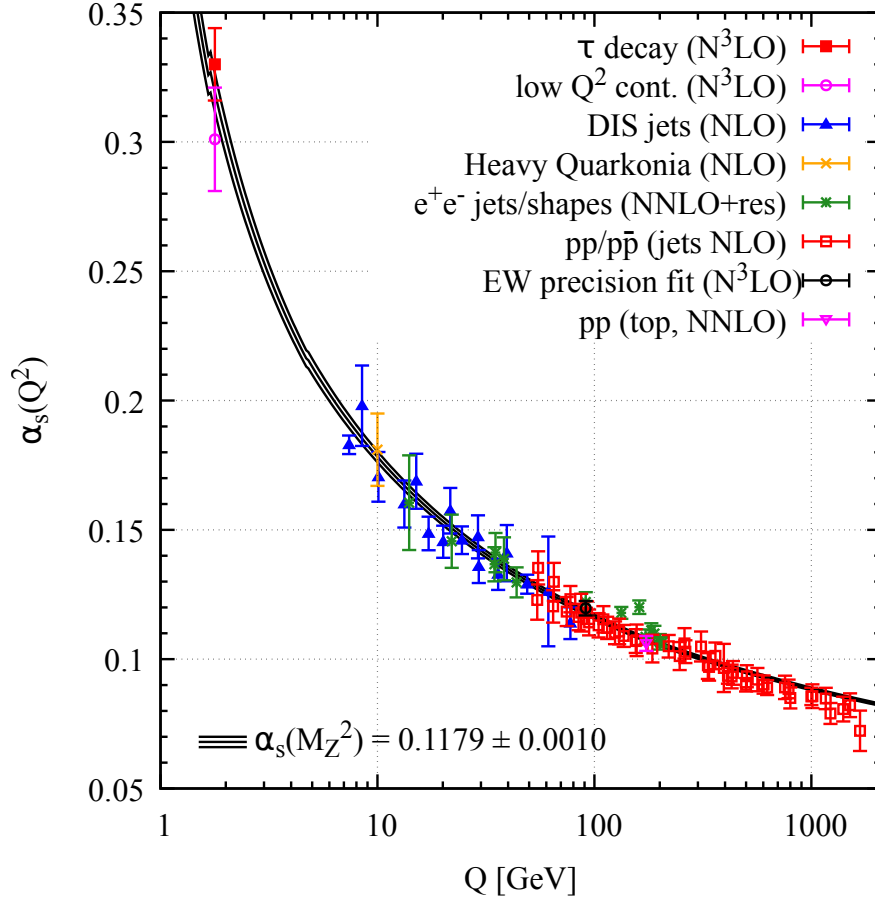
Figure 1.3: Measurements of α_s as a function of Q and the subsequent fit. Taken from Ref. [82]

partons increases. This increase in α_s with increasing distance helps explain the concept of confinement, which says that all observed particles are color neutral. If we imagine that we take two partons and try to separate them, as we increase their distance, we increase the strength of the QCD interaction between them. At a distance of about 1 fm, it becomes more energetically favorable for a quark-antiquark pair to pop out of the vacuum than to continue to allow the distance between those partons to increase. Everything we have observed so far is consistent with confinement (e.g. we've never observed a free quark or a disallowed hadronic state), but so far there is no analytical proof of color confinement [72].

A collision between electrons, protons, ions, or some combination thereof can produce initially free partons; for example, an electron-positron collision can produce a quark-antiquark pair traveling back-to-back in the center-of-mass frame ($e^+e^- \rightarrow q\bar{q}$). We do not observe these free partons; instead, if the initial momenta of the partons are large enough, we observe jets, which are collimated sprays of particles associated with those initial partons. The

process by which the parton turns into hadrons is known as hadronization, a process that is poorly understood as of now from a first-principles perspective, but can be described reasonably well with phenomenological models tuned to data. For example, in the Lund string fragmentation model [4], as two partons move away from each other, the color field lines get compressed into a tube with a "string" constant, which is the amount of energy per unit length (much like the spring constant in a spring). As the string elongates and the energy between them grows, it eventually "breaks" via the production of a $q\bar{q}$ pair. This continues until the strings stop breaking and hadrons are formed from the resulting quarks. In the coalescence model, partons near each other in phase space (position and momentum) combine to form hadrons.

Ideally, we would be able to exactly reconstruct the kinematics of a parton by reconstructing a jet, but unfortunately, this is not achievable. In collisions with few final-state particles, one could look at pictures and essentially group together some particles by eye. In practice, that is impractical and imprecise, so we use jet finding algorithms. These algorithms need to accomplish several goals: they need to define how particles get grouped together and how the kinematics of the grouped particles should be used to determine the kinematics of the jet [65]. They should also be infrared and collinear (IRC) safe; this means that particles traveling in the same direction (collinear) and extremely low-energy (infrared) particles should not affect the jet that gets reconstructed [65]. Different jet finding algorithms reconstruct the parton kinematics with varying levels of success, but without these kinds of well-defined algorithms, it would be very difficult to make any comparisons among different experiments and theory calculations, since we could not be certain that we were comparing identical objects with the same expected properties [58].

There are a number of jet-finding algorithms; in heavy-ion collisions, the most common one is the anti-k_T algorithm [16] with E-scheme recombination. This recombination scheme means that whenever particles are grouped together, their 4-momenta are summed to get the 4-momentum of the combined object. The anti-k_T algorithm is part of a class of algorithms known as sequential recombination algorithms. In these algorithms, one defines a distance metric d_{ij} between two entities (particles or pseudojets) i and j, as well as a distance metric d_{iB} between the entity i and the beam B. These distances can be written as follows:

$$d_{ij} = \min(k_{ti}^{2p}, k_{tj}^{2p})\frac{\Delta_{ij}^2}{R^2}, \tag{1.4}$$

$$d_{iB} = k_{ti}^{2p}, \tag{1.5}$$

with k_{ti} the transverse momentum of the ith entity and $\Delta_{ij}^2 = (\Delta y_{ij})^2 + (\Delta\varphi_{ij})^2$ the distance in rapidity-azimuth space between the two entities. The parameters that define the algorithm are the resolution parameter R and a power parameter p. $p = 1$ is known as the k_T algorithm, $p = 0$ is known as the Cambridge-Aachen algorithm, and $p = -1$ is known as the anti-k_T algorithm. To form jets, one calculates all d_{ij} and d_{iB} for all pairs of particles (i, j) and all particles i. Then one starts with the smallest d. If the smallest d is a

d_{ij}, the two entities are combined (using the chosen recombination scheme) into a pseudojet and all the d_{ij} and d_{iB} distances are recalculated. If the smallest d is a d_{iB}, i is declared to be a jet and removed from the list of entities. This continues until there are no more entities and everything has been clustered into a jet. This means that it is entirely possible to have 1-particle jets. R, sometimes called the "jet radius," essentially sets the maximum size of the jet. The anti-k_{T} algorithm essentially starts with the highest-k_{T} particles first and successively groups together softer and softer particles.

Jet algorithms, while extremely useful, rarely if ever produce an object that exactly matches the initial parton. This means that the jet kinematics are only an approximation of the parton kinematics. Also, in some kinds of collisions, there are can be a lot of particles that did not arise from the process that produced the initial parton that will get clustered into the jet. Various mitigation techniques can be used to remove this contribution from the final jet kinematics; these include the jet area/median method [19] (used in this thesis), constituent subtraction [9] and its iterative version [8], and even machine learning approaches. Furthermore, sometimes only the charged particles in an event will be used for jet reconstruction; these are called charged-particle jets or charged jets.

As we see in Figure 1.3 and Equation 1.3, as we increase Q^2 (and therefore decrease the distance), α_s gets smaller and eventually goes to 0. This property is known as asymptotic freedom: the theory asymptotically becomes a free theory (i.e. no interactions) as the energy scale goes to infinity and the distance goes to 0. This means that at sufficiently high Q^2, α_s is small enough to do perturbation theory. At LHC energies, it is still large enough ($\alpha_s \sim 0.1$) that higher-order corrections are nontrivial, but it is at least possible, if difficult, to do calculations in perturbative QCD (pQCD) in this regime. These higher-order corrections can cause there to be more partons in the final state or can appear as virtual loops in the Feynman diagrams; by including higher-order corrections, more accurate calculations can be done. While pQCD is a powerful tool, it cannot be used to describe everything[4], even when α_s is small. Furthermore, there are regimes in which α_s is small in which some very interesting things happen.

1.2 Quark-gluon plasma

At very high temperatures and/or densities, hadrons can melt into a state of matter known as the quark-gluon plasma (QGP), a state of deconfined quarks and gluons. Figure 1.4, taken from Ref. [60], shows a somewhat simplified view of the QCD phase diagram, where we see that, under "normal" conditions, we have confined hadrons, but in more extreme circumstances, we instead have a QGP. At these high energies and small distances, asymptotic freedom means that the coupling between the partons (i.e. α_s) is very small; eventually, when α_s gets small enough, we should see a weakly-interacting gas of quarks and gluons. We have not yet reached high enough temperatures to see this weakly-interacting gas; instead, the QGP that we observe is a strongly-coupled liquid.

---

[4]Well, maybe it can, but we're not good enough at it yet.
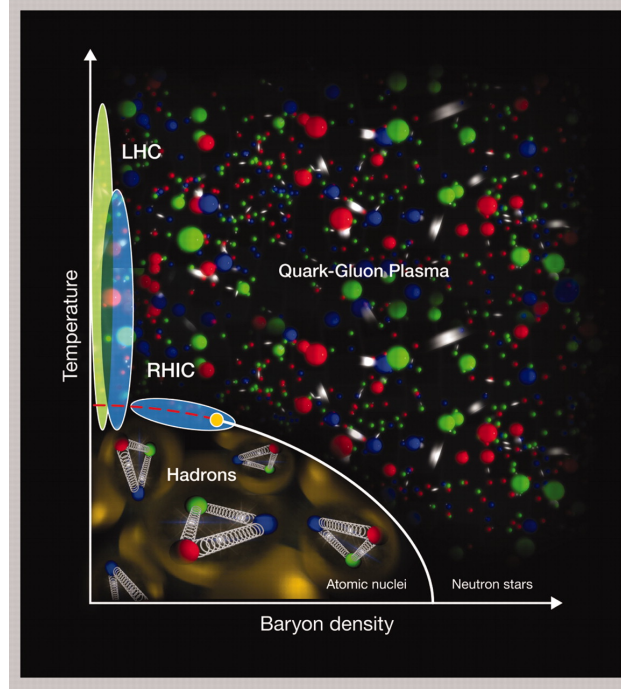
Figure 1.4: A simplified view of the QCD phase diagram. Taken from Ref. [60]

QGP is often described as a near-perfect fluid; this refers to the fact that it has an extremely low shear viscocity, or more specifically, a very low ratio of shear viscocity to entropy density, η/s. This is to say that the quarks and gluons flow past each other with very little friction, there is very little dissipation of energy in the fluid, and momentum can be transported over large distances [15]. This conclusion that QGP is a strongly coupled liquid is drawn somewhat indirectly from the fact that all of our measurements are consistent with the formation and evolution of a relativistic hydrodynamic fluid [15]. In particular, measurements of azimuthal correlations and their evolution with a number of parameters are consistent with the description of a strongly coupled liquid with very low η/s [15].

Azimuthal correlations have been extensively studied because they have a clear and interesting structure. In particular, in a relativistic hydrodynamic fluid, initial spatial anisotropies cause there to be pressure gradients that turn into momentum anisotropies in the final state [15]. This collective behavior is known as collective flow, and it is often quantified in terms of the coefficients v_n of the Fourier expansion of the angular distribution:

$$\frac{\mathrm{d}N}{\mathrm{d}\varphi} \propto 1 + 2\sum_{n=1}^{\infty} v_n \cos[n(\varphi - \Psi_n)], \tag{1.6}$$

where N is the number of particles and Ψ_n is the nth-order event plane, which can be thought of as being related to the direction of the flow in that event and is randomly oriented

on an event-by-event basis [55].

The most frequently studied of these coefficients is v_2, known as elliptic flow. Since it arises from the overlap region being "almond-shaped," v_2 is small for the most central events; it is also smaller for more peripheral events, as they have fewer particles. It can be extracted from measurements of 2-particle correlations, and has been measured for a variety of particle types, across different transverse momentum (p_T) ranges and centrality (described in the next section) ranges, in different collision systems at different energies. From the measured v_n, within the framework of relativistic hydrodynamics, one can extract η/s, and for small values of η/s, hydrodynamics can generally reproduce the measured data well. For more about collective flow, see Ref. [55].
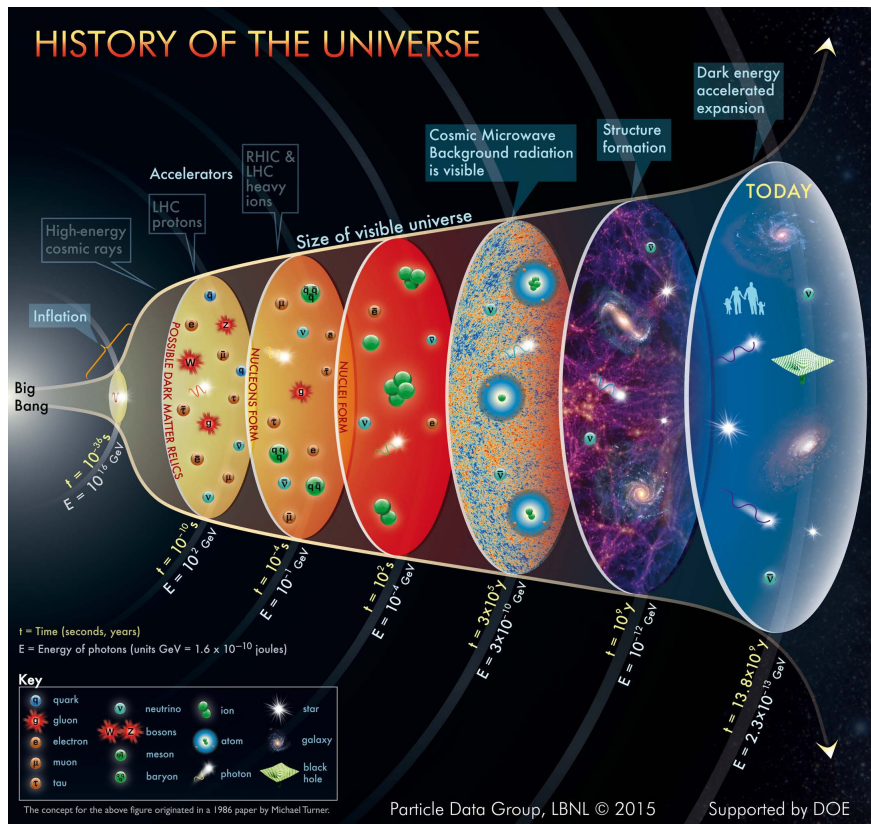
Figure 1.5: Cartoon of the history of the universe with information about the universe at various times after the Big Bang. Taken from Ref. [57]

From somewhere around 10^{-6} to around 10^{-4} s after the Big Bang (see Figure 1.5), while the universe was still too hot for hadrons (or nuclei) to form, it consisted of quark-gluon plasma. However, due to the nature of the phase transition between QGP and hadronic matter, there are no cosmological remnants that would allow us to directly observe the

primordial quark-gluon plasma [15]. Therefore, in order to study QGP and better understand the evolution of the universe, we turn to relativistic heavy-ion collisions.

Heavy-ion collisions

When two nuclei are accelerated to relativistic speeds and collide with each other, a quark-gluon plasma can be formed. The QGP subsequently evolves and expands as a hydrodynamic fluid before hadronizing into what is eventually a free-streaming hadron gas. The stages of a heavy-ion collision are shown in Figure 1.6, which is taken from the BNL page on The Physics of RHIC, which, at the time of writing, is at `https://www.bnl.gov/rhic/physics.php`. Just before the collision (panel 1), in the center-of-mass frame, each nucleus is a Lorentz-contracted disk with a diameter of about 14 fm (for a Pb nucleus), where both the locations of the nucleons in the nucleus and the location of the partons in the nucleons fluctuate from event to event. During the collision, extremely large color fields interact with each other (panel 2) and the quarks and gluons are freed (panel 3). Shortly after the collision, the quark-gluon plasma is formed (panel 4) and evolves hydrodynamically as a relativistic fluid. It expands and cools until it drops below a temperature of about 155 MeV, called the critical temperature, which is when hadrons are formed and the quarks and gluons are no longer free. This same temperature is also the threshold called chemical freeze-out, where inelastic collisions among hadrons end and thus the types of hadrons in the event are fixed; in principle the critical temperature and chemical freeze-out temperature do not have to be the same. The hadrons continue to elastically scatter off each other as this gas continues to expand and cool, until it drops below a temperature of about 95 MeV, a threshold called thermal freeze-out, which means that the hadrons stop scattering off each other and continue in straight-line paths. These hadrons (and leptons and photons) that were created in the collision are measured by various detector systems, and it is from these measurements that we can reconstruct information about the formation and evolution of the QGP.

At a collider like the Large Hadron Collider (LHC) at CERN in Geneva, Switzerland or the Relativistic Heavy Ion Collider (RHIC) at Brookhaven National Lab in Upton, NY, USA, we can control two aspects of the collision: the ion species (with the heaviest being Pb at the LHC and Au at RHIC) and the energy of the beam (usually quoted as the per-nucleon-nucleon center-of-mass energy, $\sqrt{s_{\mathrm{NN}}}$, or in a proton-proton collision, just $\sqrt{s}$). One important thing we cannot control is the impact parameter, which is how close the center of the nuclei are to each other when they collide.

In heavy-ion collisions, the amount of overlap is estimated via a quantity known as centrality, which ranges from 0 to 100 percent, where 0% are the most central collisions (the most overlap) and 100% are the most peripheral collisions (the least overlap)[5]. This percentage refers to the fraction of the total interaction cross section; for example, a 0-10% centrality bin refers to the 10% of the cross section with the largest overlap. Larger

---

[5]"Peripherality" is therefore a more accurate term, but so it goes. For more confusion, "higher centrality" refers to smaller values, e.g. 0-10%.
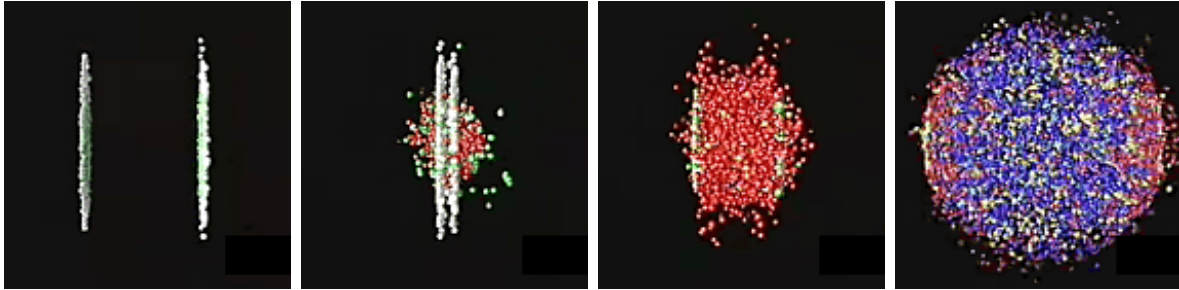
(a) Just before the ions collide, they are Lorentz contracted

(b) The ions collide with each other, during which extremely large color fields interact

(c) The quarks and gluons are freed

(d) The liquid QGP is created

Figure 1.6: Cartoon of the stages of a heavy ion collision from just before to the collision to the beginning of the formation of the QGP. Taken from the BNL page on The Physics of RHIC (see text for link)

overlap means more nucleon-nucleon interactions, which leads to events with more particles (higher multiplicity). Experimentally, centrality is determined by measuring the multiplicity of events, doing a fit, and dividing the result into bins. The fit comes from Glauber modeling of nuclear collisions [64], which is used to understand geometric aspects of collisions. This will be discussed in more detail in Section 2.2. There are also ultra-peripheral collisions, where the nuclei do not interpenetrate at all (the distance between the center of the nuclei is greater than twice the radius) while their electromagnetic fields do interact; I will not discuss them here.

In a heavy-ion collision, the interaction of the nuclei can be thought of in terms of interactions between the nucleons, with more central collisions having more nucleon-nucleon collisions. Within each nucleon-nucleon collision, we can further think of it in terms of a parton-parton interaction. A nucleon can be described in terms of parton distribution functions (PDFs), which give the probability that a given type of parton will carry a particular fraction of the total nucleon momentum; this fraction is known as Bjorken x or just x [72]. A nucleon-nucleon interaction can then be thought of as the interaction between two partons, each randomly determined by the nucleon PDF with some momentum fraction x. A nuclear PDF, or nPDF, describes the PDF of the collection of nucleons in a nucleus, which is not exactly the same as a superposition of the individual nucleon PDFs. PDFs are not calculable and have to be extracted from fits to experimental results. For more about PDFs, see Ref. [49].

Once in a while, a collision will result in an event in which two partons undergo a "hard scattering," leading to the production of particles at large angles from the beam direction with large transverse momentum ("hard" refers to high momentum transfer, or high Q^2).
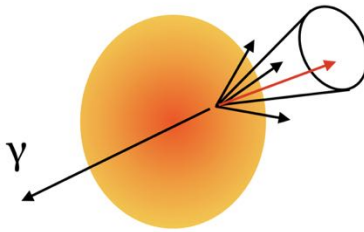
Figure 1.7: Cartoon depicting a photon-jet event (the arrows) within a QGP

While rare, these interactions are important because they happen in the very early stages of the collision and their products therefore traverse the evolving QGP produced by the rest of the event[6] as depicted in Figure 1.7. The high-p_T objects produced in these hard scatterings are known as "hard probes," and they include high-p_T jets, high-p_T hadrons, heavy quarks, and electroweak bosons, since it takes a high-energy scattering to produce these objects. For this analysis, I will focus on two types of objects: photons and jets.

Photon-jet correlations

Photons are produced throughout the lifetime of a heavy-ion collision via various mechanisms. Neutral mesons can decay into photons; these are called decay photons. Non-decay photons are collectively called direct photons, and they can be produced in a number of ways. The hot QGP can radiate photons as it cools; these are called thermal photons. Charged particles can radiate a photon via bremsstrahlung; these are called bremsstrahlung photons. As a parton fragments into a jet, it can produce a photon (also via bremsstrahlung, but this is specifically within a jet); these are called fragmentation photons [6]. Photons can be produced in a hard scattering; these are called prompt photons. In this thesis, I focus on this last category of photons, the prompt photons.

At leading order, there are two Feynman diagrams that result in a photon being produced back-to-back with a jet. These are shown in Figure 1.8, with QCD Compton scattering on the left and quark-antiquark annihilation on the right. These processes lead to quark- and gluon-initiated jets, respectively. At LHC energies, which reach small values of x, gluons dominate the parton distribution function, as seen in the rightmost panel of Figure 1.9. This dominance of gluons in the small-x regime comes from gluon emission and splitting, which is more likely to happen at smaller energies. This means that the dominant leading-order process is QCD Compton scattering, so the final-state jets tend to be initiated by quarks.

There are many higher-order processes that also contribute to photon-jet events, but in general, photon-tagged jets are quark-enriched. These higher-order processes can, for example, cause the final state to have two jets and a photon; more generally, in higher-order

---

[6]Some will argue that there is no "rest of the event," and it's true that these are not truly separable, especially once we're looking at what's in the detectors, but it's useful to think of it this way
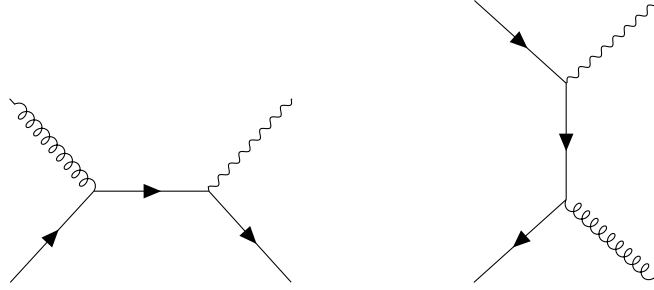
Figure 1.8: Leading-order Feynman diagrams for photon-jet production. Left: QCD Compton scattering. Right: quark-antiquark annihilation
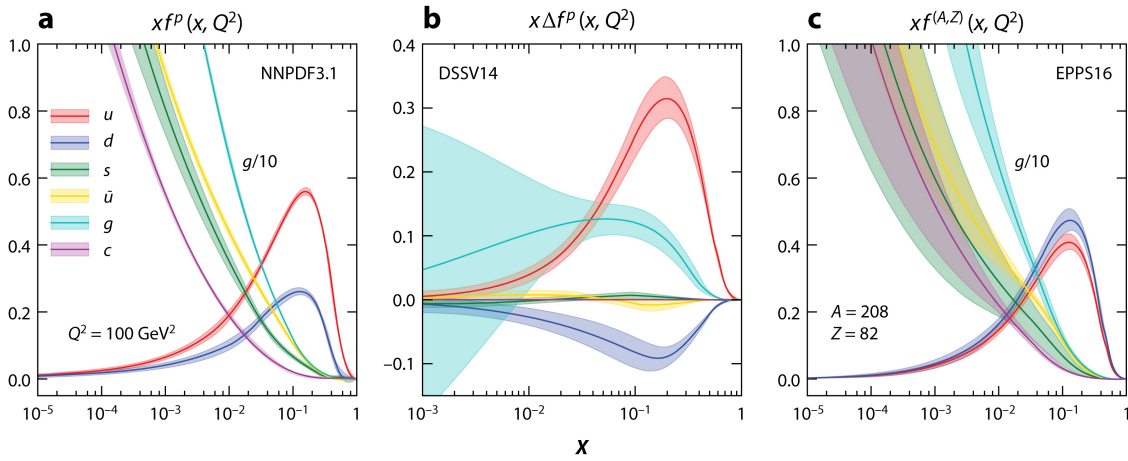
Figure 1.9: Parton distribution functions for unpolarized protons (a), polarized protons (b), and lead nuclei (c). Taken from Ref. [49]

processes, the photon and jet are no longer produced back-to-back with the same momentum. However, at sufficiently high Q^2, α_s is small enough that these higher-order processes are subdominant, if still nonnegligible (for example, at $Q \sim 20$ GeV, $\alpha_s \sim 0.15$).

By examining events where a photon is produced back-to-back with a jet, we can do relatively controlled studies of jet quenching, a set of phenomena in which jets lose energy while traversing the QGP with that energy being redeposited in the medium. Since we only observe the final-state jet, not the initial parton immediately after the hard scattering, in principle we can't know how much energy the jet had before going through the medium. By measuring the direction and p_T of the photon, we constrain the initial direction and p_T of the jet. At leading order, in the center-of-mass frame, the photon and jet are produced back-to-back with the same momentum and the photon does not participate in the strong interaction

and is therefore essentially unaffected by the QGP. Even in higher-order interactions, the initial kinematics of the jet are constrained by the kinematics of the photon. With this estimate of the initial jet p_T from the photon p_T, we can better determine how much energy a jet (or the parton from which it came) loses as a result of interactions with the medium.

As early as 1986 [5, 11], it was predicted that jets scattering as they travel through a QGP should result in the modification of the acoplanarity distribution. In other words, in a situation where a dijet (two back-to-back jets) is produced by a hard scattering, the angle between the dijets (and the amount that differs from being back-to-back) was predicted to be modified by the QGP. Replacing one of the jets with a photon would somewhat change the calculation, since the photon experiences minimal scattering in the QGP, but we still might expect that the opening angle between the photon and jet could be modified by the QGP. It is more straightforward to see that the distribution of the momentum balance between the jet and photon will be shifted by the effects of the QGP; we expect jets to have less energy than the corresponding photon.

Medium-induced energy loss can happen through collisional energy loss as the parton bounces off of the partons in the QGP, or it can happen through radiative energy loss, where the parton radiates a gluon. Radiation can also be induced by collisions, so these are not fully independent mechanisms [7]. Radiative energy loss is the dominant form of energy loss for high-energy partons, and it can be understood in terms of the jet transport coefficient, usually called $\hat{q}$ [21] and defined as "the averaged transverse momentum broadening squared per unit length," $\hat{q} \equiv \langle k_T^2 \rangle / L$.

There are a number of models that seek to describe the energy loss of partons as they traverse the QGP. The more complete models also take into account the reaction of the plasma to the partons, since energy loss must be balanced by energy gain somewhere else[7] in what is sometimes called energy redeposition or jet-induced medium response. This energy is deposited along the trajectory of the hard parton, so the thermalization of the deposited energy causes a change in the hydrodynamic evolution of the QGP, leading to a structure sometimes called the "Mach cone," as it is reminiscent of a sonic boom [24]. However, for such a structure to be visible, there must be significant energy deposited into the medium in the jet quenching process.

Some ways in which models of medium-induced jet energy loss differ include:

- How inelastic energy loss is calculated, and under what assumptions

- How the parton splittings are modified in the medium; this can be roughly broken down into two categories, namely directly modifying the splitting function (e.g. MATTER [20] does this) or modifying the parton kinematics between vacuum-like splittings (e.g. JEWEL [78, 79] does this)

---

[7]otherwise we would live in a very different kind of universe

- Whether and how the medium response is simulated; this may be through some kind of viscous hydrodynamical model (e.g. MARTINI [66]) or some kind of full Boltzmann transport of both jet and medium partons (e.g. AMPT [61])

  - Whether and how "recoil partons," which were partons that were originally part of the thermal background that got scattered into the final state by the jets, are handled, including whether they are allowed to rescatter with the rest of the medium

  - Whether and how "negative partons," which are the holes in the phase space left behind by the recoil partons, are handled

For example, the CoLBT-hydro model [22, 25] involves both Linear Boltzmann Transport (LBT) [75, 54] and a hydrodynamical model. LBT starts with a linear version of the Boltzmann transport equation, which statistically describes the behavior of a non-equilibrated thermodynamic system. LBT is a Monte Carlo (MC) simulation where the propagation of partons and the medium excitation are simulated according to this linear Boltzmann equation. There are different parton phase-space distributions before and after scattering within a medium of some temperature and fluid velocity. The scattering probability is based on the parton scattering cross section and the local medium density. The probability of collision-induced radiation is calculated and included as well.

In CoLBT-hydro, LBT is combined with a 3+1D viscous hydrodynamic model to simultaneously simulate the parton transport and evolution of the thermal medium, with the coupling done at each time step. It can therefore be used to simulate events in which a photon and a jet are produced in a hard scattering, and to predict distributions of the correlations between them after traveling through a QGP.

In measuring photon-jet correlations across different collision systems, kinematic ranges, jet definitions, etc., as well as other types of measurements of jet quenching, one of our goals is to distinguish between the different models of jet quenching and to begin to determine what approaches to jet energy loss are appropriate. It is through comparison with data that we are able to gain insight into the interplay and strength of the various energy loss mechanisms and to ultimately learn about the QGP and QCD as a whole. For example, when it comes to extracting $\hat{q}$ from a model, the approach is generally to constrain model parameters with the data and then to evaluate or directly extract $\hat{q}$ from that model. By narrowing down which models accurately predict the behavior in the data, we can perhaps come to an extraction of the actual $\hat{q}$ of the QGP produced in nature.

In order to measure the correlation between prompt photons and the jets produced in the same hard scattering, we tend to measure isolated photon-jet correlations. "Isolated" photons are photons that are surrounded by little to no hadronic activity. This increases the likelihood of selecting on a prompt photon, as decay and fragmentation photons tend to be produced within a jet and therefore tend to be surrounded by a lot of hadronic activity.

There have been a couple of published measurements of isolated photon-jet correlations in 5.02 TeV Pb–Pb collisions at the LHC. CMS published their measurement in 2018 [40]

for photons with $p_\mathrm{T} > 40$ GeV/c and jets with $p_\mathrm{T} > 30$ GeV/c. They found no evidence of broadening in the azimuthal correlations and a decrease in the ratio $p_\mathrm{T}^\mathrm{jet}/p_\mathrm{T}^\gamma$ in Pb–Pb collisions relative to a pp reference. ATLAS published their measurement in 2019 [36] for photons with $63.1 < p_\mathrm{T} < 200$ GeV/c and jets with $p_\mathrm{T} > 31.6$ GeV/c. They also found that the $x_{J\gamma} = p_\mathrm{T}^\mathrm{jet}/p_\mathrm{T}^\gamma$ distribution was modified in Pb–Pb collisions relative to pp collisions, with more modification for more central collisions. CMS and ATLAS have both further explored properties of these photon-tagged jets, studying the fragmentation function [39, 35] and jet shapes [38]. Because jet quenching is a well-established phenomenon, when we measure photon-jet correlations in ALICE, we should also expect to see similar effects to CMS and ATLAS, namely a shift towards lower $p_\mathrm{T}^\mathrm{jet}/p_\mathrm{T}^\gamma$ in Pb–Pb collisions relative to a pp reference.

In this thesis, I present a measurement of isolated photon-jet correlations in 5.02 TeV Pb–Pb collisions at the LHC with the ALICE detector. Similar to CMS and ATLAS, we measure the azimuthal correlations and the transverse momentum asymmetry. However, we are able to measure lower-p_T photons and jets, namely photons within $28 < p_\mathrm{T} < 40$ GeV/c and charged-particle jets with $p_\mathrm{T} > 10$ GeV/c. The rest of the thesis is structured as follows: Chapter 2 describes the LHC and the ALICE experiment, Chapter 3 details the analysis, Chapter 4 presents the results, and Chapter 5 compares the results to calculations and the other experimental results and discusses their implications.

Chapter 2

Experiment

2.1 LHC

The Large Hadron Collider (LHC) at CERN is the world's largest and most powerful accelerator, designed to collide protons at up to $\sqrt{s} = 14$ TeV. It sits in an underground tunnel with a circumference of 27 km under both France and Switzerland near Geneva. While the LHC is usually used as a proton collider, one or both beams can be replaced by nuclei as well. In most years when the LHC is operational, the collider is configured with the goal of studying heavy-ion collisions for about a month out of the year. These configurations have included Pb–Pb collisions as well as p–Pb collisions, Xe–Xe collisions, and pp collisions at specific center-of-mass energies used as references for the ion collisions.

In order to study nature at the smallest scales, we have to go to higher energies, as dictated by the de Broglie wavelength $\lambda = h/p$. Accelerators allow us to collide particles at near-light speed, allowing us to study things at very small scales (like subatomic particles) and also to potentially discover new particle states (like the Higgs boson). Colliding beams allow us to reach significantly higher center-of-mass energies than fixed-target experiments, so in order to study the highest-energy collisions, one has to go the largest circular collider, which is the LHC at CERN. In the heavy-ion collisions used to study the QGP, a higher center-of-mass energy produces a hotter plasma.

To actually create such high-energy beams, protons (or nuclei) go through a series of accelerators, each of which increases the energy of the particles, before being injected into the LHC itself. A schematic with the various stages (LINAC, BOOSTER, PS, SPS, LHC), along with many non-LHC accelerator experiments at CERN, is shown in Figure 2.1, taken from Ref. [62]. Proton beams start in LINAC 4, where the hydrogen atoms are initially accelerated and stripped of their electrons before being injected into the PS Booster. Pb beams start in LINAC 3 as vaporized lead and are collected and accelerated in the Low Energy Ion Ring (LEIR). From either the PS Booster or the LEIR, the beams are injected into the PS (which brings proton beams up to 26 GeV), the SPS (which brings proton beams up to 450 GeV), and finally the LHC, where they are slowly brought to the intended collision

energy over the course of about 20 minutes. In the case of ion beams, there are stripper foils between each accelerator to remove ever more electrons from the atoms.

The beams, which are actually discrete bunches, go around the LHC for many hours at a time, colliding at a frequency of about 40 MHz, or 25 ns between collisions. In each collision, the beams are brought to pass through the same space. However, protons are very very small, so most of the protons in a bunch will not interact in a given bunch crossing. Over time, the beam intensity degrades due to intra-beam scattering among the charged particles in the beam, which causes the beams to broaden and reduces the collision probability. Eventually, the beam no longer produces good collisions; typically, this takes on the order of 8 hours. In Pb ion beams, in which each particle has a much larger charge than a proton, this degradation happens faster. At this point (or in the case of some kind of problem or emergency), the beam is dumped, its energy safely deposited into a very large block of graphite and other materials, and the accelerator complex is ready to start the whole procedure over again.

At the LHC, the beams are collided at 4 interaction points, each of which houses a large detector experiment[1]. These are ATLAS (A Toroidal LHC Apparatus) [37] at Point 1, ALICE (A Large Ion Collider Experiment) [32] at Point 2, CMS (Compact Muon Solenoid) [41] at Point 5, and LHCb (LHC beauty) [42] at Point 8. The relative positions of these can be seen in Figure 2.2.

---

[1]There are actually more than 4 detector experiments at the LHC; the smaller ones share an interaction point with one of the large ones.
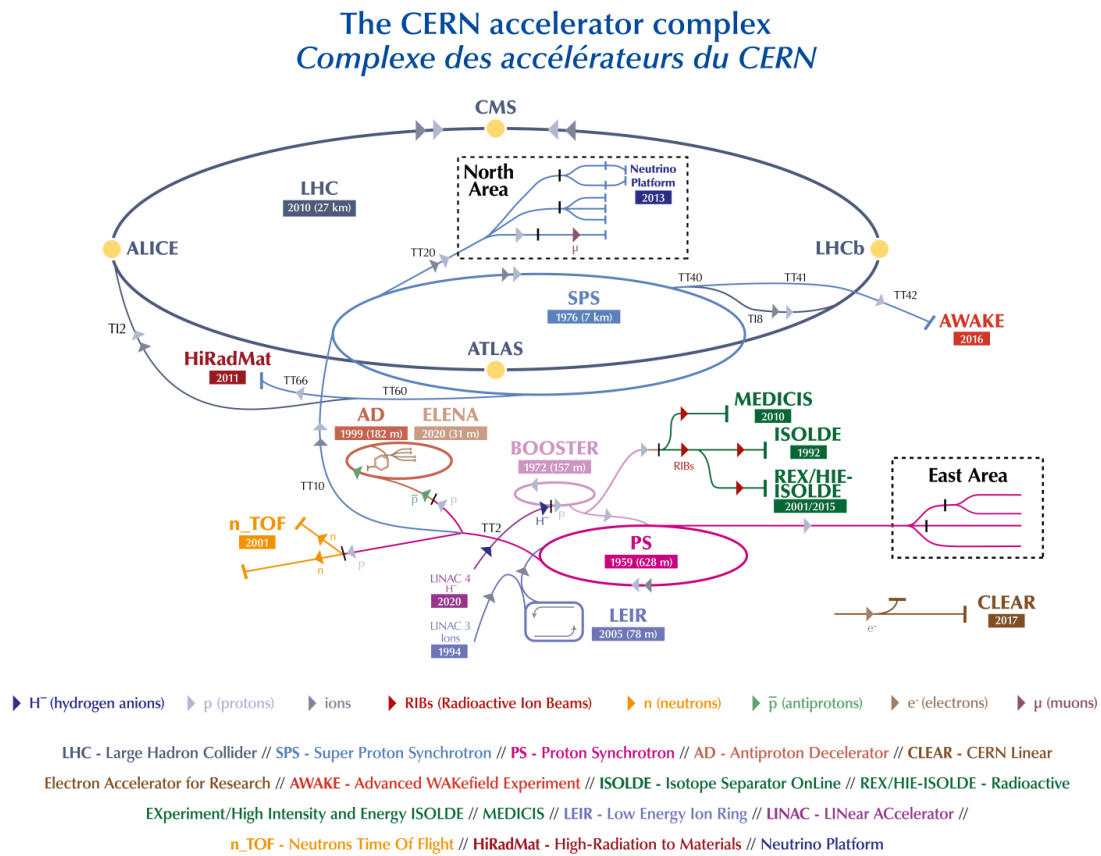
Figure 2.1: A schematic view of the CERN accelerator complex. Taken from Ref. [62]
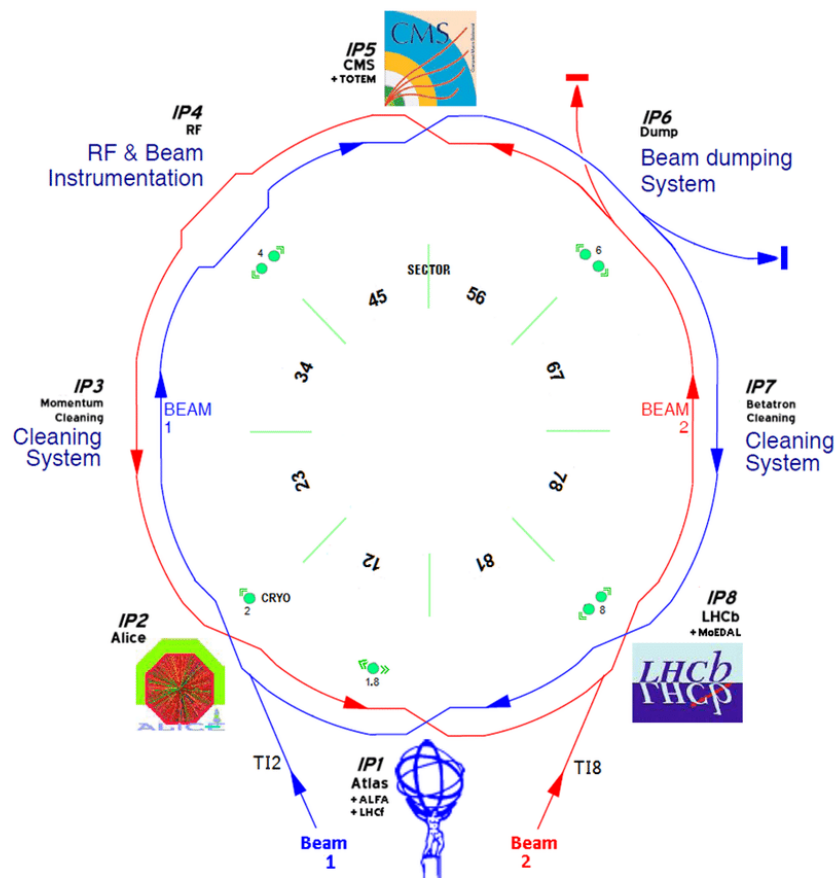
Figure 2.2: A schematic view of the Interaction Points at the LHC. Taken from Ref. [77]

2.2 ALICE

ALICE is dedicated to heavy-ion physics. Figure 2.3 shows a schematic view of the many sub-detectors that made up ALICE during Run 2, the time period during which the data for this analysis were taken. Run 2 began in 2015 and ended in 2018. After Run 2, there was a long shutdown period (Long Shutdown 2, or LS2) during which ALICE underwent a number of upgrades to various sub-detector systems in preparation for Run 3. However, for the sake of consistency, I will describe the detector as it was in Run 2 in the present tense. A full description of the ALICE detector can be found in Ref. [32] and a full description of the ALICE detector performance can be found in Ref. [31].

ALICE was designed to explore and measure a wide range of observables in heavy-ion collisions, which led to a number of design considerations. The original design of ALICE was optimized for extremely high multiplicity, $\mathrm{d}N / \mathrm{d}\eta = 8000$ (in reality, this number is closer to 2000 for the highest-multiplicity events), and this was the strongest constraint in the design process. Within this high-multiplicity environment, the detector was designed to provide good momentum resolution and particle identification over a large momentum range. One consequence of this decision is a relatively slow overall interaction rate, due to use of slow sub-detectors such as high-granularity detectors that use the drift time of particles in an electric field.

The ALICE coordinate system is defined such that the z-axis is parallel to the beam, the x-axis points towards the center of the accelerator ring, and the y-axis points straight up. The conversion to cylindrical coordinates (r, φ) from (x, y) is the standard one. We also use the pseudorapidity η, which is defined in terms of the polar angle θ as

$$\eta \equiv -\ln\left(\tan\frac{\theta}{2}\right), \tag{2.1}$$

which means that $\eta = 0$ is perpendicular to the beam axis and increasing values of η correspond to directions that are increasingly parallel to the beam axis.

ALICE can be divided into two regions: the central barrel, covering $|\eta| < 0.9$, and the forward (and backward) detectors covering much higher $|\eta|$. The detectors in the central barrel are enclosed in a solenoidal magnet (the big red shell labeled "L3 magnet" in Figure 2.3), which creates a magnetic field of up to 0.5 T parallel to the direction of the beam. Of the 20 or so ALICE sub-detectors, we use only a handful in this analysis: the Inner Tracking System (ITS), the Time Projection Chamber (TPC), the Electromagnetic Calorimeters (EMCal and DCal), and the VZERO system (V0). I will describe each in detail in the next few sections.

L3 magnet

The central barrel is enclosed by a large solenoidal magnet capable of producing a field of up to 0.5 T parallel to the beam line (in the z-direction). This magnet was previously used by the L3 experiment at the Large Electron-Proton Collider (LEP), which were the previous occupants of Point 2 and the LHC ring, respectively [32, 71, 77]. The field variations are
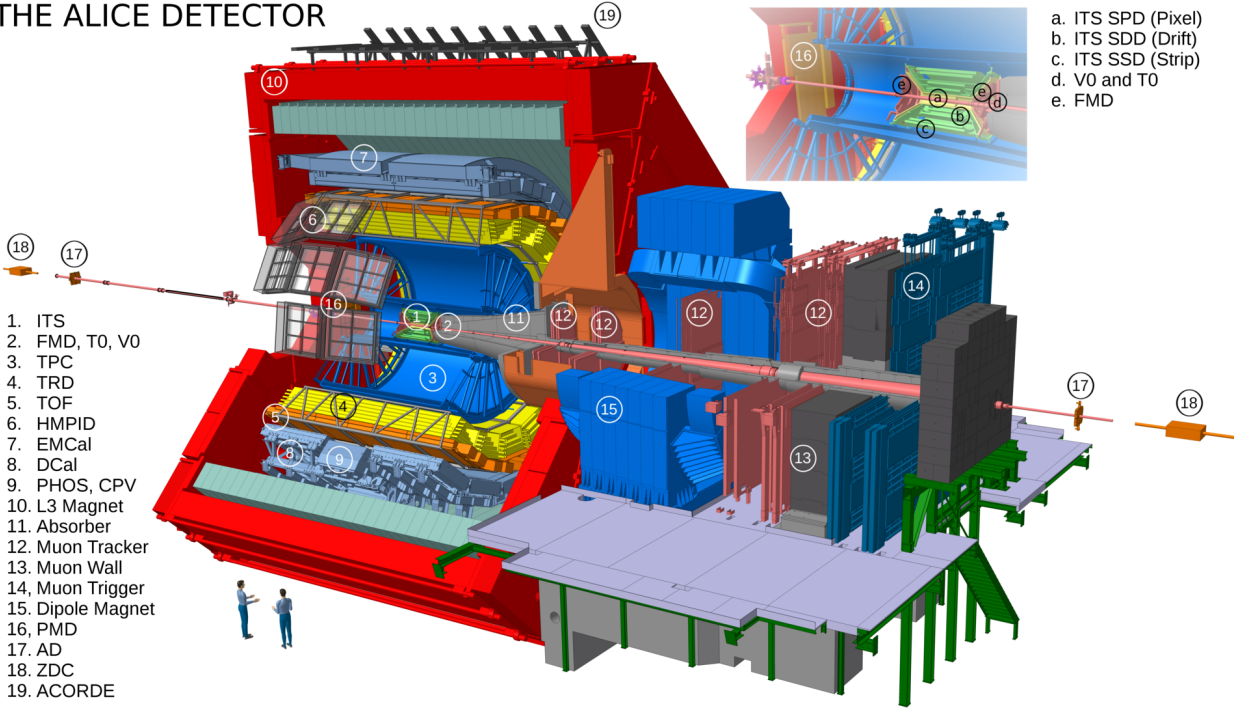
Figure 2.3: A schematic of the ALICE detector in Run 2 with the subdetector systems labeled. Taken from Ref. [70]

below 2% of the nominal value through the volume of the central barrel. The magnetic field causes charged particles to bend as they emerge from the interaction point, allowing us to measure their transverse momentum by the reconstructed trajectory of the track.

ITS

The ALICE Inner Tracking System, or ITS, is the part of the tracking system closest to the interaction point. It consists of 6 layers of silicon detectors with varying technologies and covers $|\eta| < 0.9$. Information about each of the layers, including their position, is given in Table 2.1 and they are visually shown in Figure 2.4. The ITS is used to track charged particles and to reconstruct primary and secondary vertices.

The two innermost layers comprise the Silicon Pixel Detector (SPD), with pixels of size 50 μm ($r\varphi$) × 425 μm (z). This pixel size provides a spatial precision of 12 μm in $r\varphi$ and 100 μm in z. As the innermost part of the tracker, the SPD is used to determine the position of the primary vertex by looking for where the largest number of 2-point tracklets (one from each layer) converge. It is also part of the overall ALICE triggering system.

The next two layers comprise the Silicon Drift Detector (SDD). They have an average spatial precision of 35 μm in $r\varphi$ and 25 μm in z. Silicon drift detectors were chosen for

Table 2.1: Summary of the different layers of the ALICE ITS

	SPD	SDD	SSD
Distance from beam pipe	3.9 and 7.6 cm	15.0 and 23.9 cm	38.0 and 43.0 cm
$r\varphi$ precision	12 μm	35 μm	20 μm
z precision	100 μm	25 μm	830 μm
Readout	Digital	Analog	Analog
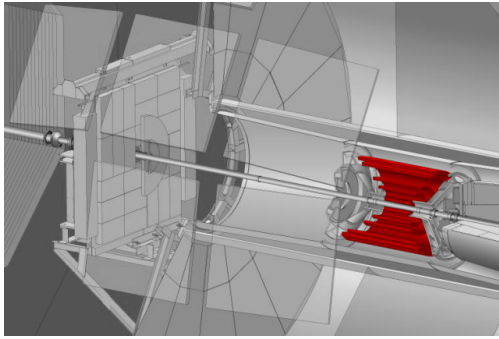
(a) The entire ITS
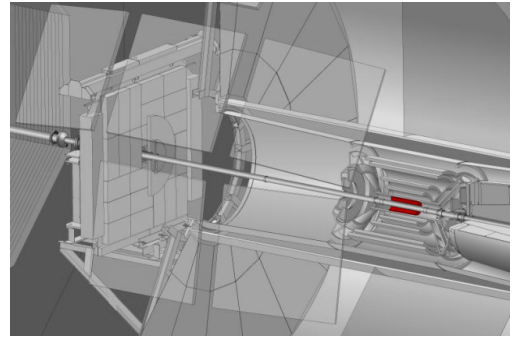
(b) The SPD layers
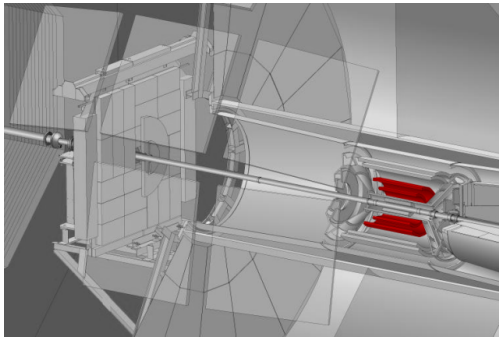
(c) The SDD layers
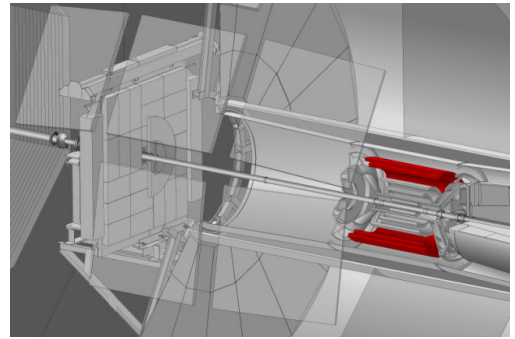
(d) The SSD layers

Figure 2.4: A schematic of the innermost part of the ALICE detector with the ITS and its subparts highlighted in red. Taken from Ref. [63]

the middle two layers because of their high resolution capabilities in high-particle-density environments and their ability to (in principle) provide energy loss information ($\mathrm{d}E / \mathrm{d}x$); $\mathrm{d}E / \mathrm{d}x$ will be discussed more in the next section. Because they use the drift time of charges, they are relatively slow compared to the other ITS layers. In order to precisely determine the drift time, the drift velocity, which changes with temperature, must be carefully monitored.

The final two layers of the ITS comprise the Silicon Strip Detector (SSD), with double-sided strip sensors with pitch 95 μm (or, equivalently, "cells" of size 95 μm ($r\varphi$) × 40 mm (z)). This gives a spatial precision of 20 μm in $r\varphi$ and 820 μm in z. The SSD layers, in principle,

also provide dE/dx information. Their radial position was chosen for track matching with the TPC.

While the ITS is nominally one system, because the three technologies are quite different from each other, in practice they operate as three separate subsystems. For the purposes of data analysis, the detector signals are simplified and treated the same way when being fed into the track reconstruction algorithm. However, during data taking, the three sub-subsystems are treated separately, each with their own detector control systems, calibration procedures, data quality management, etc. The new ITS for Run 3, with 7 layers all using the same underlying technology (pixels), will have less of this differentiation between layers.

TPC

Surrounding the ITS is the Time Projection Chamber (TPC), a cylindrical chamber filled with gas in an electric (and magnetic) field. When a particle passes through the gas, the gas is ionized, and the produced charges drift along the electric field to be collected and measured at the end plates, with the timing of the signal used to determine the position in z and the position of the signal at readout used to determine the position in r and φ.
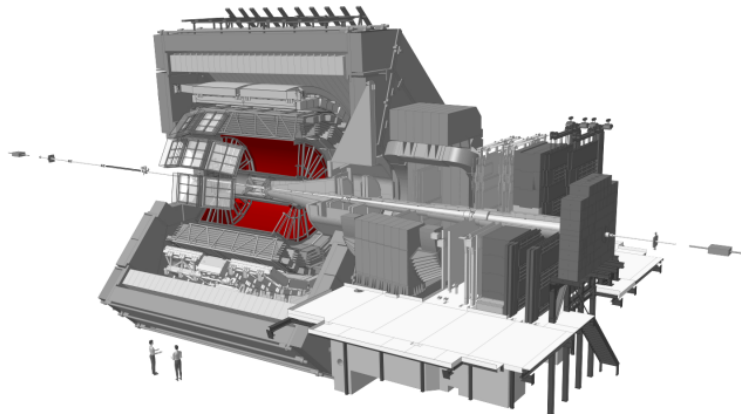
Figure 2.5: A schematic of the ALICE detector with the TPC highlighted. Taken from Ref. [63]

The ALICE TPC, shown schematically in Figure 2.5 in the context of the full detector, has an inner radius of 85 cm and an outer radius of 250 cm and is divided into 18 readout sectors (multi-wire proportional chambers) at the end plates. It is divided in half by a central high-voltage electrode, which creates an electrostatic field of about 400 V/cm along the z-axis, giving a maximum drift time of about 90 μs. A field cage surrounds the gas volume in order to maintain the uniformity of the electric field. The TPC is filled with 90 m^3 of a gas mixture of Ar-CO$_2$ (88-12) [56], which optimizes for the stability of the readout chambers.

As the TPC was designed to handle extremely high particle multiplicities (on the order of 20000 tracks at once, since it was designed for $dN/d\eta = 8000$ for $|\eta| < 0.9$) while

still meeting the physics requirements, it was optimized for some features at the cost of others. For example, a given readout sector is divided radially into two chambers (inner and outer), and the inactive areas of the two are aligned with each other; this optimizes for the momentum precision of high-momentum tracks, but causes there to be significant gaps in the acceptance such that about 10% of φ is inactive.

The multi-wire proportional chambers at the end plates are read out with cathode pads, with 159 total rows between the inner and outer chambers. This means that a single track traversing the detector can produce up to 159 hits. The pad size increases with increasing radial distance as the track density decreases, with 3 different sizes (4×7.5 mm^2, 6×10 mm^2, and 6×15 mm^2). There are a total of over 500,000 readout pads. Some schematics of the readout are given in Figure 2.6.
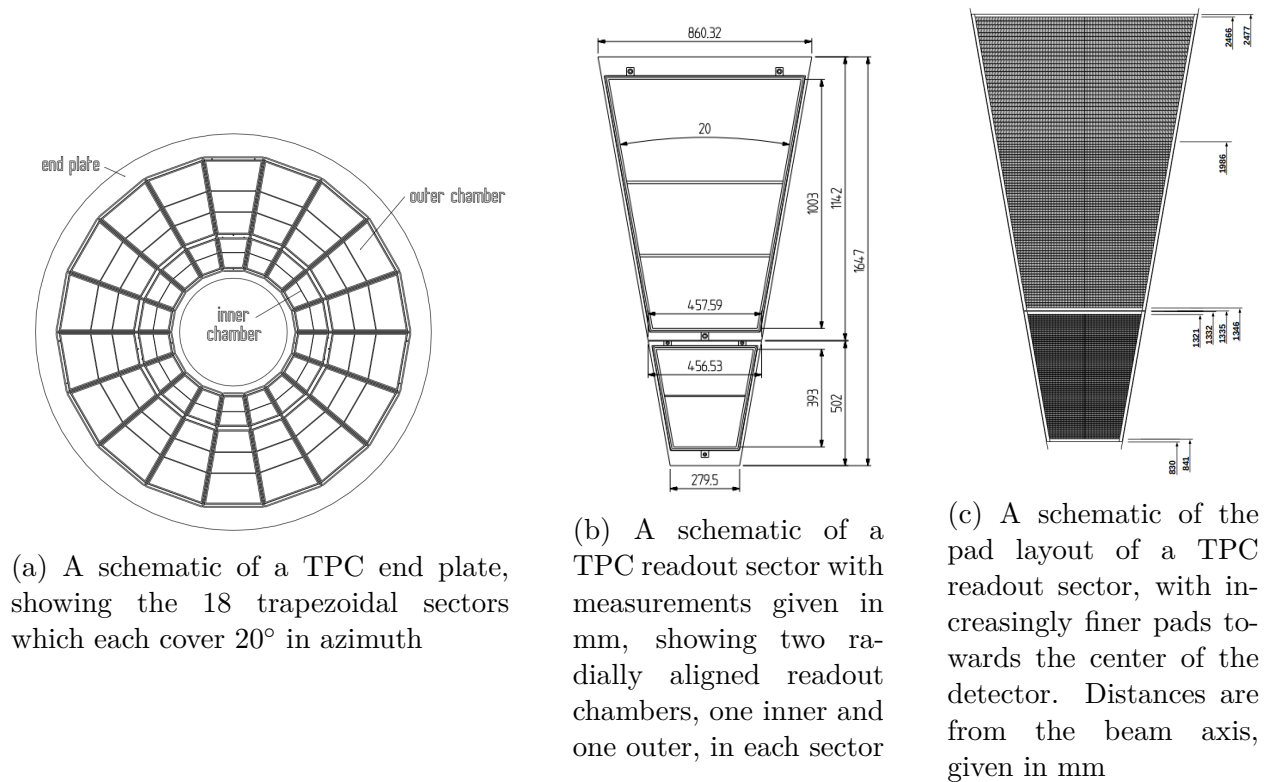
(a) A schematic of a TPC end plate, showing the 18 trapezoidal sectors which each cover 20° in azimuth

(b) A schematic of a TPC readout sector with measurements given in mm, showing two radially aligned readout chambers, one inner and one outer, in each sector

(c) A schematic of the pad layout of a TPC readout sector, with increasingly finer pads towards the center of the detector. Distances are from the beam axis, given in mm

Figure 2.6: Schematics of the TPC readout, in increasing granularity from the endplate showing the position of each sector to a breakdown of each sector into chambers and pads. All schematics taken from Ref. [46]

The TPC is designed to measure tracks with p_T from 0.1 GeV/c to 100 GeV/c. The position resolution is 800-1100 μm in $r\varphi$ and 1100-1250 μm in z. The TPC is also designed to provide dE/dx information for particle identification. dE/dx is the energy lost per distance traveled of a charged particle, which is dependent on the mass (and charge) of the

particle. By measuring $\mathrm{d}E / \mathrm{d}x$ and the particle momentum, one can identify the mass of the particle and therefore what kind of particle it is. An example of the ALICE TPC $\mathrm{d}E / \mathrm{d}x$ performance in Pb–Pb collisions at $\sqrt{s_{\mathrm{NN}}} = 2.76$ TeV can be seen in Figure 2.7. The $\mathrm{d}E / \mathrm{d}x$ resolution is about 6%.
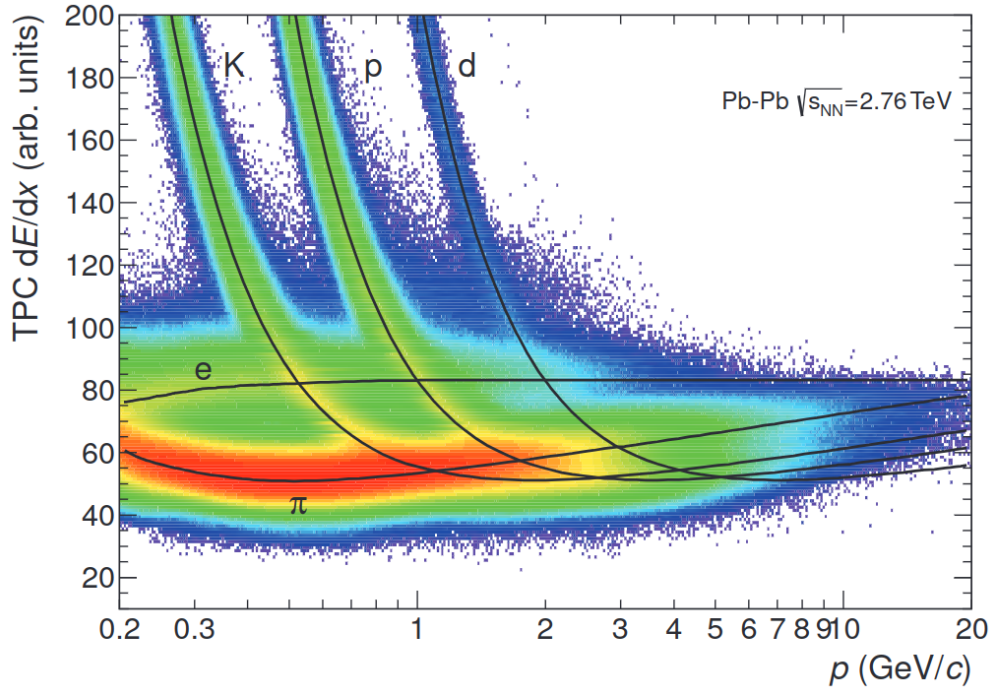
Figure 2.7: $\mathrm{d}E / \mathrm{d}x$ in the TPC with parameterizations of exepcted mean energy loss for different particles. Taken from Ref. [31]

One of the challenges with time projection chambers in general is the distortion of the electric field due to what is known as "space charge;" the ALICE TPC is no exception. When an electron is separated from an atom via ionization, the electron drifts much faster than the remaining positive ion due to its smaller mass, leading to a buildup of the heavier positive ions in the detector gas. These positive ions cause distortions in the electric field, making it nonuniform. This can cause significant problems, such as deterioration of the tracking resolution and efficiency, if it is not accounted for. Details about the space-charge distortions and how they are mitigated in the ALICE TPC can be found in Ref. [56].

EMCal and DCal

In general, electromagnetic calorimeters work by causing an incident photon or electron to create an electromagnetic shower and capturing and measuring the energy of that shower. In an electromangetic shower, a photon undergoes pair production, where it converts into

an e^+e^- pair near an atomic nucleus. Electrons and positrons undergo bremsstrahlung radiation, where they emit a photon when deflected by a charged particle like an atomic nucleus. At each step of pair production or bremsstrahlung, the outgoing particles have less energy than the incoming parent. This cascade (or shower) of pair production and bremsstrahlung continues until the particles no longer have enough energy to do so.

Calorimeters can be divided into two types, based on how the shower is created and measured: sampling and absorption (or homogeneous). A sampling calorimeter has two different kinds of materials: one to cause the particle to shower and the other to measure the energy of the shower particles. A homogenous calorimeter consists of a single material that both causes the shower and measures its energy. Absorption calorimeters tend to be more expensive but are better at ensuring that the full energy of the shower is measured.
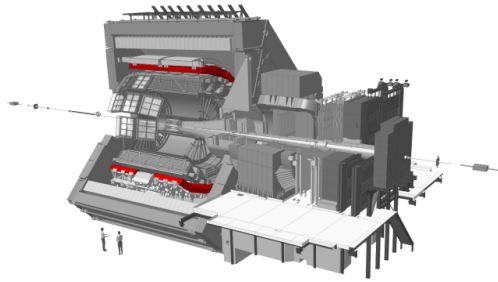
(a) A schematic of the ALICE detector with the EMCal and DCal highlighted; note the gap in the DCal where the PHOS is. Taken from Ref. [63]
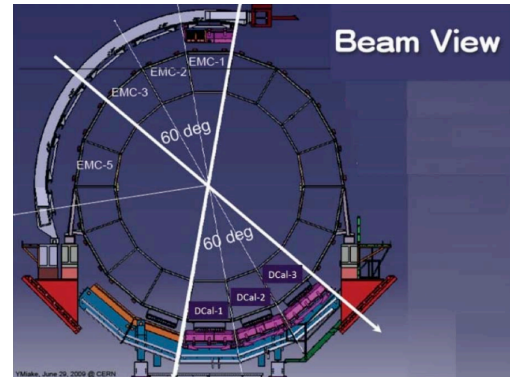
(b) An end view of the ALICE detector showing the relative positions of the EMCal and DCal. Taken from Ref. [3]

Figure 2.8: Schematics of the ALICE EMCal and DCal relative to the rest of the detector

The ALICE electromagnetic calorimeter system [30] consists of three components: the ElectroMagnetic Calorimeter (EMCal), the Dijet Calorimeter (DCal), and the Photon Spectrometer (PHOS); we use the first two for this analysis. The EMCal covers $80° < \varphi < 187°$ [2] for $|\eta| < 0.7$, while the DCal was built around the existing Photon Spectrometer (PHOS), giving it an acceptance of $0.22 < |\eta| < 0.7$ for $260° < \varphi < 320°$ and $|\eta| < 0.7$ for $320° < \varphi < 327°$. A schematic of the positions of the EMCal and DCal can be seen in Figure 2.8. From this point, "EMCAL" (all caps) will refer to both the EMCal and DCal collectively; while ALICE uses the same capitalization of the acronym when referring to both the electromagnetic calorimeter system as a whole and the part of it that is not the DCal, I will not adhere to that convention for the sake of clarity.

---

[2]Because ALICE reports φ in the range $-\pi < \varphi < \pi$, the EMCal acceptance is split across the $\pi/-\pi$ boundary such that a small fraction of it is at large negative values of φ, making φ distributions slightly awkward to look at

One of the goals of the EMCAL is the detailed exploration of jet quenching over a large kinematic range in a cost-effective way, which gives rise to a calorimeter with large acceptance and moderate resolution. In addition to measuring photons (and electrons and neutral mesons that decay into photons), it also provides a trigger for (relatively) high-p_T photons and jets, which is important for being able to make measurements involving a hard photon. It can also be used to measure the neutral component of jets, thereby making it possible to measure full jets in addition to charged-particle jets.

(a) A shashlik
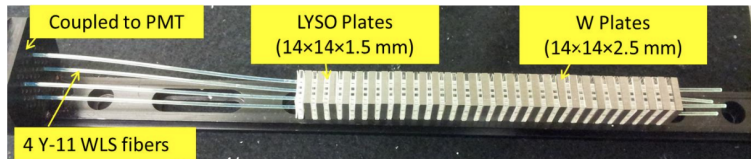
(b) A shashlik-type sampling calorimeter. Taken from Ref. [81]

Figure 2.9: Shashlik

The EMCAL is a Shashlik-type (see Figure 2.9) Pb-scintillator sampling calorimeter, which means that each cell (also called a "tower") consists of alternating layers of Pb and scintillator, with wavelength-shifting fibers running through them all. The Pb layers produce the electromagnetic shower while the scintillator layers are used to measure the energy. For the EMCAL, there are 77 layers of 1.76 mm scintillator and 76 layers of 1.44 mm Pb, which comes out to a little over 20 radiation lengths ($20.1X_0$). The radiation length X_0 of a material is the average distance it takes an electron to get down to $1/e$ of its original energy as it loses energy by traversing the material and is also related to how long it takes a photon to pair produce. With a size of $20.1X_0$, the EMCAL measures all of the energy of a photon or electron, except for the fraction of the energy deposited into the Pb (non-measuring) layers.

The EMCAL is arranged into supermodules, which come in three sizes: full-size, 2/3-size, and 1/3-size. There are 20 supermodules in all; 12 for the EMCal (10 full-size and 2 1/3-size) and 8 for the DCal (6 2/3-size and 2 1/3-size). The η-φ layout of the 20 supermodules can be seen in Figure 2.10, which was taken from Ref. [30]. A full-size supermodule has 288 modules, and a module is made of a 2×2 block of cells[3]. In total, there are 17664 cells in the EMCAL.

Each cell of the EMCAL has a size of 6 cm × 6 cm, which, at a distance of about 4.5 m from the beam line, gives a granularity of $\Delta\varphi \times \Delta\eta = 0.0143 \times 0.0143$ rad^2. The Molière radius of a material characterizes the size of an electromagnetic shower in that material; it is defined as the average radius of the cylinder needed to contain 90% of the energy of the shower. The EMCAL has a Molière radius of 3.2 cm, which means that a photon hitting the

---

[3]The cells are numbered "reasonably" within each module, as in $\frac{12}{34}$, but this results in an incomprehensible numbering system when looking at the detector as a whole, e.g. $\frac{1256}{3478}$ etc.
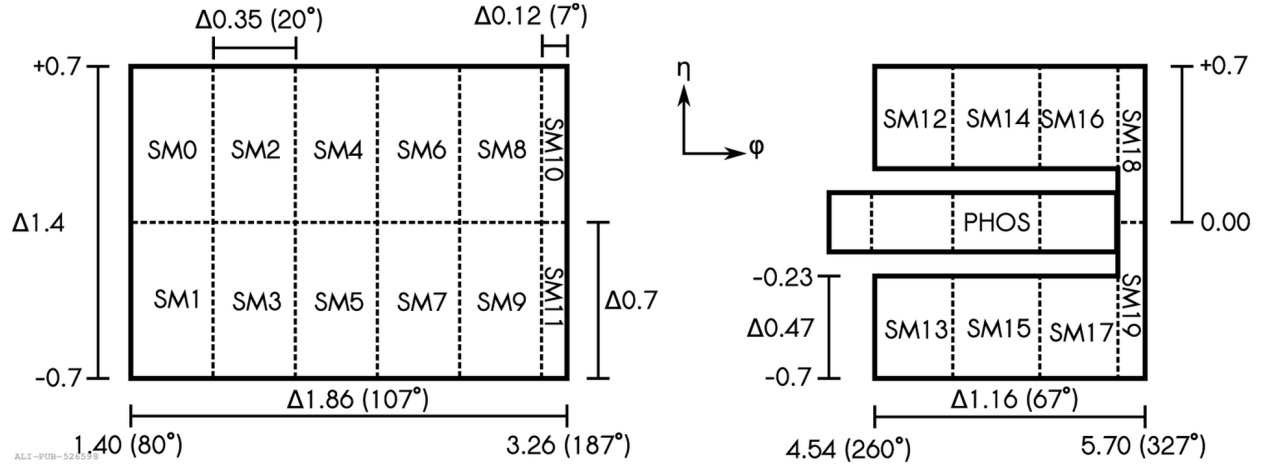
Figure 2.10: Layout of the EMCal and DCal supermodules in the η-φ plane. Taken from Ref. [30]

exact center of a cell will have most of its energy absorbed by that single cell, with relatively little leakage into neighboring cells. Generally, the energy of a photon (or electron) will be spread across several neighboring cells. This is a relatively coarse granularity, chosen in part because the EMCAL was designed to study relatively high-p_T phenomena. Another consequence of this design focus was the de-emphasis on the calorimeter resolution[4], which can be parameterized for the ALICE EMCAL as

$$\frac{\sigma_E}{E} = \frac{4.8\%}{E} \oplus \frac{11.3\%}{\sqrt{E}} \oplus 1.7\%, \tag{2.2}$$

with E given in GeV. The first term (proportional to $1/E$) comes from intrinsic detector effects that cause stochastic fluctuations, such as energy sampling, energy deposition, and light-collection efficiency. The second term (proportional to $1/\sqrt{E}$) comes from electronic noise. The third (constant) term comes from things like shower leakage and detector nonuniformity [30].

The calibration of the ALICE EMCAL is done by considering photons from π^0 decays. The π^0 has a mass peak at 135 MeV, and we use its decay channel into two photons. We identify those photons by their invariant mass, which should be near the π^0 mass. Each of these photons produces a cluster in the EMCAL, which we require to be relatively circular, and the cell at the centroid of the cluster is calibrated (across many clusters) to match the energy of the photon from the π^0 decay. This procedure is iterative, with each pass improving the extracted calibration coefficients.

---

[4]ALICE does have an electromagnetic calorimeter with much better granularity and resolution at the cost of much smaller acceptance; this is the PHOS detector

V0
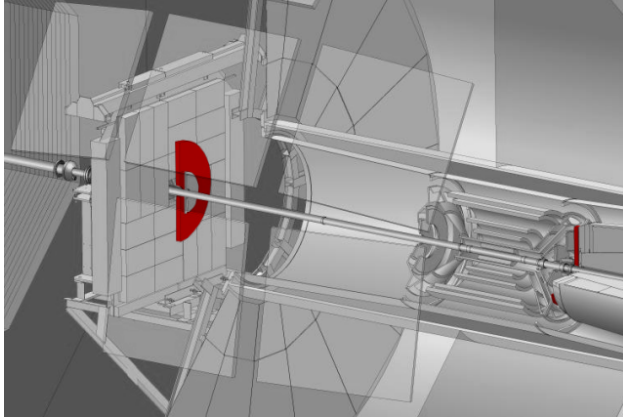
Figure 2.11: A schematic of the innermost part of the ALICE detector with the V0 system highlighted in red. Taken from Ref. [63]

The VZERO (V0) detector sits in the forward and backward regions; Figure 2.11 shows its position relative to the beampipe and ITS. This system serves a number of purposes, including triggering, separation of beam-beam interactions from background events, measurement of luminosity, and measurements of charged particle multiplicity and azimuthal distributions. For this analysis, we use the V0 system as part of the minimum-bias (MB) trigger, to determine the centrality of a given event, and to estimate the reaction plane of a given event.

The V0 system is made of two BC404 plastic scintillator arrays, one on each side of the interaction point, named V0A and V0C. V0A is 340 cm from the vertex and covers $2.8 < \eta < 5.1$; V0C is 90 cm from the vertex and covers $-3.7 < \eta < -1.7$. Each is made of 4 rings segmented into 8 parts. The light from the scintillators is wavelength shifted in order to be able to be read out via a photomultiplier system.

The V0 signals can be used in multiple ways to determine various global collision properties. The timing of the signals is used to distinguish between beam-beam and beam-gas interactions; timing information is also part of the MB trigger. The total charge collected by the scintillator arrays is used to determine the centrality of a collision, as it is proportional to the multiplicity of the event. The distribution of the total energy in both arrays is fit to a Glauber distribution [64] and divided into centrality classes, as shown in Figure 2.12. The percentage refers to the percentage of the cross section of hadronic collisions, as discussed earlier. The azimuthal distribution of charge in the system, which is segmented into 8 sectors, gives an estimate of the reaction plane.
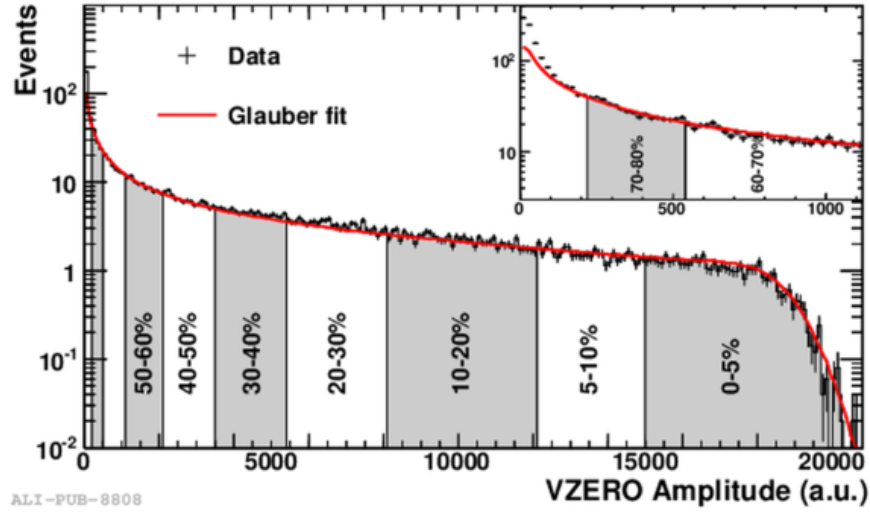
Figure 2.12: Distribution of total V0 amplitude, fit with a Glauber distribution, and divided into centrality bins, for Pb–Pb collisions at $\sqrt{s_{NN}} = 2.76$ TeV. Low-multiplicity events (to the left) are more peripheral, whereas higher-multiplicity events are more central. Taken from Ref. [26]

2.3 Triggers

Two types of triggers are used in this analysis: EMCAL gamma triggers and minimum-bias (MB) triggers. There are two EMCAL gamma triggers [73], which have thresholds at 5 and 10 GeV. They require that the energy within a 2×2 group of cells in the EMCAL be larger than those thresholds.

In addition to these "gamma-triggered" events, we also use minimum-bias (MB) events in this analysis. A MB trigger tries to select for events in which an inelastic interaction between beam particles occurred (as opposed to the bunches passing through each other without interacting or one beam interacting with the residual gas in the beampipe) with as little bias as possible. MB events are generally selected by requiring some minimum energy deposits in detectors — in ALICE, this means coincidence hits in both parts of the V0 — so real interactions that do not produce enough energy do not get selected by MB triggers.

Chapter 3

Analysis

3.1   Analysis overview

The goal of this analysis is to measure the correlation between isolated prompt photons and charged-particle jets that come from the same hard scattering. The data were collected in the 2015 and 2018 Pb–Pb collisions at $\sqrt{s_{\mathrm{NN}}} = 5.02$ TeV at the LHC, with photons measured with the EMCAL and tracks reconstructed from both the ITS and TPC. We consider photons with $28 < p_{\mathrm{T}} < 40$ GeV/c in the following centrality bins: 0-10%, 10-30%, 30-50%, 50-90%. This photon p_{T} range is optimized for the signal-to-background ratio of the per-trigger yield, given the measured jet p_{T} range described below. The tracks in the jets are required to have $p_{\mathrm{T}} > 0.15$ GeV/c and to pass the "standard" ALICE track cuts for the run periods in which the data was taken [34].

The measurement of the γ-jet correlations is complicated by backgrounds for both the prompt photons and the jets. In addition to the prompt photons we aim to measure, there are also photons from neutral meson decays (particularly neutral pions that decay into a pair of photons) and fragmentation photons (photons produced as part of a jet from quark bremsstrahlung radiation). The main background for this analysis is photons from neutral meson decays ("decay photons"). To reduce this background, we apply an isolation criterion based on the transverse momentum of the tracks surrounding the EMCAL cluster, which also reduces the fragmentation photon background [59]. Both neutral mesons and fragmentation photons are produced as part of jets, which means that they tend to be surrounded by a lot of charged particles. On the other hand, at leading order in the hard scattering, prompt photons are produced by themselves with no surrounding activity. By requiring that there be relatively little energy around the EMCAL cluster, we select against the background photons. We also use the transverse spatial energy distribution of the cluster in the calorimeter (the "shower shape") to distinguish between prompt photons and decay photon pairs, as in Ref. [27]. A cluster that passes both the isolation and shower shape criteria is called a photon candidate.

Photon candidates still contain a substantial fraction of decay photons. These come from

jets in which most of the jet energy is carried by a single neutral meson which then decays into two photons whose opening angle is sufficiently small that, due to the relatively coarse granularity of the EMCAL, the cluster looks like a single photon [29]. We determine the purity of the photon candidate sample using a template fit method, as in Ref. [27]. This fits the shower shape distribution of the clusters measured in data to a linear combination of a signal and background template. The signal template comes from an embedded γ-jet MC simulation, while the background template comes from an isolation sideband in data corrected by a combination of an embedded γ-jet MC and an embedded dijet MC. The purity is determined separately in bins of photon candidate p_T and centrality.

Charged-particle jets are reconstructed using the anti-k_T algorithm and E recombination scheme with a resolution parameter of $R = 0.2$ from the tracks in the event. The mass of the tracks is assumed to be the pion mass. The p_T of the jet as given by the anti-k_T algorithm is corrected by the underlying event density (discussed in Section 3.2) and the jet area as in Ref. [28]. For this analysis, we consider jets within $|\eta| < 0.9 - R$ with $10 < p_T < 50$ GeV/c. The $|\eta|$ requirement ensures that the entire jet lies within the acceptance of the ITS and TPC, while jets below the minimum p_T cut tend to be background-dominated.

The jets have a background as well, namely jets in the same event arising from a different hard scattering than the one that produced the photon, as well as "fake jets," which are jets reconstructed from the many soft particles comprising the underlying event that were not produced in a hard scattering. We collectively call this the combinatorial background, which is substantial in Pb–Pb collisions. However, the fake jets, which are comprised of soft particles and therefore have relatively low p_T, are reduced by the requirement of an isolated photon candidate with $p_T > 28$ GeV/c. While some photons from asymmetric π^0 decays can pass isolation cuts, they result from high momentum pions which are themselves produced in hard partonic scatterings. This biases against fake jets and allows the measurement of relatively low-p_T jets opposite a photon.

We then measure the angular correlation ($\Delta\varphi = |\varphi_\gamma - \varphi_{\mathrm{jet}}|$) and momentum imbalance ($p_T^{\mathrm{jet}}/p_T^\gamma$) of all jets paired with each photon candidate in the event. We remove the decay photon correlations by considering isolated clusters with a background-like shower shape, scaling by the purity, as was done in Ref. [27]. We remove the combinatorial background with event mixing, which pairs photon candidates with jets from minimum-bias (MB) events. The result is the correlation between prompt photons and the jets from the same hard scattering, or the per-trigger yield of jets correlated with prompt photons.

The rest of this chapter is structured as follows. First, I will discuss event reconstruction: event selection, track reconstruction, underlying event estimation, EMCAL cluster reconstruction, and simulations. Then, I will discuss the objects of interest: photon candidates and jets. Next, I will discuss how those are combined to measure photon-jet correlations and how the backgrounds are estimated and subtracted. Finally, I will describe the sources of systematic uncertainty and discuss the impact of the detector response.

3.2 Event reconstruction and selection

Track reconstruction

Tracks are reconstructed from "hits" in the ITS and TPC, which are small clusters of charge in the TPC (up to 159 for a given track) and pixel/strip hits in the ITS (up to 6 for a given track). A Kalman filter [51] is used in 3 passes in what is referred to as an "inward-outward-inward" track reconstruction scheme. First, tracks are seeded in the outermost part of the TPC. These seeds are used to reconstruct tracks in the TPC, moving inward towards the ITS. These reconstructed TPC tracks are then used as seeds for track finding in the ITS. The ITS tracks are then reconstructed moving inward again. Then, the outward propagation starts, with refitting happening this time from the ITS and then the TPC until it gets to the TRD and TOF (see Figure 2.3), where it gets matched to tracks found in those detectors. Finally, the constraints from matching to the TOF and TRD are used to do one final refit of the tracks, again from the outside moving in. All of this is done within the context of a 0.5 T magnetic field, which causes the tracks to bend according to their transverse momentum. Many more details of the track reconstruction can be found in Ref. [31]. The tracks are then required to pass the standard ALICE track cuts for Pb–Pb collisions, discussed in detail in Ref. [34].

Underlying event

The underlying event consists of the particles that were not produced in the hard scattering. In Pb–Pb collisions in particular, it causes the reconstructed energy of jets and the isolation energy of photon candidates to be too high due to the presence of the many additional particles. We use the jet area/median method [17] to calculate the underlying event density ρ. We first use FastJet [18] to cluster jets with the k_T algorithm with distance parameter $R = 0.3$. The k_T algorithm starts with the softest particles first, leading to jets reconstructed primarily from the soft particles in the underlying event. We calculate the transverse momentum density for each jet by taking its transverse momentum and dividing it by its Voronoi area as calculated with FastJet. A Voronoi diagram is the partition of a plane into regions that are closest to objects in that plane. In this case, η-φ space can be partitioned based on the positions of the tracks, and the Voronoi area is the area of the partition. We then estimate the median transverse momentum density across all jets in the event using the Harrell-Davis quantile estimator [53] (a robust method to estimate quantiles that can also give a confidence interval) with $p = \frac{1}{2}$ to get the underlying event density ρ for the event. The median is robust to outliers in the distribution and therefore reduces the impact of particles from the hard scattering.

This estimate of the underlying event density is done on an event-by-event basis. Therefore, when ρ is used to subtract the underlying event contribution to the isolation or jet p_T, there may be under- or over-subtraction due to spatial fluctuations of the underlying event, which are not taken into account in this method. This under- and over-subtraction

contributes to the jet energy resolution, which will be discussed in a later section. Table 3.1 shows the mean values and standard deviations of ρ for various centrality ranges and Figure 3.1 shows the ρ distributions themselves.

Table 3.1: Mean values and standard deviations of ρ in various centrality ranges, first for 10%-wide ranges and then for centrality ranges relevant for this analysis

Centrality	$\langle\rho\rangle$ [GeV/area]	Std dev
0-10%	151.144	19.578
10-20%	101.691	13.152
20-30%	68.072	9.752
30-40%	43.878	7.221
40-50%	26.628	5.248
50-60%	14.966	3.577
60-70%	7.768	2.245
70-80%	3.811	1.343
80-90%	2.009	0.885
0-30%	117.515	37.258
30-50%	37.363	10.620
50-90%	11.235	5.449
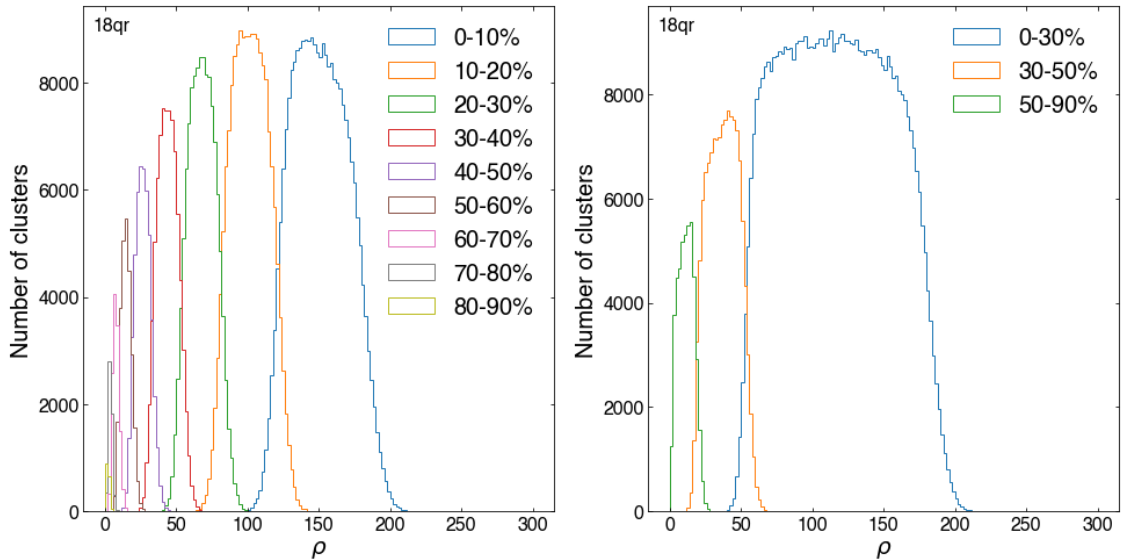
Figure 3.1: Distribution of underlying event density estimate for various centrality ranges

EMCAL cluster reconstruction and selection

In each event, neighboring cells in the EMCAL are grouped together using the V2 clusterizer algorithm, which groups the cells into clusters that have at most one local (and therefore global) maximum. There are two energy thresholds associated with this algorithm, the "seed" energy, which is a lower limit on the energy of the cell with the maximum energy in the cluster, and the "cell" energy, below which a cell is essentially ignored in the clustering. For this analysis, we use 500 MeV for the "seed" energy and 100 MeV for the "cell" energy.

Before the cells are clustered, a number of corrections are applied through the ALICE EMCal correction framework. These include:

- CellEnergy (energy calibration of each cell)

- CellBadChannel (masking of noisy cells and cells with an "improper" response)

- CellTimeCalib (correction for cable length, electronics response time, clock phase differences)

- CellTrackMatcherAndMIPSubtraction (subtracting the minimum-ionizing particle (MIP) energy for tracks whose trajectories match an EMCAL cell)

- CellEmulateCrosstalk (in MC only — emulation of the cross-talk between channels on the electronics cards)

After the clusters are formed, more corrections are applied through the ALICE EMCal correction framework. These include:

- ClusterNonLinearity (cluster energy non-linearity correction derived from electron beam data, which is negligible above 3 GeV)

- ClusterNonLinearityMCAfterburner (in MC only — additional corrections to the non-linearity correction)

Then, the following cuts are applied on each EMCAL energy cluster:

- $28 < p_\mathrm{T} < 40$ GeV/c (the range of interest for this analysis)

- $|\eta| < 0.67$ (avoid the edges of the detector)

- $E_\mathrm{cross}/E_\mathrm{max} > 0.05$ (remove "pointy"/"exotic" clusters) — E_cross is the sum of the energies of the 4 orthogonally adjacent cells to the cell with the maximum energy in the cluster, whose energy is E_max

- # cells ≥ 2 (remove single-cell clusters, which is redundant after the above cut but made explicit here regardless)

- distance to bad channel ≥ 1 (avoid bad channels)

- $\sigma_{\text{long}}^2 < 0.1$ (remove contamination from neutrons hitting the readout electronics) — σ_{long}^2 will be defined in Section 3.4

- |time| < 20 ns (reduce pileup, which is when multiple collisions are read out in the same event)

  - This cut is made in the data but not the MC because of a known issue with calculating the cluster time in MC productions. There is no pileup in the MC, so it should have minimal effect.

The effect of each of these cuts, in each of the data, embedded γ-jet MC, and embedded dijet MC is summarized in Table 3.2. In the data, the cuts with the largest effect are the "exoticity" cut on $E_{\text{cross}}/E_{\text{max}}$ and the pileup cut on |time|. In the simulations, the cut with the largest effect is again the exoticity cut; there is no pileup cut made in the MC.

Table 3.2: Number of clusters remaining after each cut in the cluster cutflow with the survival percentage from the previous cut in parentheses

Cut	Data	γ-jet MC	Dijet MC
$28 < p_{\text{T}} < 40$ GeV/c	78616	1067038	391791
$|\eta| < 0.67$	78605 (99.9%)	1066617 (99.96%)	391709 (99.98%)
$E_{\text{cross}}/E_{\text{max}} > 0.05$	76152 (96.9%)	1050573 (98.5%)	367836 (93.9%)
# cells ≥ 2	76152 (100%)	1050573 (100%)	367836 (100%)
Distance to bad channel ≥ 1	76152 (100%)	1038382 (98.8%)	363878 (98.9%)
$\sigma_{\text{long}}^2 > 0.1$	76143 (99.99%)	1038115 (99.97%)	363875 (99.999%)
|time| < 20 ns (data only)	73644 (96.7%)	-	-

(a) Clusters from 2018 data

Cut	Data	γ-jet MC	Dijet MC
$28 < p_{\text{T}} < 40$ GeV/c	28290	247781	248376
$|\eta| < 0.67$	28284 (99.98%)	247651 (99.9%)	248314 (99.98%)
$E_{\text{cross}}/E_{\text{max}} > 0.05$	27385 (96.8%)	242552 (97.9%)	230203 (92.7%)
# cells ≥ 2	27385 (100%)	242552 (100%)	230203 (100%)
Distance to bad channel ≥ 1	27385 (100%)	239262 (98.6%)	227672 (98.9%)
$\sigma_{\text{long}}^2 > 0.1$	27385 (100%)	239214 (99.98%)	227668 (99.998%)
|time| < 20 ns (data only)	26865 (98.1%)	-	-

(b) Clusters from 2015 data

Event selection

The following criteria are used to select events for the photon-jet correlations:

- The run is in the "good" run list, which is determined by the Data Preparation Group within the ALICE collaboration and is based on the Quality Assurance status of the tracking detectors in the Central Barrel and the EMCAL [1]

- The event contains at least one EMCAL cluster with $p_{\mathrm{T}} > 15$ GeV/c

- The primary vertex is within 10 cm of the nominal interaction point in the longitudinal direction, i.e. $|z$-vertex$| < 10$ cm

- The event is selected by one of the EMCAL gamma triggers (the kEMCEGA event selection, in ALICE terms)

For the MB data used for embedding and event mixing in this analysis, instead of the kEMCEGA event selection, the event must instead pass one of kINT7 (MB), kCentral (MB with roughly 0-10% centrality), and/or kSemiCentral (MB with roughly 30-50% centrality) event selections, depending on the centrality of the event. In particular, for 0-10% centrality, the event is allowed to pass either kINT7 or kCentral; for 30-50% centrality, the event is allowed to pass either kINT7 or kSemiCentral; and for all other centralities, the event must pass kINT7. See Ref. [74] for more information about these event selections.

3.3 MC simulations

While there are models and event generators that simulate full Pb–Pb events, none of them are currently able to reproduce both the hard and soft components of Pb–Pb events simultaneously. Therefore, instead of using one of these models, we embed simulated pp events into Pb–Pb from data, which effectively simulates a hard scattering with the soft Pb–Pb background. This data-driven method is a more accurate approach to modeling the effects of the underlying event.

To generate the simulated pp events, we use PYTHIA 8 [67], which is a widely-used general-purpose MC event generator in high-energy physics. It is highly configurable in many aspects; we use the Monash 2013 tune [68] with the NNPDF2.3 LO PDF set [23], which configures PYTHIA to match a large set of measurements from data from experiments at LEP, SLAC, the SPS, the Tevatron, and the LHC. This tuning for pp collisions in PYTHIA is why we use pp, rather than a more general nucleon-nucleon collision, even though a ^{208}Pb nucleus actually has more neutrons (126) than protons (82). The "truth" particles produced by PYTHIA are then transported through a simulation of the detector using GEANT 3 [14] to produce "reconstructed-level" particles. ALICE centralizes the production of these MC simulations.

For this analysis, we use two types of simulations: events that produce a high-p_{T} photon and jet (gamma-jet, or GJMC, which in PYTHIA is the `PromptPhoton:all` flag) and events that produce two high-p_{T} jets with at least 7 GeV in the electromagnetic calorimeters (dijet, or JJMC, which in PYTHIA is the `HardQCD:all` flag). These productions are then anchored to 15o and 18q + 18r, which are the runs in which the Pb–Pb data was taken; this means

that the detector simulation matches the detector performance seen in those runs and that the center-of-mass energy is matched, namely $\sqrt{s} = 5.02$ TeV. One more nuance about using PYTHIA in ALICE is that, in order to optimize the statistical power of the simulation, samples are generated in different bins of "pthat" (also called "pT-hard"), which refers to the p_T of the scattered photon or parton in the $2 \rightarrow 2$ hard scattering in the generated event. This means that when combining events from different pthat bins, we have to do so with weights based on the cross-section of the simulated process.

In order to embed a pp event simulated by PYTHIA, we combine it with a MB Pb–Pb event from data. For the tracks, we simply combine the tracks from the simulation and data[1], as the detector occupancies are fairly low, even in central Pb–Pb. This is not the case in the EMCAL. Consequently, for the EMCAL, we combine the cell energies from the simulation and data before rerunning the clusterizer. The centrality of the event is determined by the centrality of the MB event. All of this is done with the ALICE embedding framework [2].

For this analysis, the embedded MC is used in two ways. It is used in determining the purity of the photon candidate sample, as part of the template fit procedure, which only uses EMCAL clusters. It is also used to determine the detector response for folding the theoretical calculations.

3.4 Isolated photon identification

Photon isolation

The isolation "energy"[2] p_T^{iso} is defined as the sum of the p_T of the tracks within a cone of some radius R ($R^2 = (\Delta\eta)^2 + (\Delta\varphi)^2$), after subtraction of the underlying event density ρ scaled by the area of the cone:

$$p_T^{\text{iso}} = \Sigma_{\text{tracks}}\ p_T^{\text{track}} - \rho \cdot \pi R^2. \tag{3.1}$$

At leading order, prompt photons are surrounded by little to no hadronic activity. We would therefore expect the isolation energy of prompt photons to be close to zero. On the other hand, fragmentation and decay photons tend to be produced within jets and therefore are relatively likely to have a large amount of energy in the isolation region (large p_T^{iso}). Therefore, requiring p_T^{iso} to be small, which we refer to as making an "isolation cut," tends to select against the background photons and enhance the fraction of signal photons. Additionally, we sometimes require p_T^{iso} to be large, which we refer to as making an "anti-isolation cut," for the purposes of selecting a sample of (mostly) background photons.

In heavy ion collisions, we sometimes use a relatively small value of jet R, $R = 0.2$ (e.g. in Ref. [28]), in order to reduce the effects of the fluctuations in the underlying event and in the fragmentation of partons. In this analysis, we choose the same R for the photon isolation. From this point, p_T^{iso} always refers to $R = 0.2$ unless otherwise stated.

---

[1]The more "correct" way to do this is to go back to the hits in the ITS and TPC and refit the tracks

[2]"Isolation transverse momentum" is too hard to say, and besides, they're the same in natural units
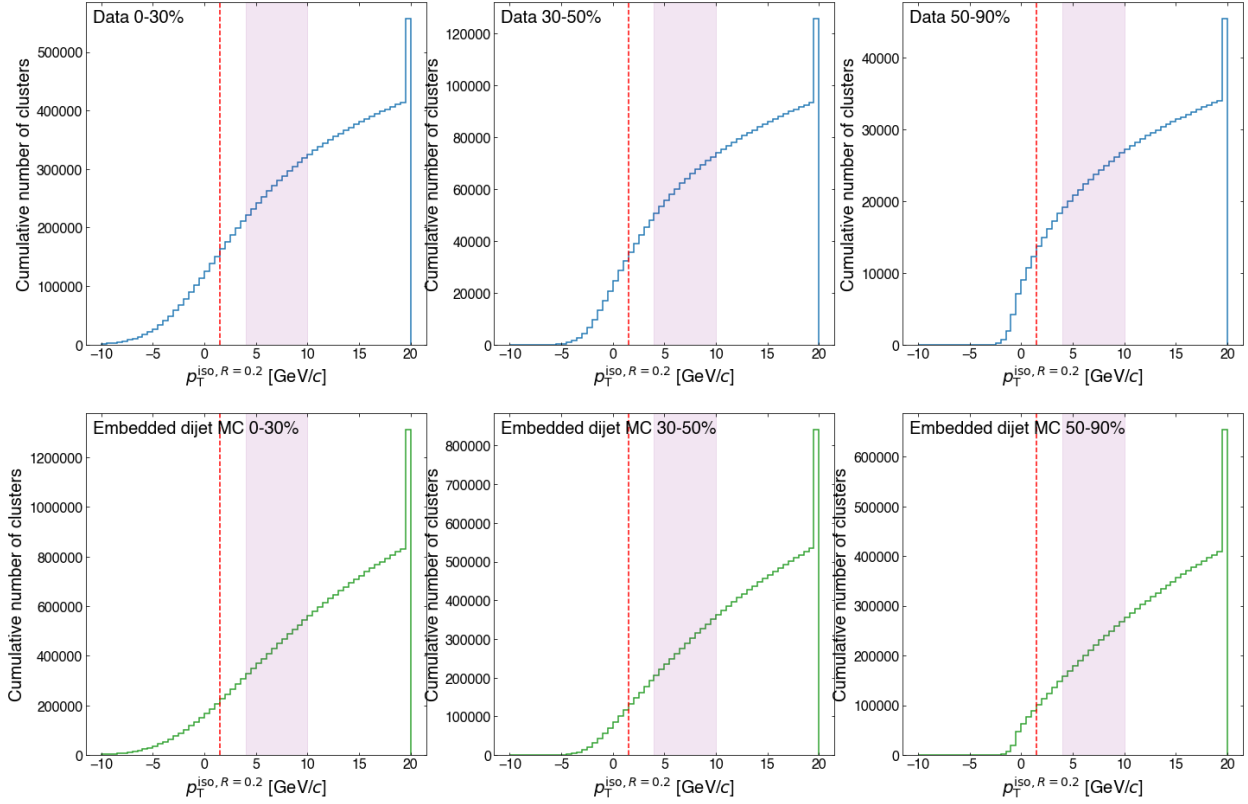
Figure 3.2: Cumulative (non-normalized) distribution of $p_\mathrm{T}^\mathrm{iso}$ (R=0.2) split by centrality in data (top) and embedded dijet MC (bottom). The red dashed line shows the isolation cut at 1.5 GeV/c and the shaded area indicates the anti-isolation range of 4–10 GeV/c.

Figure 3.2 shows the non-normalized cumulative $p_\mathrm{T}^\mathrm{iso}$ distributions of clusters in embedded dijet MC and real Pb–Pb data. From this, we can look at any range of $p_\mathrm{T}^\mathrm{iso}$ and determine how many photon candidates are present in that range. We use these to help decide where to make the isolation and anti-isolation cuts. For the isolation cut, we want the fraction of signal photons to be large and the fraction of background photons to be small. For the anti-isolation range, we want the fraction of signal photons to be small while maximizing the statistics of the embedded dijet MC and data; furthermore, we want that range to be as close as possible to the isolation cut due to the correlation between the isolation and shower shape of a cluster.

Figure 3.3 shows the normalized cumulative $p_\mathrm{T}^\mathrm{iso}$ distributions of clusters in embedded γ-jet MC (signal) and embedded dijet MC (background). At each value of $p_\mathrm{T}^\mathrm{iso}$, we can read off an estimate of the fraction of signal and background clusters that pass that selection as estimated by these embedded MC samples. For example, the isolation selection for this analysis is represented by the vertical dashed red line. The intersection of this line with the
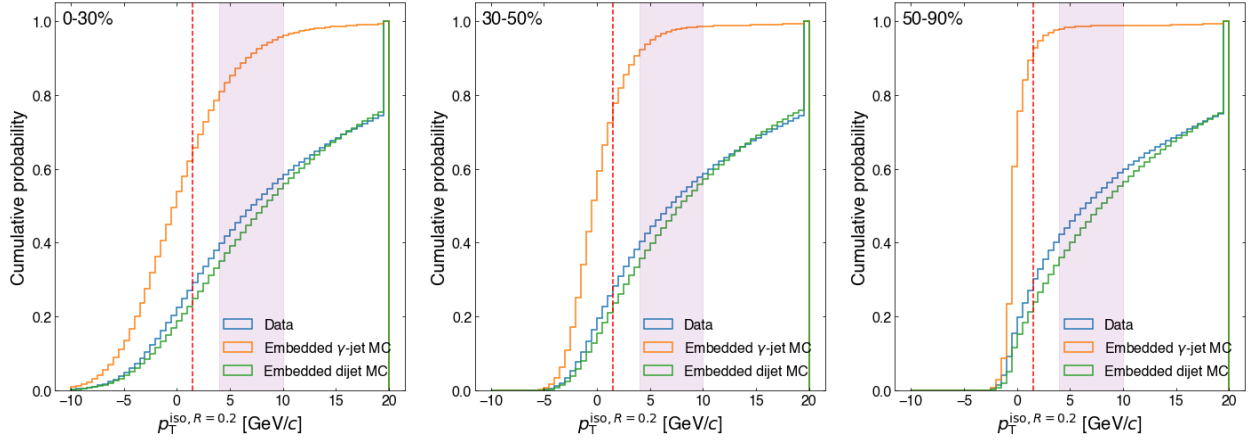
Figure 3.3: Normalized, cumulative distribution of p_T^{iso} (R=0.2) split by centrality. The red dashed line shows the isolation cut at 1.5 GeV/c and the shaded area indicates the anti-isolation range of 4–10 GeV/c.

orange and green curves gives the percentage of clusters that pass the isolation selection in the signal and background, respectively.

In this analysis, the isolation cut is chosen to be $p_T^{iso} < 1.5$ GeV/c. The upper rows of Table 3.3 give the percentage of signal and background clusters that pass this isolation selection. The anti-isolation range is chosen to be $4 < p_T^{iso} < 10$ GeV/c, and the lower rows of Table 3.3 give the percentage of signal included in the anti-isolation range and the number of clusters in the data and dijet MC. The signal contamination in the anti-isolation region is accounted for when calculating the purity of the photon candidates.

Table 3.3: Percentages and numbers of photon candidates in each isolation selection, split by centrality

Centrality	0-30%	30-50%	50-90%
Isolation cut $p_T^{iso} < 1.5$ GeV/c			
% of signal MC	61.5%	71.7%	88.5%
% of background MC	15.7%	13.8%	13.6%
# of clusters in data	149857	32145	12282
Anti-isolation range 4–10 GeV/c			
% of signal MC	16.9%	7.9%	1.3%
# of clusters in data	107831	24371	8486
# of clusters in background MC	237060	158628	120187

Shower shape

The distribution of the energy in a cluster, or the "shape" of the shower, can help us distinguish between prompt photons and non-prompt photons (e.g. decay photons), some examples of which are shown in Figure 3.4. A cluster with one photon tends to have a symmetric shower if it hits near the center of an EMCAL cell, whereas a cluster with two photons can have a more elongated shower if those photons are slightly separated spatially but still close enough to end up in the same cluster.
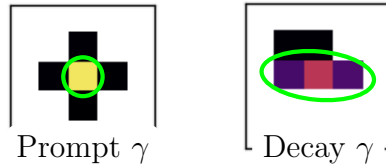
Figure 3.4: Example of a cluster containing a prompt photon (left) and a cluster containing a pair of decay photons (right), with an approximation of a fitted ellipse in green; brighter colors correspond to a larger percentage of the cluster energy in that cell

Traditionally in ALICE, the shower shape is quantified with the σ^2_{long} variable, which takes the indices of the cells in the cluster to calculate the square of the larger eigenvalue of the energy distribution in the η-φ plane. It can be thought of as the long axis of the ellipse fit to the energy-weighted positions of the cells in the cluster, as sketched in the green curves in Figure 3.4. More precisely, it is defined according to Ref. [27] as

$$\sigma^2_{\text{long}} = \frac{\sigma^2_{\varphi\varphi} + \sigma^2_{\eta\eta}}{2} + \sqrt{\frac{\sigma^2_{\varphi\varphi} - \sigma^2_{\eta\eta}}{4} + \sigma^2_{\varphi\eta}}, \tag{3.2}$$

where $\sigma^2_{\varphi\eta} = \langle \varphi\eta \rangle - \langle \varphi \rangle \langle \eta \rangle$ are the covariance matrix elements; the integers φ and η are the cell indices in their respective directions; and $\langle \varphi\eta \rangle$ is the second moment and $\langle \varphi \rangle$, $\langle \eta \rangle$ are the first moments of the position of the cells within the cluster. Furthermore, the position is log-weighted by the energy with some cutoff w_0:

$$\text{weight} = \max(\log(E_{\text{cell}}/E_{\text{cluster}}), w_0), \tag{3.3}$$

where, as in Ref. [27], we choose the cutoff to be $w_0 = -4.5$. This means that cells that contain less than 1.1% of the total cluster energy are not considered in σ^2_{long} calculation; if only one cell passes this cutoff, the value is exactly 0.25.

For this analysis, we use a modified version of σ^2_{long} which we call $\sigma^2_{\text{long(5x5)}}$. For this variable, rather than using all of the cells in the cluster in Equation 3.2, we instead use all of the cells in the 5×5 grid centered at the cell with the most energy in the cluster. This means both that sometimes cells that are part of the cluster are excluded from the shower shape calculation and also that sometimes cells that are not part of the cluster are included

in the shower shape calculation. Calling it the "cluster shower shape" is therefore a bit of a misnomer, but it does characterize the shape of the EMCAL shower in the vicinity of the cluster.
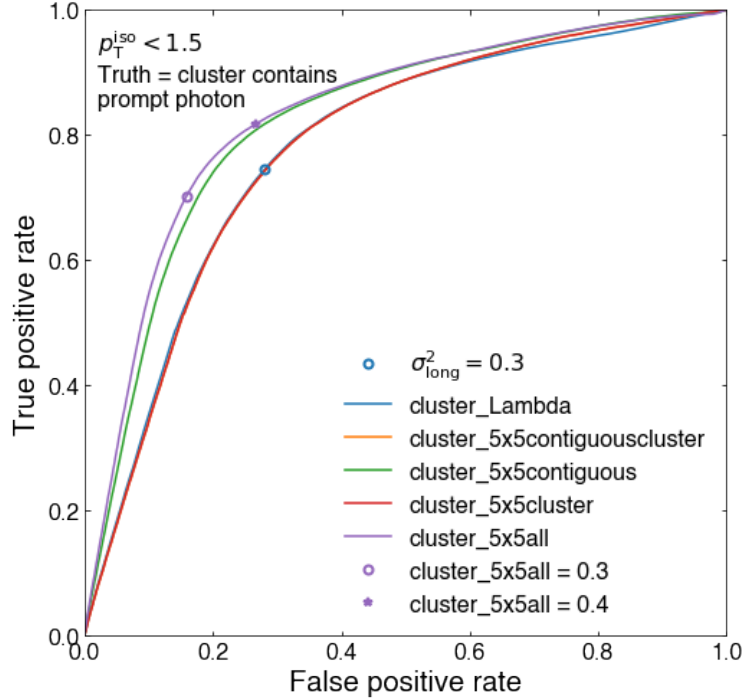
Figure 3.5: ROC curve for various 5×5 shower shape variations as compared to σ_{long}^2. The TPR and FPR for particular thresholds of certain variables are indicated as open points. cluster_5x5all is the same as $\sigma_{\text{long(5x5)}}^2$

The receiver operating characteristic (ROC) curve in Figure 3.5 demonstrates that the $\sigma_{\text{long(5x5)}}^2$ shower shape variable (labeled cluster_5x5all) does a better job of distinguishing between prompt photons and non-prompt photons (e.g. decay photons) than the traditional σ_{long}^2 shower shape variable or other 5×5 variations of σ_{long}^2 variable. A ROC curve plots the true positive rate (TPR) against the false positive rate (FPR) for a binary discriminator as its threshold is varied. The true positive rate is the percentage of real positive cases that are (correctly) identified as positive, while the false positive rate is the percentage of real negative cases that are (incorrectly) identified as positive. A perfect binary discriminator has TPR=1 and FPR=0 while a completely random classifier will have a linear response between $(0, 0)$ and $(1, 1)$; we want a discriminator with a high TPR and a low FPR [50]. We see that $\sigma_{\text{long(5x5)}}^2$ is a better discriminator of clusters with prompt photons than the other variations, including the standard σ_{long}^2.

The shape of the $\sigma_{\text{long(5x5)}}^2$ distributions is relatively similar to the σ_{long}^2 distributions, as single photons produce a sharp peak at approximately 0.25 in both variables and there

is a secondary bump at larger values. Figure 3.6 shows the $\sigma^2_{\text{long(5x5)}}$ distributions in the embedded γ-jet and dijet MCs compared to the σ^2_{long} distributions. From this, we see that the distributions of the $\sigma^2_{\text{long(5x5)}}$ variable are different between prompt and non-prompt photons, as the dijet MC is dominated by non-prompt photons. We also see that the notable effects of switching to $\sigma^2_{\text{long(5x5)}}$ from σ^2_{long} are the reduction of the size of the peak at 0.25 and the improved separation of the secondary peak above 0.5 (which is absent in the γ-jet MC).
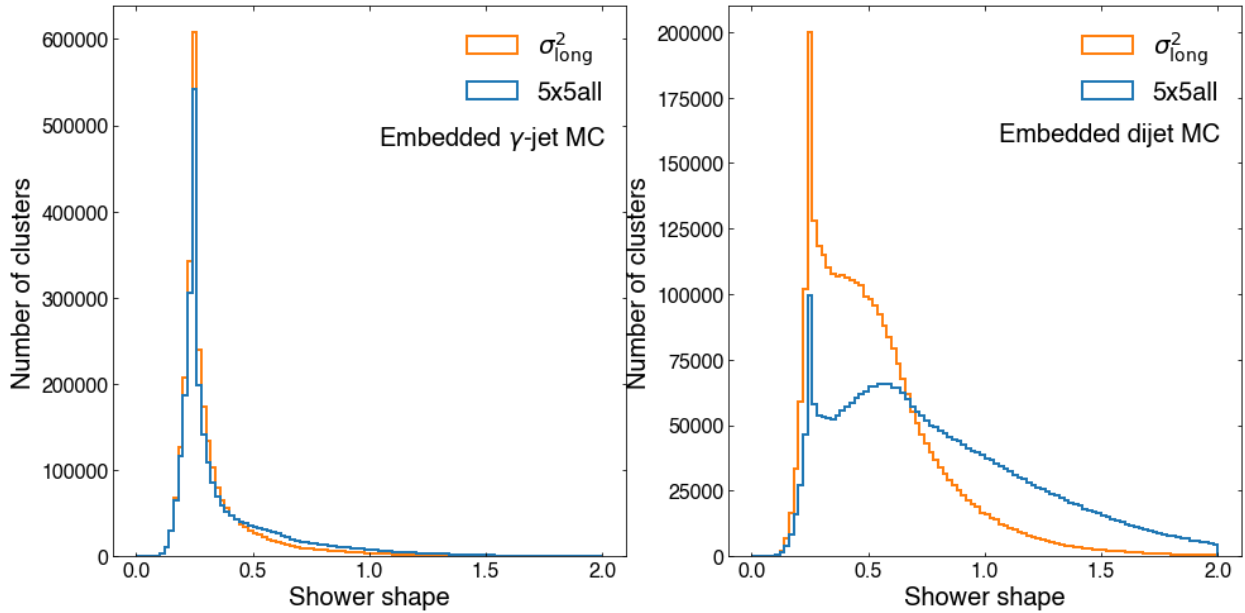
Figure 3.6: Distribution of $\sigma^2_{\text{long(5x5)}}$ and σ^2_{long} for embedded γ-jet MC (left) and embedded dijet MC (right)

We use the shower shape to define two populations of clusters. "Signal-like" clusters have small values of $\sigma^2_{\text{long(5x5)}}$ ($0.1 < \sigma^2_{\text{long(5x5)}} < 0.3$) while "background-like" clusters have larger values of $\sigma^2_{\text{long(5x5)}}$. These will be referred to as the signal region (SR) and background region (BR) throughout the rest of this thesis. The definition of background-like clusters is centrality-dependent and is summarized in Table 3.4; how these thresholds are determined will be discussed in a later section. Photon candidates are defined to be clusters that are signal-like and isolated ($p_{\text{T}}^{\text{iso}} < 1.5$ GeV/c). Table 3.5 shows the number of photon candidates in each centrality bin. There is still a significant fraction of non-prompt photons in this photon candidate sample, so we need to estimate the purity, which we do via the template fit method.

Table 3.4: $\sigma^2_{\text{long(5x5)}}$ thresholds for background-like clusters

Centrality	Lower bound	Upper bound
0-30%	1.0	2.0
30-50%	0.6	2.0
50-90%	0.4	2.0

Table 3.5: Number of photon candidates in each centrality bin

Centrality	Number of photon candidates
0-10%	13806
10-30%	20359
30-50%	10318
50-90%	4240

Template fits and photon purity

We leverage the observation that the shower shape distributions of the signal and background clusters are different (as seen in Figure 3.6) in order to determine the purity of isolated signal-like clusters. In principle, we can use any variable, not just a shower shape variable, as long as that variable has substantially different distributions for the signal and background clusters. The shower shape is a good choice because, in addition to having different distributions, the main causes of the difference are relatively well-understood from a physical perspective.

We fit the shower shape distribution of the isolated clusters in the data to a linear combination of signal and background templates. The isolated clusters in the data consist of isolated prompt photons (the signal) and isolated non-prompt photons (the background). The signal template comes purely from the embedded γ-jet MC. The background template is more complicated. Ideally, it should be as data-driven as possible, so we start with the anti-isolated clusters in the data. However, as Figure 3.7 shows, the shower shape distribution is somewhat different for the isolated non-prompt photons vs the anti-isolated non-prompt photons. Since the "true" background in the data is *isolated* non-prompt photons, we need to correct the anti-isolated non-prompt photon distribution to get the true background.

The background template correction comes from a combination of the embedded γ-jet and dijet MCs; the inclusion of the γ-jet MC helps account for signal leakage in the anti-isolation region. In addition to being weighted by their respective production cross-sections, we also use R_{AA} to further scale the dijet MC. R_{AA}, the nuclear modification factor, quantifies how the yield of some object in a nucleus-nucleus (AA) collision differs from an equivalent pp collision. As described in Section 3.3, the embedding is done using a pp MC production, which means that there is no jet quenching effect from the QGP. In order to account for the fact that, in Pb–Pb collisions, the production rate of high-p_{T} partons per nucleon-nucleon
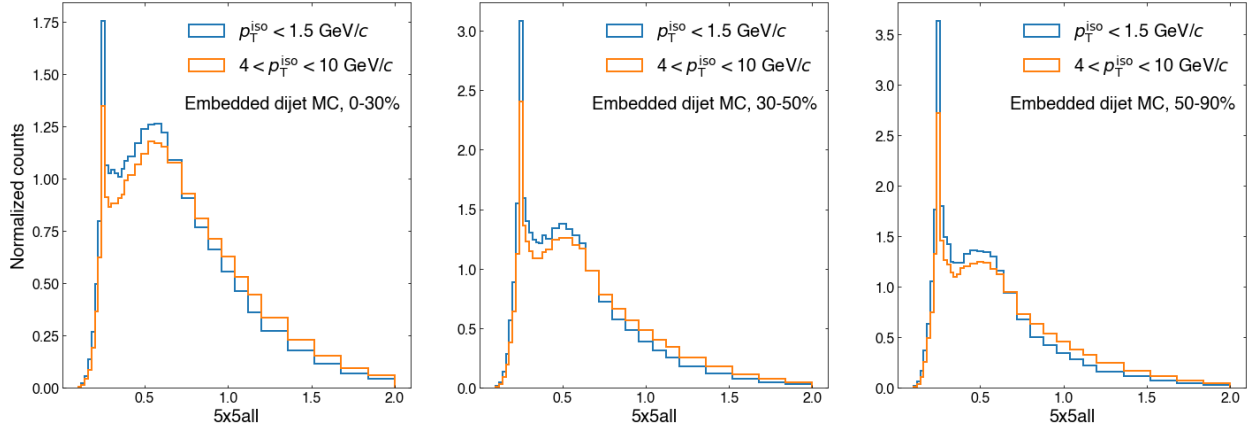
Figure 3.7: $\sigma^2_{\text{long(5x5)}}$ distributions in embedded dijet MC with the isolation (blue) and anti-isolation (orange) cuts

collision is significantly lower than in pp collisions, we need to scale the embedded dijet MC by R_{AA}. We do this by looking at the parent of the photon in the cluster. Most of the time, this is a π^0. ALICE does not yet have published measurements of R_{AA} for π^0s, but there are measurements of charged hadron R_{AA} in $\sqrt{s_{\text{NN}}} = 5.02$ TeV Pb–Pb collisions [33]. Other measurements of R_{AA} show that it is about the same for charged and neutral pions [44], and charged hadrons are mostly charged pions, so we use the charged hadron R_{AA} to approximate the π^0 R_{AA}. We use the p_{T} of the parent π^0 and the centrality of the Pb–Pb event that was embedded into to determine the R_{AA} for that cluster. Since R_{AA} of direct photons has been shown to be 1, there is no such scaling for the embedded γ-jet MC.

The background template is corrected with the combined MCs as follows. We take the ratio of the shower shape distributions for the isolated background to the anti-isolated background, as modeled by the MCs. We can write this ratio bin-by-bin in the shower shape as:

$$\text{Weights}(\sigma^2_{\text{long(5x5)}}) = \frac{R_{\text{AA}} \cdot \text{Dijet}_{\text{Iso}}}{R_{\text{AA}} \cdot \text{Dijet}_{\text{Anti-iso}} + \gamma\text{-jet}_{\text{Iso}}}, \tag{3.4}$$

where the R_{AA} refers to the additional cluster-by-cluster weighting; it is not an overall multiplicative factor. The background template is then

$$\begin{aligned} \text{Bkg template} &= \text{Data}_{\text{Anti-iso}} \times \text{Weights} \\ &= \text{Data}_{\text{Anti-iso}} \times \frac{R_{\text{AA}} \cdot \text{Dijet}_{\text{Iso}}}{R_{\text{AA}} \cdot \text{Dijet}_{\text{Anti-iso}} + \gamma\text{-jet}_{\text{Iso}}}. \end{aligned} \tag{3.5}$$

If the combination of the anti-isolated MCs exactly represents the anti-isolated data, and the isolated dijet MC exactly represents the isolated background, then this correction

with Weights will exactly modify the anti-isolated data to the true isolated non-prompt background. The MC is not a perfect representation of the data, but as long as the relative difference between the anti-isolated and isolated non-prompt photons is reasonably well-modeled by the MCs, this correction is still valid, albeit with an associated systematic uncertainty. Figure 3.8 shows that, as the anti-isolation range gets further from the isolation cut, the shower shape distribution of the anti-isolated clusters becomes increasingly different from that of the isolated clusters; this is particularly visible in the region of the first peak. Consequently, it is important to choose an anti-isolation range that is as close to the isolation region as feasible, in order to reduce the potential impact of imperfect modeling of this difference by the MC. Low statistics in the anti-isolated data and MC will also have a negative impact on the background template if there are large statistical fluctuations, so it is important to choose a sufficiently large anti-isolation range. For this analysis, we choose the range $4 < p_\mathrm{T}^\mathrm{iso} < 10$ GeV/c.
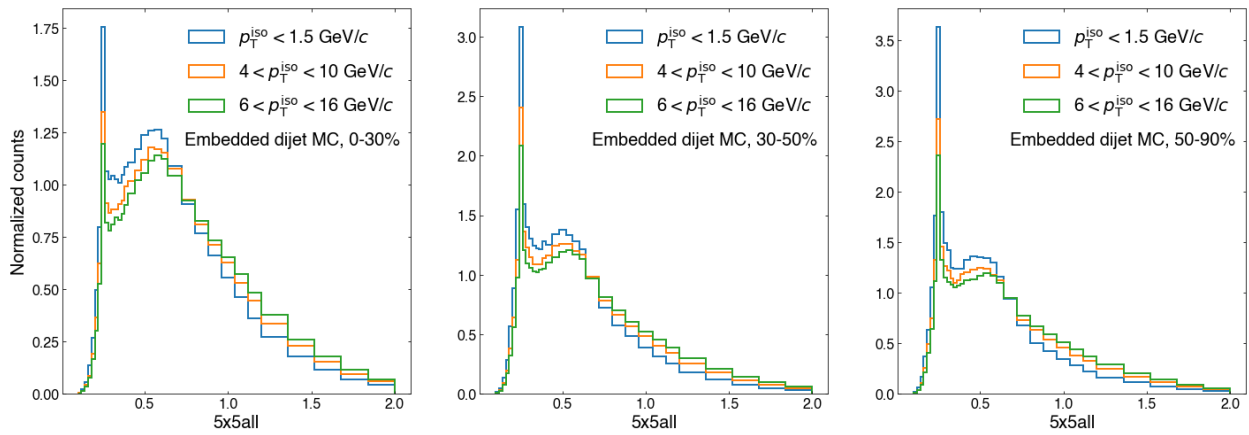
Figure 3.8: $\sigma^2_{\mathrm{long(5x5)}}$ distributions in embedded dijet with the isolation (blue) and two different anti-isolation (orange and green) cuts

With the signal template and the corrected background template, we now fit the isolated data to a linear combination of the two templates. This is a straightforward χ^2 minimization, where the uncertainty is taken as the quadrature sum of the statistical uncertainties of the isolated data and background template (which comes from the anti-isolated data); the statistical uncertainty on the signal template is negligible. The template fits with residuals are shown in Figure 3.9. The purity is then extracted in the signal-like region by taking the ratio of the signal to the sum of the signal and background; in Figure 3.9, this is the ratio of the blue area to the blue + yellow area in the shaded grey region.
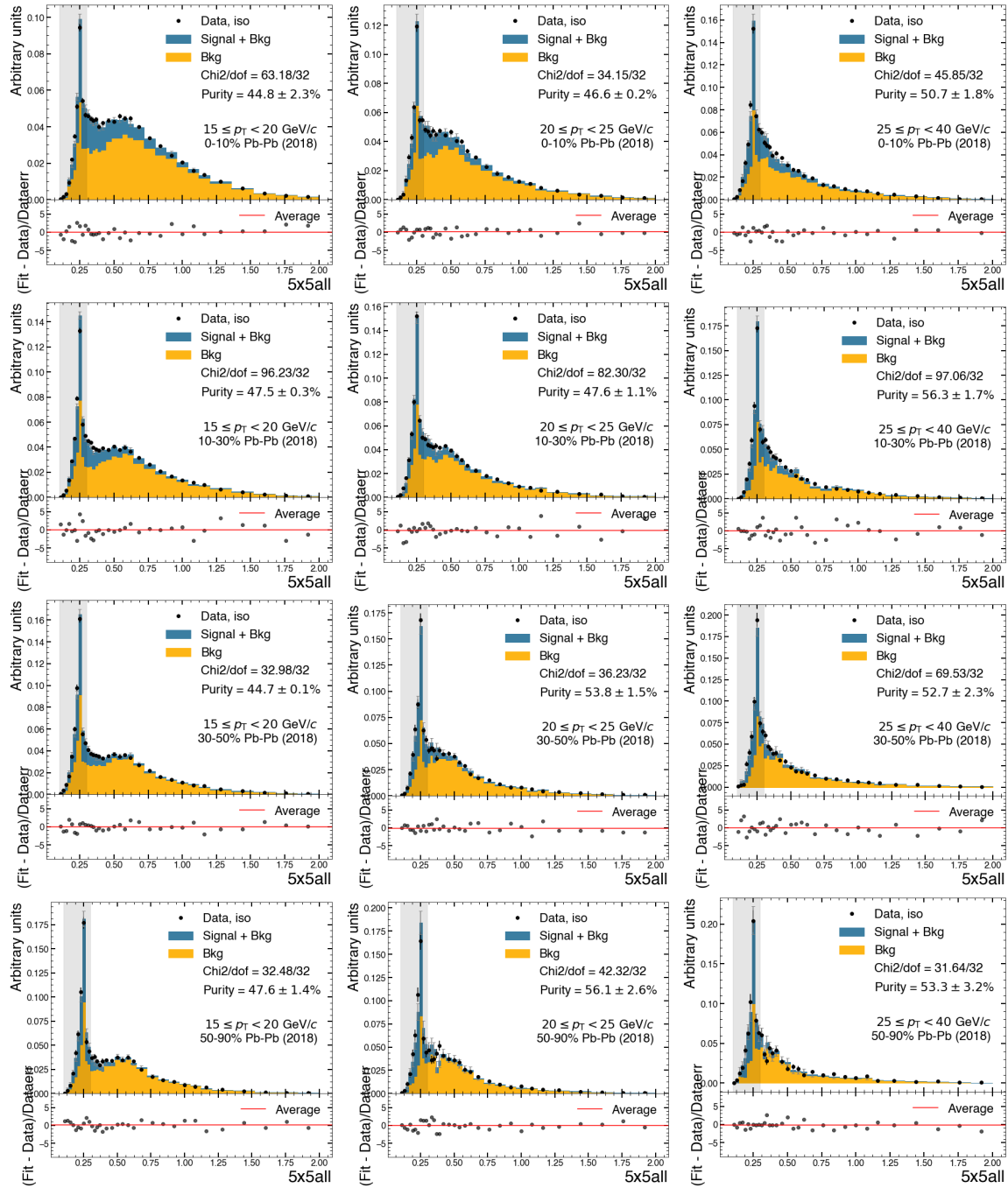
Figure 3.9: Template fits with residuals for different photon p_{T} ranges (left to right) and different centrality ranges (top to bottom)

The template fits are done in bins of photon candidate p_T and centrality; the extracted purities are shown in Figure 3.10. In the more peripheral collisions, the purity increases with p_T; this is consistent with what we saw in pp and p–Pb collisions [27]. To get the statistical uncertainty on the template fit, we take the uncertainty on the fit fraction as calculated by the `iminuit` package (which also does the fit itself) and recalculate the purity with the fit fraction varied by this uncertainty. While the statistical uncertainty on the fit itself seems quite small, it is dwarfed by the systematic uncertainty on the purity (described in the next section), which is what is ultimately propagated to the final observable.
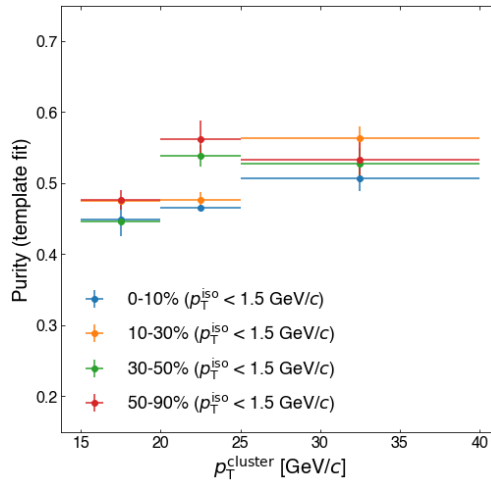
Figure 3.10: Purity as a function of photon candidate p_T

Systematic uncertainties on the photon purity

As was the case in Ref. [27], there are 3 sources of systematic uncertainty associated with the template fit procedure: the uncertainty due to the signal template modeling, the uncertainty due to the anti-isolation selection, and the uncertainty due to the background template correction. They are treated as independent and combined in quadrature to get the total systematic uncertainty on the purity. Section 3.7 describes how this is then propagated to the final measurement.

To estimate the uncertainty due to the signal template modeling, we do a "background-only" template fit in which we remove the signal template entirely. One example of such a fit is shown in Figure 3.11. We fit the data to the background template alone in the range $1.2 < \sigma^2_{\text{long}(5\text{x}5)} < 2.0$, where there is little to no signal (the red region in the right panel of Figure 3.11). This gives a normalization to the background template. We then estimate the purity from this background-only fit by looking again in the signal region, $0.1 < \sigma^2_{\text{long}(5\text{x}5)} < 0.3$, and taking the difference between the data and the background template to be the "signal" (the white space between black points and yellow bars in the

right panels of Figure 3.11). We divide the "signal" by the data to get the purity. We then take the difference between the purity as calculated with this background-only fit and purity as calculated with the full template fit to be the systematic uncertainty due to the signal template.
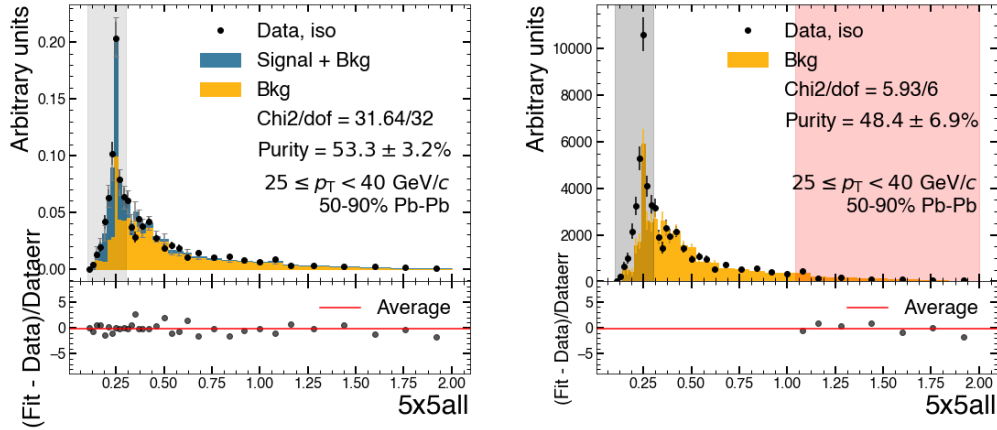
Figure 3.11: A comparison of a template fit (left) with a background-only fit (right) for 50-90%, 25-40 GeV/c clusters. The red region shows the range in which the background template is fit to the data, and the grey regions show where the purity is calculated.

To estimate the uncertainty due to the anti-isolation selection, we repeat the template fits with many different anti-isolation selections. In particular, we look at 4 GeV/c-wide bands of anti-isolation, from 2-6 GeV/c all the way to 16-20 GeV/c, in 0.5 GeV/c increments. With each anti-isolation selection, we calculate the purity and χ^2. One example of this study is shown in Figure 3.12. We then look at the windows within the nominal anti-isolation range (4-10 GeV/c, the green range in Figure 3.12) and treat the purities as a uniform distribution. Therefore, to assign a systematic uncertainty, we take the difference between the maximum and minimum purity calculated within that range (the blue bands in the left panels in Figure 3.12) and divide by $\sqrt{12}$. As an additional check, we make sure that the χ^2 values of those fits are all relatively reasonable.

To estimate the uncertainty due to the background template correction, we evaluate the extent to which the simulation reproduces the relationship between $p_{\mathrm{T}}^{\mathrm{iso}}$ and $\sigma^2_{\mathrm{long(5x5)}}$ by using the following double ratio

$$\text{Double ratio} = \frac{\text{Data}_{\mathrm{iso}}/\text{Data}_{\mathrm{anti\text{-}iso}}}{\text{MC}_{\mathrm{iso}}/\text{MC}_{\mathrm{anti\text{-}iso}}}. \tag{3.6}$$

Note that the denominator is the same as the Weights defined in Equation 3.4. In the region where there is no signal, we expect the double ratio to be flat if the MC reproduces the data. We can therefore fit the double ratio to a single-parameter linear fit in the range $0.7 < \sigma^2_{\mathrm{long(5x5)}} < 1.7$ and extract a slope and an uncertainty on the slope. Some example fits
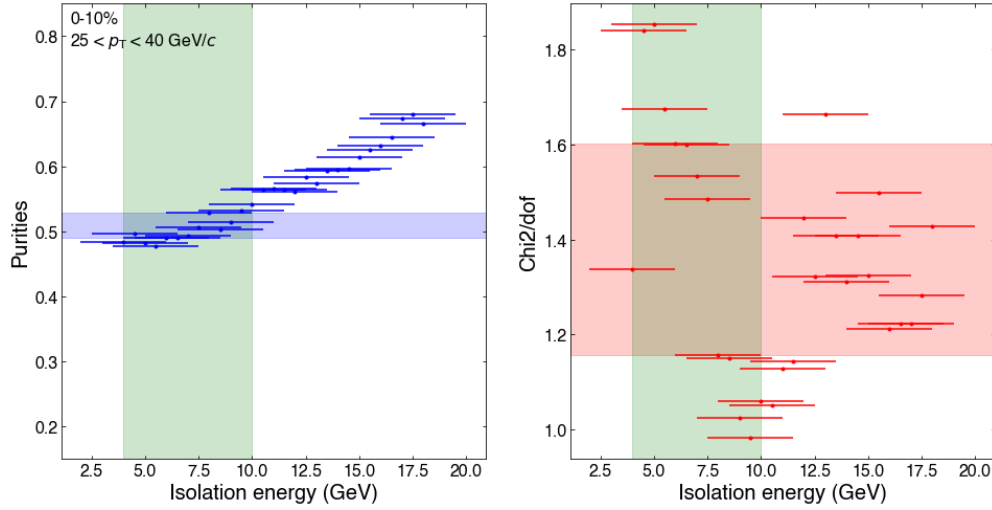
Figure 3.12: The purity (left) and χ^2/dof (right) from the template fit when varying the anti-isolation selection. The horizontal bars represent the range of the anti-isolation selection for that point.

are shown in Figure 3.13, with the uncertainty on the slope represented by the band. The fit in the leftmost panel looks somewhat odd, but the fit procedure is a χ^2 minimization using the `iminuit` package, much like what was done in the template fit itself, and we trust that the numerical procedure does a better job than a visual estimation.
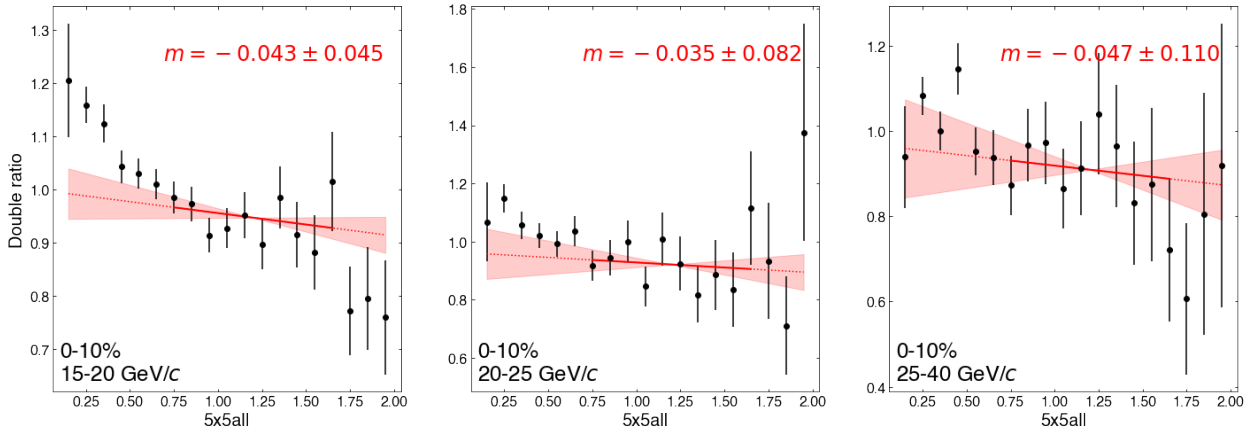
Figure 3.13: Double ratio fits for 0-10% for the three cluster p_T bins

After fitting, the double ratio can be applied as an additional correction to the background template by extrapolating the fit into the signal region and using it as an additional multiplicative factor:

$$\text{Bkg template} = \text{Data}_{\text{anti-iso}} \times \text{Weights} \times \text{Double ratio fit.} \qquad (3.7)$$

If we rewrite this as

$$\text{Bkg template} = \text{Data}_{\text{anti-iso}} \times (\text{MC}_{\text{iso}}/\text{MC}_{\text{anti-iso}}) \times \frac{\text{Data}_{\text{iso}}/\text{Data}_{\text{anti-iso}}}{\text{MC}_{\text{iso}}/\text{MC}_{\text{anti-iso}}}, \qquad (3.8)$$

we can see that, schematically, this results in the background template being an estimate of the isolated non-prompt photons, which is what we want. Since the double ratio fit also has an uncertainty on the slope, we can apply this correction after varying the slope by its uncertainty and taking half the distance in the purity to be the uncertainty. Alternatively, we could consider the difference between the purity without the double ratio correction and the purity with the double ratio correction, but that turns out to often be smaller than the result of propagating the slope uncertainty to the purity. Furthermore, we determine that we do not need to apply the double ratio correction in general, as the slopes are generally consistent with 0 after taking into account the uncertainty on the fit. The full results of the double ratio fit variation are tabulated in Table 3.6.

Table 3.6: Double ratio results and purities calculated when applying the double ratio fit, the double ratio fit with the slope varied up 1σ, and the double ratio fit with the slope varied down 1σ

Centrality	p_{T}^{γ} [GeV/c]	DR slope	P w/ DR	P w/ DR+σ	P w/ DR-σ
0-10%	15-20	-0.0430 ± 0.0451	0.423	0.450	0.395
0-10%	20-25	-0.0347 ± 0.0821	0.448	0.490	0.405
0-10%	25-40	-0.0474 ± 0.1096	0.486	0.535	0.438
10-30%	15-20	-0.0628 ± 0.0578	0.448	0.473	0.423
10-30%	20-25	-0.0429 ± 0.1216	0.461	0.504	0.419
10-30%	25-40	0.0736 ± 0.1502	0.584	0.631	0.541
30-50%	15-20	-0.0446 ± 0.0663	0.429	0.456	0.402
30-50%	20-25	-0.0039 ± 0.1322	0.537	0.577	0.500
30-50%	25-40	0.0138 ± 0.1690	0.530	0.575	0.491
50-90%	15-20	0.0520 ± 0.1070	0.494	0.531	0.458
50-90%	20-25	-0.3148 ± 0.2386	0.498	0.545	0.459
50-90%	25-40	-0.4634 ± 0.3384	0.452	0.508	0.413

The systematic uncertainties on the purity are tabulated in Table 3.7. The total relative uncertainty on the purity amounts to 3.5-7.8%, which is very similar to what was seen in 5 TeV pp collisions [27]. Figure 3.14 plots the photon candidate purity along with the systematic uncertainties as boxes and the statistical uncertainties as error bars.

Table 3.7: Absolute systematic uncertainties on the purity

Centrality	p_{T}^{γ} [GeV/c]	Purity	σ_{stat}	Sig temp	Anti-iso	Bkg temp corr	Total σ_{sys}
0-10%	15-20	0.448	0.023	0.051	0.013	0.027	0.059
0-10%	20-25	0.466	0.002	0.026	0.006	0.042	0.050
0-10%	25-40	0.507	0.018	0.024	0.011	0.048	0.055
10-30%	15-20	0.475	0.003	0.043	0.004	0.025	0.050
10-30%	20-25	0.476	0.011	0.023	0.006	0.043	0.049
10-30%	25-40	0.563	0.017	0.048	0.009	0.045	0.066
30-50%	15-20	0.447	0.001	0.022	0.007	0.027	0.035
30-50%	20-25	0.538	0.015	0.056	0.014	0.038	0.070
30-50%	25-40	0.527	0.023	0.064	0.012	0.042	0.078
50-90%	15-20	0.476	0.014	0.032	0.016	0.037	0.051
50-90%	20-25	0.561	0.026	0.005	0.009	0.043	0.044
50-90%	25-40	0.533	0.032	0.049	0.010	0.047	0.068
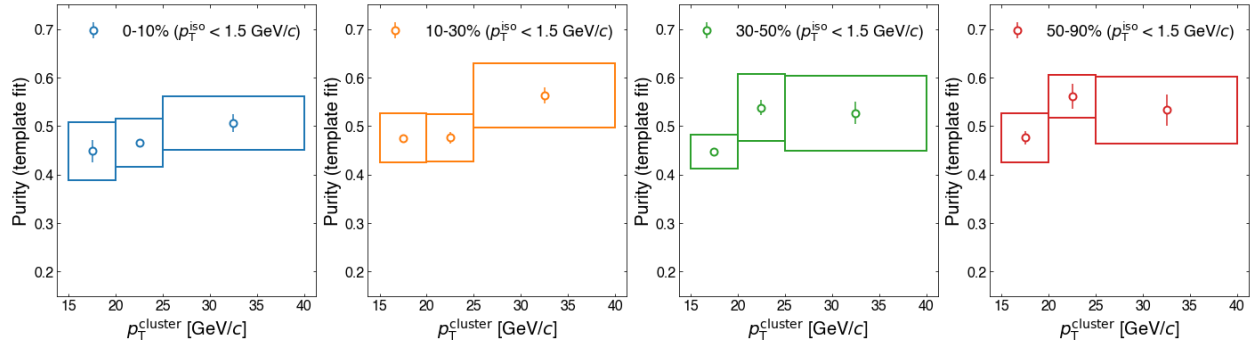
Figure 3.14: Purity vs p_{T}^{γ} with systematic uncertainties drawn as boxes

3.5 Jet reconstruction

Ideally, we would like to know about the parton that was produced in the hard scattering along with the photon. However, due to fragmentation and confinement, we cannot observe the parton directly. As discussed in the introduction, we instead observe jets: the collimated sprays of particles that come from the initial partons. In principle, if we can find all of the particles produced in the hadronization process, we can reconstruct the kinematics of the parton. However, we measure only charged-particle jets, which means that we do not include neutral particles in our jet finding, so on average we see only 60% of the particles [72]. Furthermore, the actual proportion of charged particles in the jet fluctuates jet-by-jet, so for a given charged-particle jet, we cannot know for sure what the actual total energy of the full

(charged + neutral) jet is. Even so, we measure charged-particle jets because our ability to precisely measure full jets is limited by the EMCAL acceptance and performance.

For this analysis, jets are clustered from tracks using the anti-k_T algorithm as implemented in the FastJet software package [18] with the resolution parameter $R = 0.2$. Similar to the photon isolation, the p_T of the jet has the underlying event density ρ scaled by the area of the jet [19] subtracted. This choice of $R = 0.2$, which is relatively small, means that only a fraction of the energy of the parton will be reconstructed by the jet.

There are a few ways to look at how the detector effects and underlying event affect the jet p_T. Generally, using a MC simulation, we match reconstructed jets, which are jets reconstructed from detector-level particles (e.g. after GEANT simulation), to truth jets, which are jets reconstructed from truth-level particles (e.g. the output of PYTHIA before the GEANT simulation). We can then look at the reconstructed jet p_T for different ranges of truth jet p_T, seen in Figure 3.15. The vertical bands represent where each truth p_T range were to be if the reconstructed jet p_T exactly matched the truth p_T. We see clearly that the underlying event and detector effects collectively smear the truth $p_\mathrm{T}^\mathrm{jet}$ distributions.
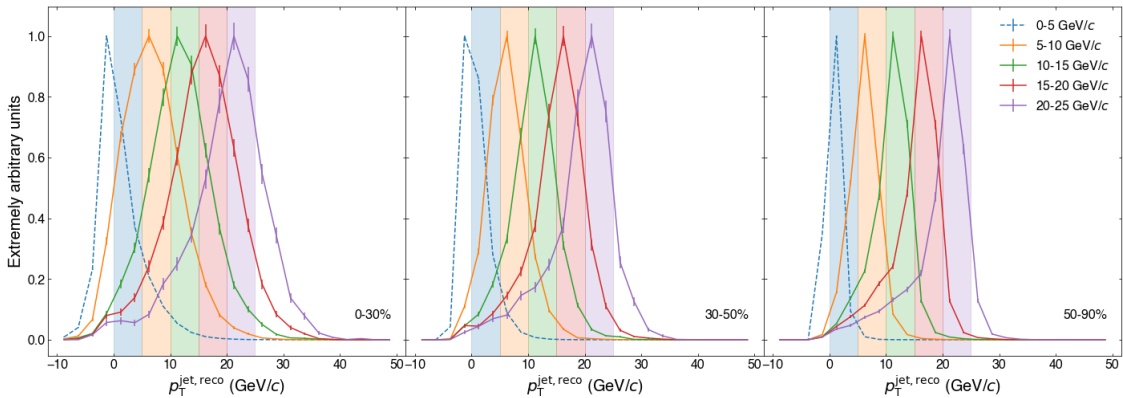
Figure 3.15: Reconstructed $p_\mathrm{T}^\mathrm{jet}$ distributions for different ranges of truth $p_\mathrm{T}^\mathrm{jet}$; colored bands correspond to truth $p_\mathrm{T}^\mathrm{jet}$ ranges

We can also look at the relative difference between the reconstructed and truth jet p_T

$$\frac{p_\mathrm{T}^\mathrm{jet,\ reco} - p_\mathrm{T}^\mathrm{jet,\ truth}}{p_\mathrm{T}^\mathrm{jet,\ truth}}, \tag{3.9}$$

which is shown in Figure 3.16 and from which can be extracted the jet energy scale (JES) and jet energy resolution (JER). We see from this that, in more central collisions, the jet p_T gets smeared more by the larger underlying event. We also see that the effect of the smearing is asymmetric, with jets being more likely to be reconstructed with too little energy rather than too much energy. Because the jet p_T spectrum falls rapidly, more smearing into higher-p_T jets could significantly distort the measurement, but the same amount of smearing

into lower-p_T jets has a much smaller effect. In this case, the long tail is towards lower-p_T jets. I will discuss the impact of the JER and JES in Section 3.8, where a 2D plot of the jet energy response can be found in Figure 3.36.
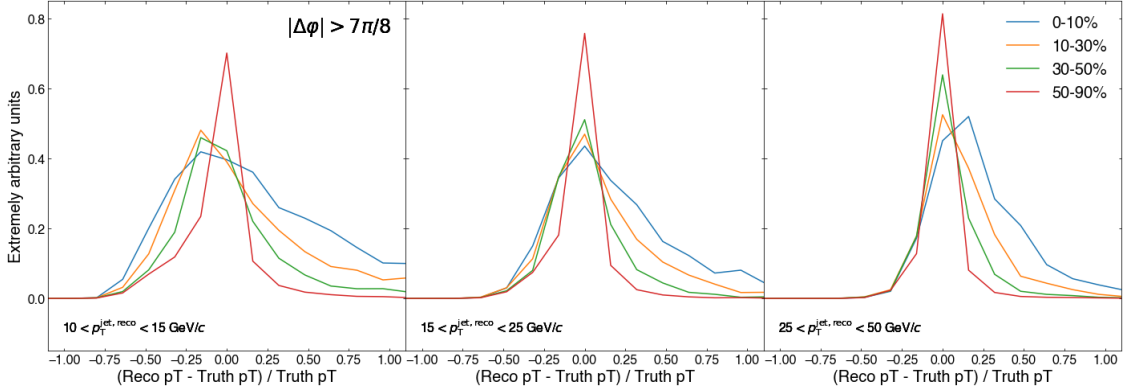
Figure 3.16: Relative difference between reconstructed and truth p_T^{jet} for different reconstructed p_T^{jet} ranges

3.6 Combining photons and jets

To get photon-jet correlations, we take a photon candidate and consider all of the jets in that event. For each of these photon-jet pairs, we measure the angular correlation ($\Delta\varphi = |\varphi_\gamma - \varphi_{jet}|$) and momentum imbalance (p_T^{jet}/p_T^γ). To make this a per-photon correlation, we divide by the total number of photon candidates. This means that effects such as the photon efficiency or event luminosity do not enter into the observable. A "trigger" refers to a photon candidate or equivalent.

The per-trigger correlation between photon candidates and jets has substantial background under both the photon candidates and the jets. As seen in Figure 3.14, the purity of the photon candidate sample is around 50%, and as we will see, the combinatorial background is quite large. I will first discuss event mixing, the technique by which we estimate the combinatorial background, and then I will discuss how these backgrounds are subtracted. For clarity, the "per-trigger yield" will refer to correlations with full background subtraction, and "per-trigger correlations" will refer to intermediate steps.

Event mixing

Event mixing is a technique that can be used to estimate the combinatorial background in a correlation analysis. Conceptually, the measured jets correlated with a photon candidate contain both jets that come from same initial hard scattering as the photon and jets that

do not. The latter population of jets can either be jets from a different hard scattering in the event or be "fake" jets that are reconstructed from the particles in the underlying event. We collectively call these "combinatorial jets," as they correspond to jets that are not physically correlated with the photon and therefore represent a combinatorial background to the photon-jet correlation.

In order to estimate the contribution of combinatorial jets, we take photon candidates from one EMCAL-triggered event and correlate them with jets from a different MB event. MB events can sometimes have jets arising from a hard scattering, but they mostly have fake jets. Particularly in central collisions, events can have multiple hard scatterings, so the mixing also estimates the contribution from jets that come from hard scatterings other than the one that produced the photon. Because the photon and the jets come from different events, there cannot be any true correlation between them. Consequently, the mixed events should represent only the combinatorial background.

Event pairing

We use the Gale-Shapley stable matching algorithm to pair events; this technique was also used in Ref. [27]. Both EMCAL-triggered events and MB events are split into "blocks" of 2000. A block of EMCAL-triggered events is compared with a block of MB events, and the stable matching algorithm is run. The events are paired based on their centrality, 2nd-order event plane angle, and z-vertex. The centrality matching is important to reproduce the multiplicity of the underlying event. The z-vertex matching ensures that the positions of the tracks (and therefore the jets) are similar. The 2nd-order event plane angle gives information about which direction the QGP flows in a given event, so matching in 2nd-order event plane angle ensures that the flow modulation of the underlying event is similar. One block of triggered events is paired with ~ 300 blocks of mixed-events, and this number can be increased if more mixed-event statistics are needed.

While events paired with the stable matching algorithm are often very close to each other in all of the parameters listed above, sometimes they are very different in one or more of these parameters. To prevent such pairs of events from being mixed with each other, an additional set of event similarity criteria are applied to the mixed events:

- $|\Delta\text{centrality}| < 5$

- $|\Delta z\text{-vertex}| < 2$ cm

- $|\Delta 2\text{nd-order event plane angle}| < 0.5$

Background subtractions

In the data, we measure 4 per-trigger correlations: the same-event signal-region (SESR), the same-event background-region (SEBR), the mixed-event signal-region (MESR), and the mixed-event background-region (MEBR). The signal-region and background-region refer to

the EMCAL shower shape, where the "photon candidates" in the BR distributions have a background-like shower shape (large $\sigma^2_{\text{long(5x5)}}$) rather than a signal-like shower shape (small $\sigma^2_{\text{long(5x5)}}$). These per-trigger correlations can be thought of in terms of various components.

First, we have the correlations of photons with jets. These photons can be either prompt photons or non-prompt photons, while the jets can be jets produced in the same hard scattering as the photon or combinatorial jets. We can think of the following 4 combinations:

- S = prompt photon + jet from the same hard scattering

- B = non-prompt photon + jet from the same hard scattering

- U_S = prompt photon + combinatorial jet

- U_B = non-prompt photon + combinatorial jet

We also have a few additional factors that are relatively straightforward:

- P = purity of the photon candidate sample

- A = detector acceptance

- ϵ = detector efficiency

The correlation with all photon candidates (i.e. the shower shape signal region) contains an admixture of the correlation with prompt photons and non-prompt photons, with the fraction given by the photon candidate purity. The same-event correlations can be thought of as a combination of the jets from the same hard scattering and the jets from the underlying event. We can then write the per-trigger correlations from the data as follows:

$$\text{SESR} = A \cdot \epsilon \cdot [P(1 + U_S) + (1 - P)(B + U_B)], \tag{3.10}$$
$$\text{SEBR} = A \cdot \epsilon \cdot [B + U_B], \tag{3.11}$$
$$\text{MESR} = A \cdot \epsilon \cdot [P \cdot U_S + (1 - P) \cdot U_B], \tag{3.12}$$
$$\text{MEBR} = A \cdot \epsilon \cdot [U_B]. \tag{3.13}$$

From this, we can show that

$$\frac{1}{P} \cdot \text{SESR} - \frac{1 - P}{P} \cdot \text{SEBR} - \frac{1}{P} \cdot \text{MESR} + \frac{1 - P}{P} \cdot \text{MEBR} = \boxed{A \cdot \epsilon \cdot S}. \tag{3.14}$$

It is important to ensure that the centrality distribution of the triggers in the mixed-event correlations (MESR and MEBR) match the centrality distribution of the triggers in the same-event correlations (SESR and SEBR). To do so, we calculate the per-trigger yield in 10% centrality bins and then take the weighted average with the weights based on the centrality distribution of the triggers in the same-event correlations. So, for example, for the 30-50% bin, we calculate the per-trigger MESR yield in 30-40% and 40-50%. If we look
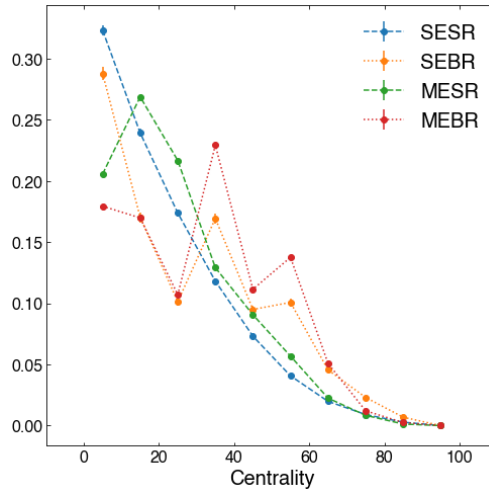
Figure 3.17: Self-normalized centrality distribution of triggers in SESR, SEBR, MESR, and MEBR

at the centrality distributions of triggers as shown in Figure 3.17, we can see that there are roughly twice as many SESR triggers in 30-40% than in 40-50%. So we take the weighted average of the two centralities with those weights, which are approximately 2:1.

Figures 3.18 and 3.19 show the purity-weighted per-trigger correlations SESR, SEBR, MESR, and MEBR as measured in the 2018 data. Subtracting the background region from the signal region gives Figures 3.20 and 3.21. To get a sense of the signal-to-background ratio, we can also plot the total background per-trigger correlation alongside the sum of the signal and background (SESR) in Figures 3.22 and 3.23. Subtracting the mixed event from the same event then gives the per-trigger yield.

Figures 3.24 and 3.25 have the per-trigger yields from both the 2018 and 2015 data, fully-subtracted, independently analyzed using the same procedure. To combine the datasets, we use inverse variance weighting to calculate both the central value and the statistical uncertainty[3].

---

[3]This is not the Bevington [10] method. This is just a straight propagation with partial derivatives of the weighted average.
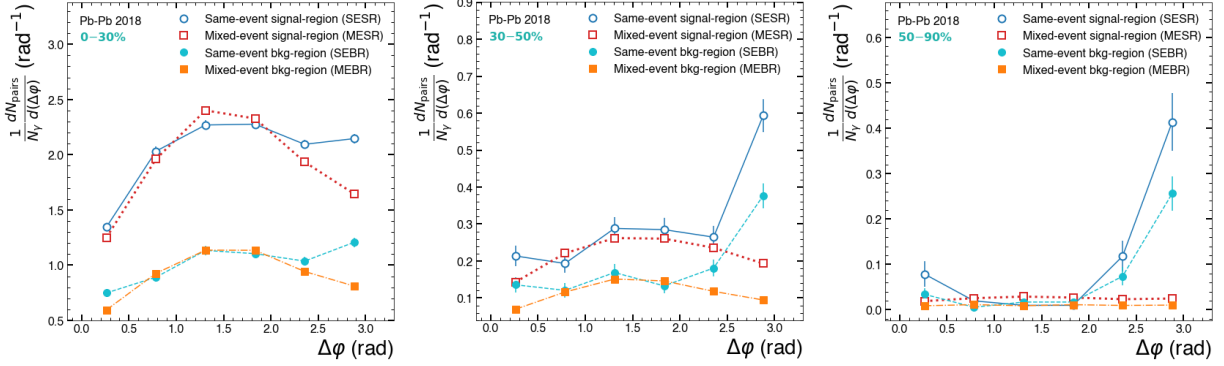
Figure 3.18: Raw $\Delta\varphi$ correlations for 2018 data
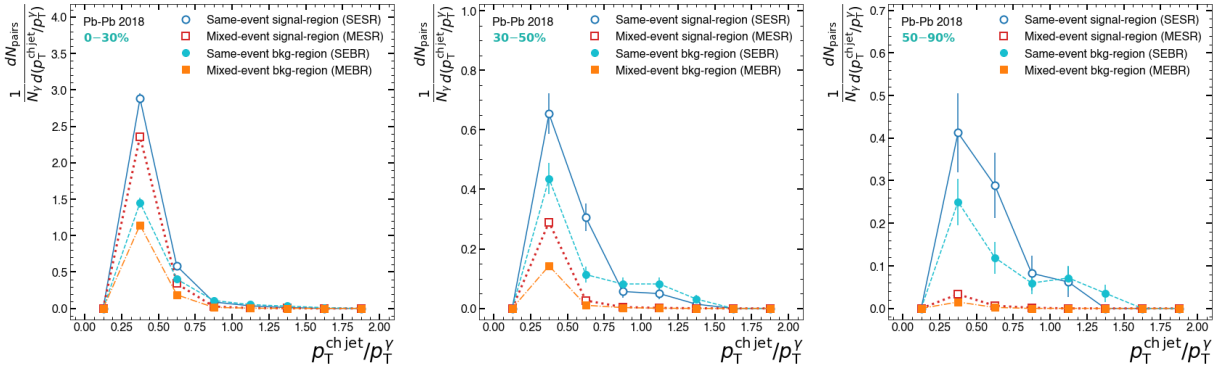
Figure 3.19: Raw $p_T^{\text{jet}}/p_T^{\gamma}$ correlations for 2018 data
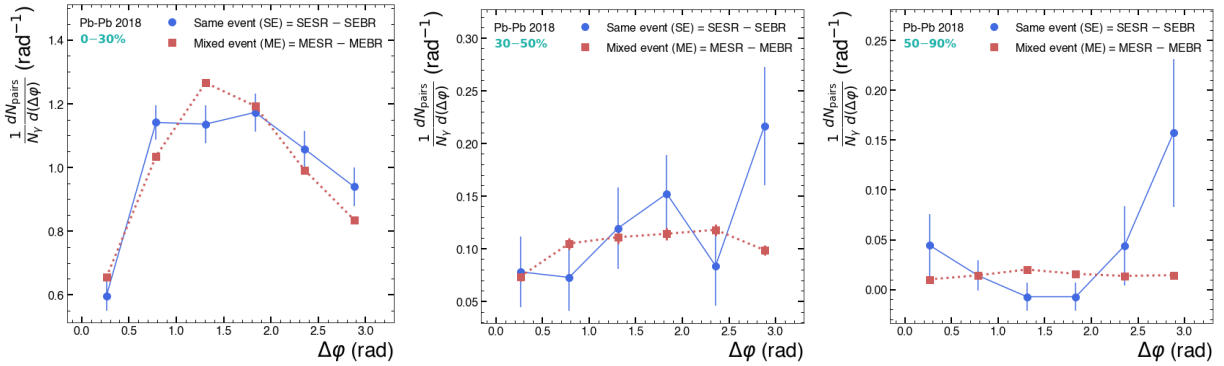
Figure 3.20: BR-subtracted $\Delta\varphi$ correlations for 2018 data
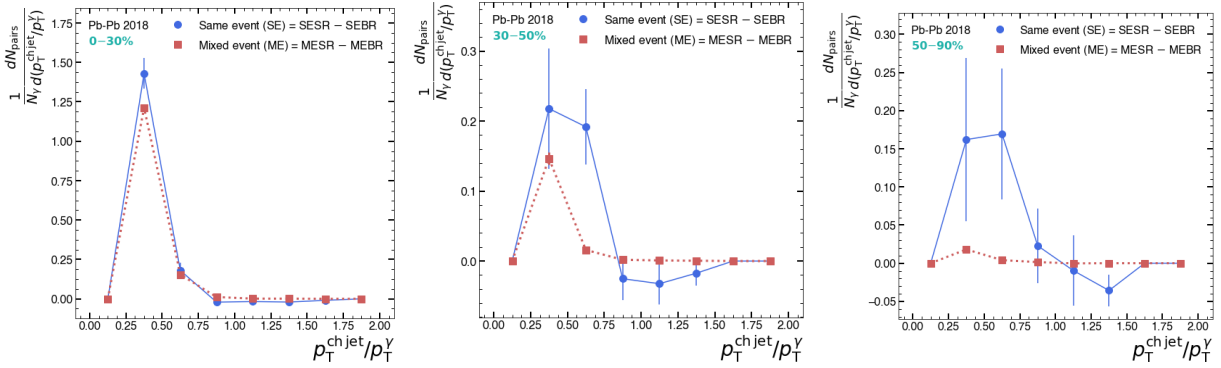
Figure 3.21: BR-subtracted $p_T^{\text{jet}}/p_T^\gamma$ correlations for 2018 data
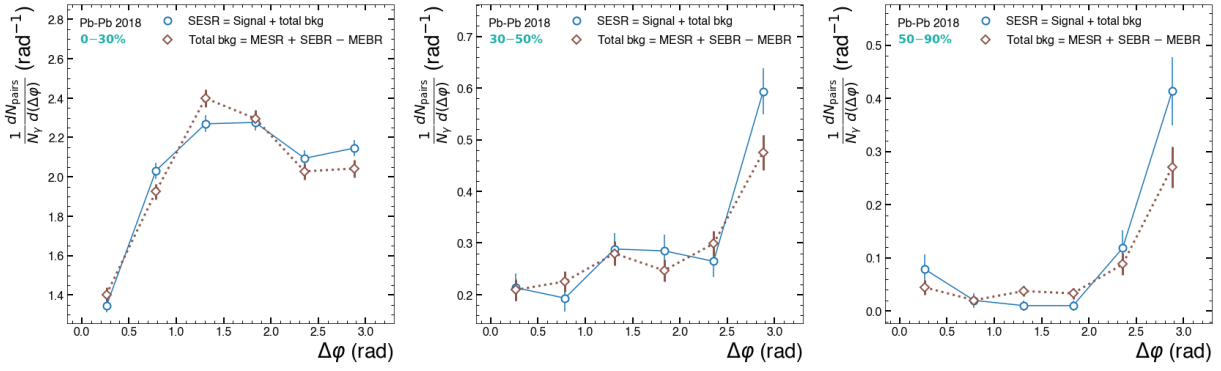
Figure 3.22: Signal and total background $\Delta\varphi$ correlations for 2018 data
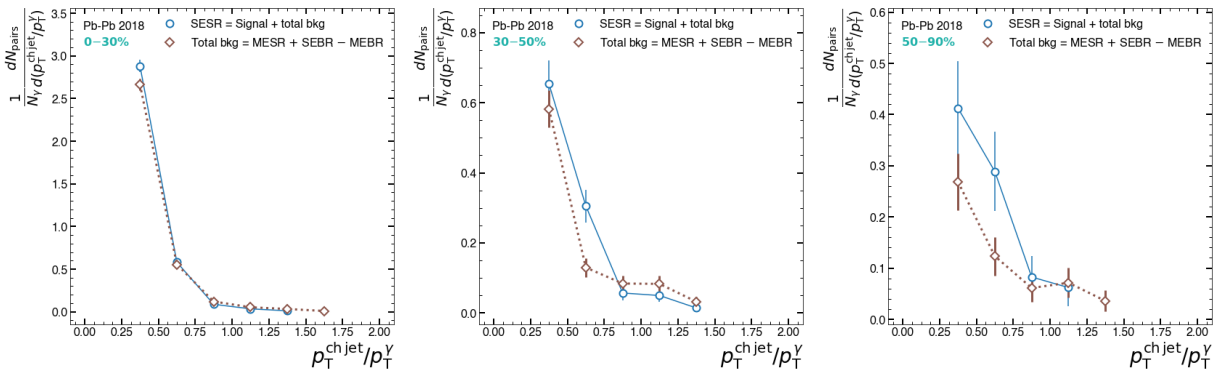
Figure 3.23: Signal and total background $p_T^{\text{jet}}/p_T^\gamma$ correlations for 2018 data
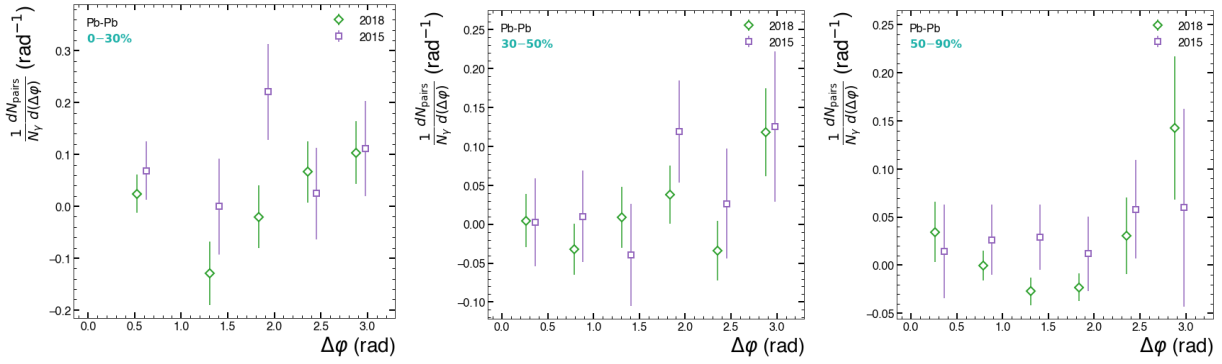
Figure 3.24: Fully-subtracted $\Delta\varphi$ correlations for both 2015 and 2018 data
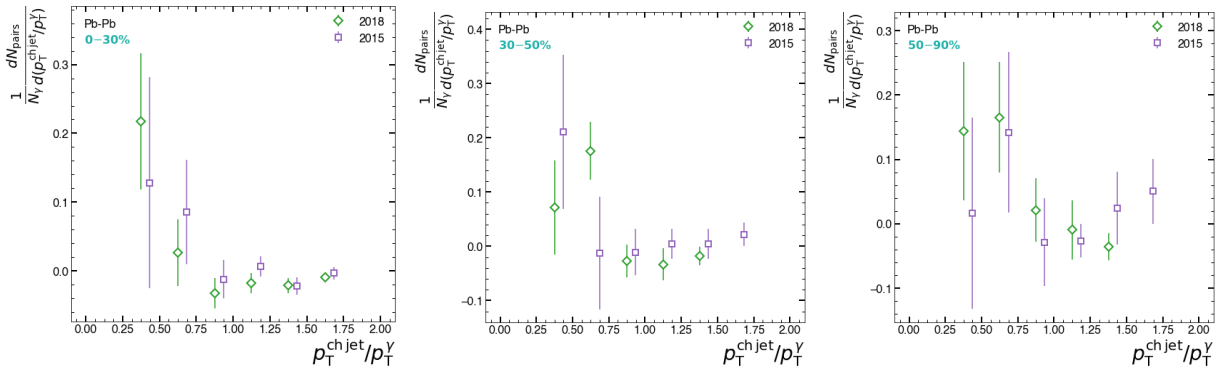
Figure 3.25: Fully-subtracted $p_\mathrm{T}^\mathrm{jet}/p_\mathrm{T}^\gamma$ correlations for both 2015 and 2018 data

3.7 Systematic uncertainties

In this section, I describe the effects of varying different aspects of the analysis in order to evaluate systematic uncertainties on the per-trigger yields. The uncertainty values associated with these variations are summarized at the end of this section. We do these variations on the 2018 data alone to estimate the systematic uncertainty, then assign it to the combined result from the 2015 and 2018 data.

Default analysis parameters

The default analysis parameters are as follows:

- Shower shape variable: $\sigma^2_{\text{long(5x5)}}$

- Shower shape signal region: 0.1–0.3

- Shower shape background region: See Table 3.4

- Isolation radius: $R = 0.2$

- Isolation cut: 1.5 GeV/c

- Anti-isolation range: 4–10 GeV/c

- Photon candidate p_{T} range: 28–40 GeV/c

- Minimum track p_{T}: 0.15 GeV/c

- Jet algorithm: anti-k_{T}

- Jet radius: $R = 0.2$

- Jet p_{T} range: 10–50 GeV/c

- $\Delta\varphi$ cut for $p_{\text{T}}^{\text{jet}}/p_{\text{T}}^{\gamma}$ distribution: $7\pi/8 < \Delta\varphi < \pi$

- Jet p_{T} cut for $\Delta\varphi$ distribution: $10 \text{ GeV}/c < p_{\text{T}}^{\text{jet}} < 1.2 \times p_{\text{T}}^{\text{cluster}}$

- Δcentrality < 5 when pairing events for mixing

Variation of the purity by its systematic uncertainty

In this study, we vary the purity up and down by the systematic uncertainty as described in Section 3.4, then recalculate the per-trigger yield. We take the difference between varying it up and down $1\sigma_{\text{sys}}$ and halve it to get the systematic uncertainty. The resulting $\Delta\varphi$ and $p_{\text{T}}^{\text{jet}}/p_{\text{T}}^{\gamma}$ per-trigger yields are shown in Figures 3.26 and 3.27, respectively. For 0-10%, in the $5\pi/6 < \Delta\varphi < \pi$ bin, this amounts to a 43% relative systematic uncertainty from the purity; for 50-90%, the relative systematic uncertainty from the purity is 16%.
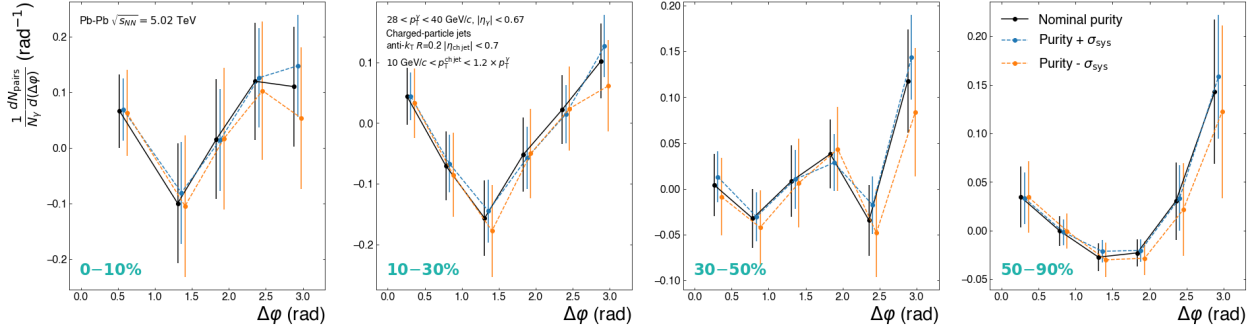
Figure 3.26: Comparison of $\Delta\varphi$ correlations with purity $\pm 1\sigma_{\mathrm{sys}}$ instead of nominal purity
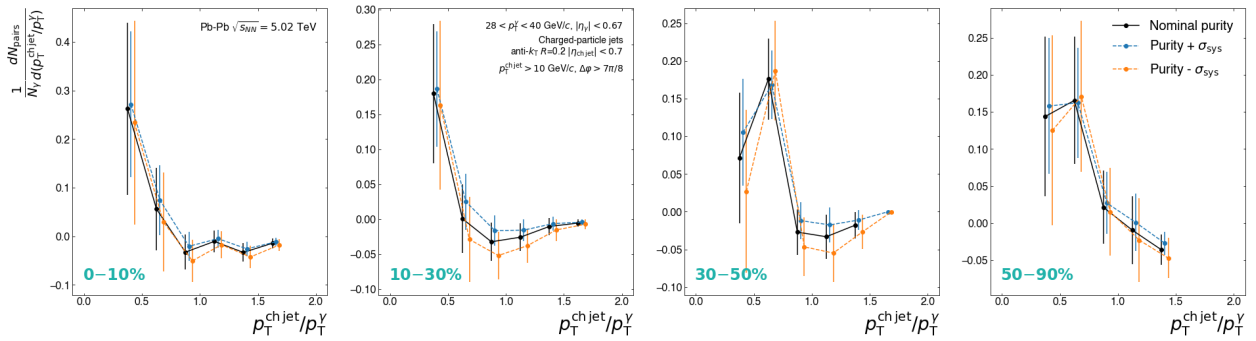
Figure 3.27: Comparison of $p_{\mathrm{T}}^{\mathrm{jet}}/p_{\mathrm{T}}^{\gamma}$ correlations with purity $\pm 1\sigma_{\mathrm{sys}}$ instead of nominal purity

Variation of the shower shape background region

In this study, the lower bound of the shower shape background region is varied up and down by 0.2, except for the 50-90% centrality bin, where it is only varied up. This changes the amount of signal contamination in the background region. The nominal values in Table 3.4 were chosen such that the amount of signal contamination was about 6.5%; these variations change that proportion to about 4.5% (when varying up) and about 8.5% (when varying down). The resulting per-trigger yields from these variations can be seen in Figure 3.28. We take the difference between varying it up and down and halve it to get the systematic uncertainty. For 0-10%, in the $5\pi/6 < \Delta\varphi < \pi$ bin, this amounts to a 100% relative systematic uncertainty from the shower shape background region; for 50-90%, the relative systematic uncertainty from the shower shape background region is 9%.

Variations in the estimation of the combinatorial background

There are a number of variations related to various aspects of the mixed-event correlation used to estimate the combinatorial background. The per-trigger yields for each variation are
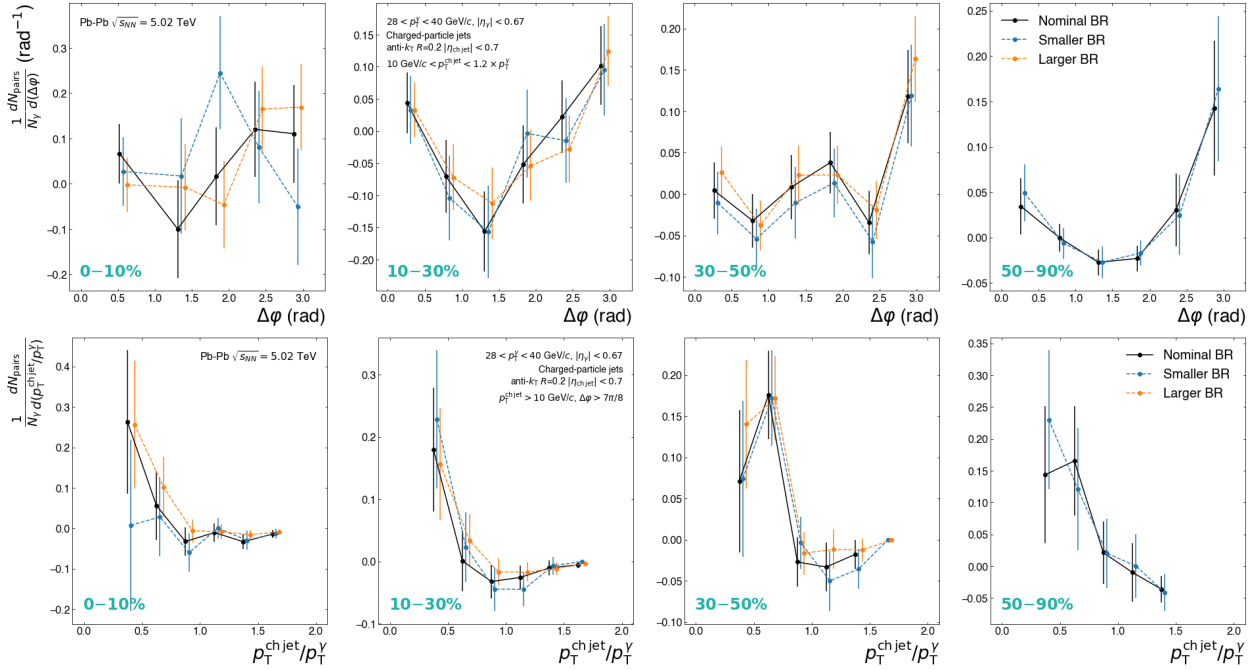
Figure 3.28: Comparison of $\Delta\varphi$ (top) and $p_{\mathrm{T}}^{\mathrm{jet}}/p_{\mathrm{T}}^{\gamma}$ (bottom) correlations with different BR ranges, where "smaller" refers to a range with less signal contamination and "larger" refers to a range with more signal contamination.

shown in Figure 3.29 for $\Delta\varphi$ and Figure 3.30 for $p_{\mathrm{T}}^{\mathrm{jet}}/p_{\mathrm{T}}^{\gamma}$. I describe each variation below, and then I discuss the way a total systematic uncertainty is derived from these various sources.

Variation of the Δcentrality cut when pairing events for mixing

In this study, when pairing the EMCAL-triggered and MB events for event mixing, we allow Δcentrality < 10 instead of Δcentrality < 5. Doing so intentionally exacerbates the problems caused by pairing events that are too dissimilar in order to estimate the effects of the dissimilarity present in the nominal range. The effect can be seen as the dark blue points in Figures 3.29 and 3.30.

Scaling the mixed-event correlations

It is possible for the mixed-event correlation to not be an exact representation of the true correlation with combinatorial jets. There are a few sources that could contribute to this difference. This might include residual mismatch between EMCAL-triggered and MB events when doing the event pairing for the event mixing. Another source might be that the underlying event in an event with a hard scattering is not identical to a MB event. By default, we do not try to correct for this difference, as we do not truly understand the shape
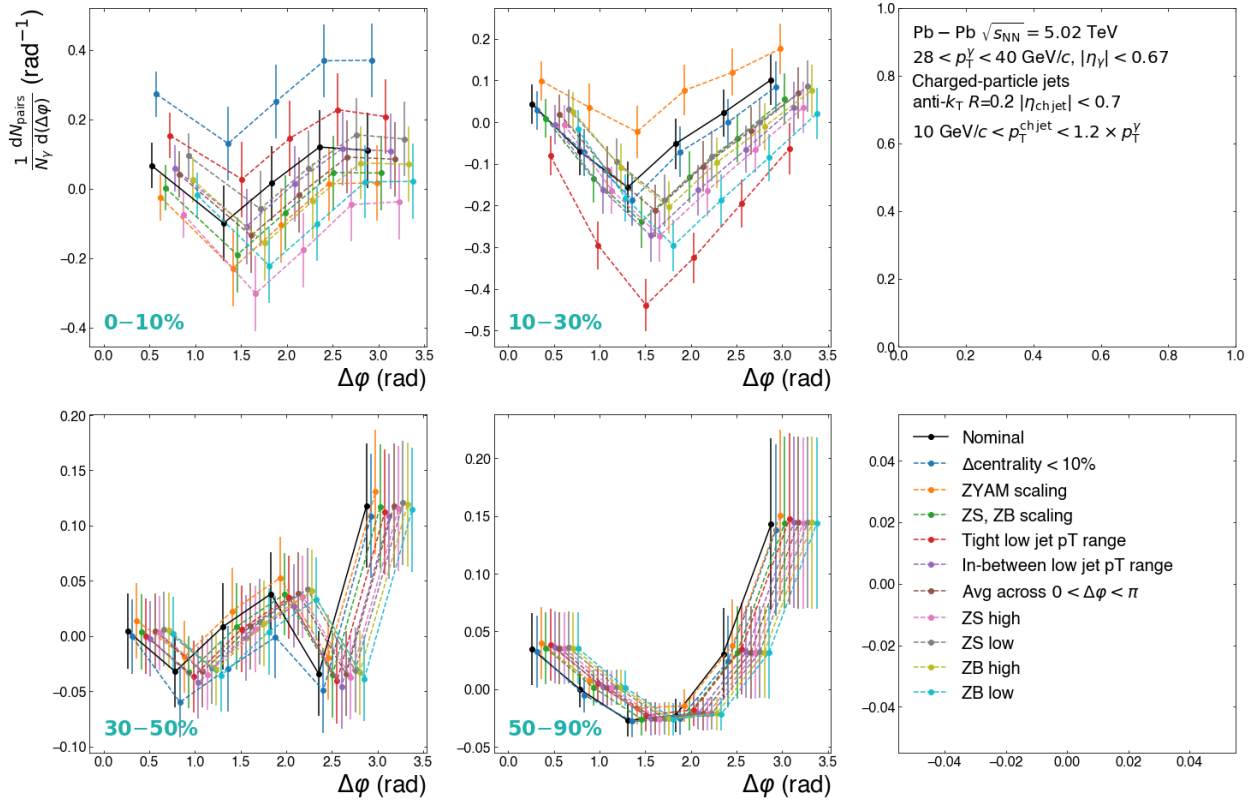
Figure 3.29: Comparison of $\Delta\varphi$ correlations with different variations on the mixed-event correlations

and magnitude of such a correction. However, we attempt various types of corrections in order to estimate the systematic uncertainty due to the possible discrepancy between the combinatorial background and the mixed-event correlation.

In the "simplest" case, we can define a single multiplicative factor such that the final fully-subtracted correlation has an average value of 0 over the two bins in $\pi/6 < \Delta\varphi < \pi/2$. This forces there to be no yield, on average, in that region of $\Delta\varphi$, and the effect of this can be seen as the orange points labeled "ZYAM scaling" in Figures 3.29 and 3.30. This Zero Yield At Minimum (ZYAM) assumption is relatively common for correlation analyses, but we choose not to force it in this analysis.

A more complicated way to try to estimate the effect of this discrepancy is to define constant multiplicative factors, ZS and ZB, on MESR and MEBR respectively. To get the values of ZS or ZB, we look for some region where we believe the same-event correlation consists almost entirely of combinatorial background. Then, in that region, the ratio of the same-event to the mixed-event can be used to properly scale the mixed-event correlation.

In this study, we look at low-p_{T} jets in a $\Delta\varphi$ region away from 0 and π. There are a few
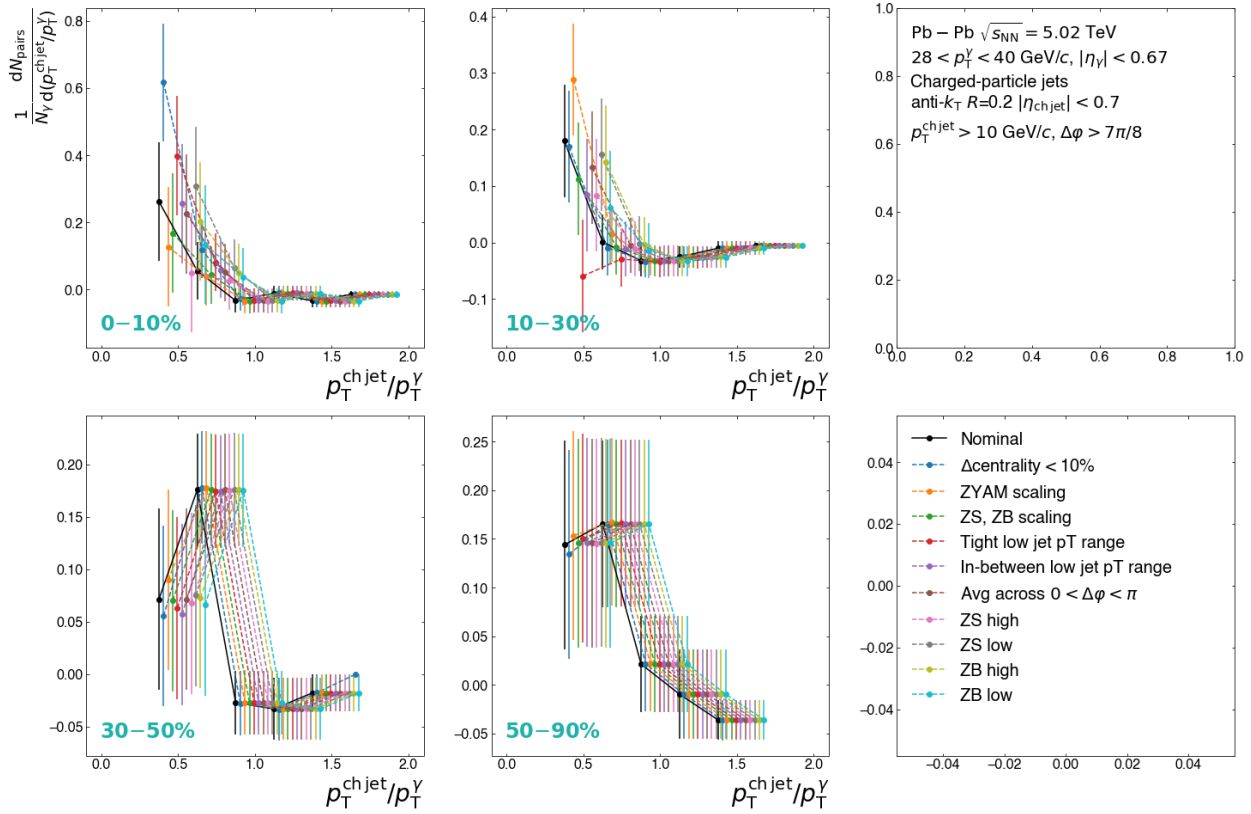
Figure 3.30: Comparison of $p_{\mathrm{T}}^{\mathrm{jet}}/p_{\mathrm{T}}^{\gamma}$ correlations with different variations on the mixed-event correlations

assumptions that go into this kind of determination of the mixed-event correlation correction. First, we assume a flat multiplicative correction across all $\Delta\varphi$. Second, we assume that the multiplicative correction for very low-p_{T} jets is the same as the multiplicative correction for our actual jets of interest. That is, we assume that the extent to which the mixed-event correlation and the true combinatorial background differ from each other is the same for different jet p_{T} regions. Finally, we assume that this combination of very low-p_{T} jets and avoiding 0 and π in $\Delta\varphi$ results in only combinatorial jets. We do some variations on this mixed-event scaling method to address the effects of these assumptions.

Due to spatial fluctuations in the underlying event, jets can sometimes be reconstructed with negative p_{T}. Most jets that end up with negative reconstructed p_{T} have fairly small p_{T} to begin with, as seen in Figure 3.15. Since we are looking for jets that are produced in the same hard scattering as a photon with at least $p_{\mathrm{T}} > 28$ GeV/c, we expect that the majority of negative-p_{T} jets are combinatorial. To further avoid signal jets, we place a stricter upper bound on the more central collisions. So our "very low-p_{T} jets" consist of jets reconstructed with $-10 < p_{\mathrm{T}} < 0$ GeV/c for the 30-50% and 50-90% centralities and $-10 < p_{\mathrm{T}} < -2$ GeV/c

for 0-10% and 10-30%.
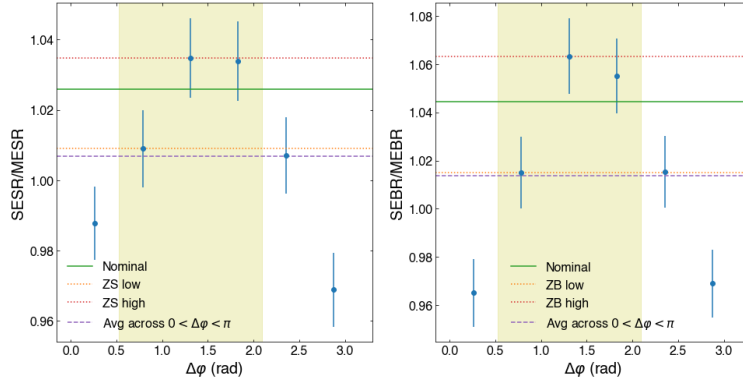
Figure 3.31: SESR/MESR and SEBR/MEBR as a function of $\Delta\varphi$ for jets with $-10 < p_\mathrm{T} < -1$ GeV/c in 30-50% Pb–Pb collisions

Figure 3.31 shows an example of the ratios SESR/MESR and SEBR/MEBR for the $\Delta\varphi$ distributions for these very low-p_T jets. We see that these are not flat with $\Delta\varphi$. In order to avoid signal jets, we do not consider $\Delta\varphi > 2\pi/3$. Also, in order to avoid effects from the isolation cut, we do not consider $\Delta\varphi < \pi/6$. Therefore, we take the average of the 3 points between $\pi/6 < \Delta\varphi < 2\pi/3$ to get ZS and ZB, as indicated by the solid line in Figure 3.31. These values are given in Table 3.8 and the effect of these scales can be seen as the green points in Figures 3.29 and 3.30 labeled "ZS, ZB scaling".

We can take different values of ZS and ZB based on the SE/ME ratios. One variation is to take the maximum and minimum values of the SE/ME ratio within $\pi/6 < \Delta\varphi < 2\pi/3$. These are indicated by the dotted lines in Figure 3.31. We vary one of ZS or ZB up or down while keeping the other at its nominal value and then recalculate the fully-subtracted correlations; the effect of using these different scales are seen in Figures 3.29 and 3.30 labeled as "ZS/ZB high/low". Another variation is to take the average values within $0 < \Delta\varphi < \pi$, indicated by the dashed line in Figure 3.31, and recalculate the fully-subtracted correlations; the effect of this can be seen in the brown points in Figures 3.29 and 3.30 labeled "Avg across $0 < \Delta\varphi < \pi$". These variations account for the possibility that ZS and ZB may not be flat in $\Delta\varphi$.

We can vary the upper bound of the very low-p_T jet range used to determine ZS and ZB. As we do so, we change the number of signal jets contaminating what should be an estimate of the pure combinatorial background. However, since the level of combinatorial background changes as well, it's difficult to say how the fraction of signal contamination changes. This study also attempts to address the question of whether the multiplicative factor for very low-p_T jets can be used for higher-p_T jets as well. By varying the upper bound, we probe how ZS and ZB might be different for different jet p_T ranges and therefore estimate the

Table 3.8: Nominal values of ZS and ZB

Centrality	ZS	ZB
0-10%	1.05	1.05
10-30%	1.10	1.10
30-50%	1.03	1.04
50-90%	0.98	1.08

effect that this assumption might have on our fully-subtracted correlation. The effect of this can be seen in the red and purple points in Figures 3.29 and 3.30.

Total systematic uncertainty from the combinatorial background

The resulting per-trigger yields from these different variations are summarized in Figure 3.29 for $\Delta\varphi$ and Figure 3.30 for $p_{\mathrm{T}}^{\mathrm{jet}}/p_{\mathrm{T}}^{\gamma}$. In order to evaluate the total systematic uncertainty from the combinatorial background, which is to say the total systematic uncertainty on the mixed-event correlation, we start by taking the full spread of the above variations. We take this to be a uniform distribution, so to convert it to 1σ, we divide by $\sqrt{12}$. We then subtract the statistical uncertainty in quadrature. The result is the systematic uncertainty due to the mixed-event; if it is negative after the subtraction, it is set to 0. For 0-10%, in the $5\pi/6 < \Delta\varphi < \pi$ bin, this amounts to a 43% relative systematic uncertainty from the combinatorial background; for 50-90%, the systematic uncertainty from the combinatorial background goes to 0, as it is smaller than the statistical uncertainty.

Total systematic uncertainty on the per-trigger yields

To get the total systematic uncertainty on the per-trigger yields as a function of $\Delta\varphi$ and $p_{\mathrm{T}}^{\mathrm{jet}}/p_{\mathrm{T}}^{\gamma}$, we add the three sources (photon candidate purity, shower shape background region, mixed event) in quadrature; this is summarized in Figures 3.32 and 3.33. The dominant systematic uncertainty comes from the uncertainty on the shower shape background region, except for the $\Delta\varphi$ distribution in 10-30%, where the uncertainty from the combinatorial background dominates.
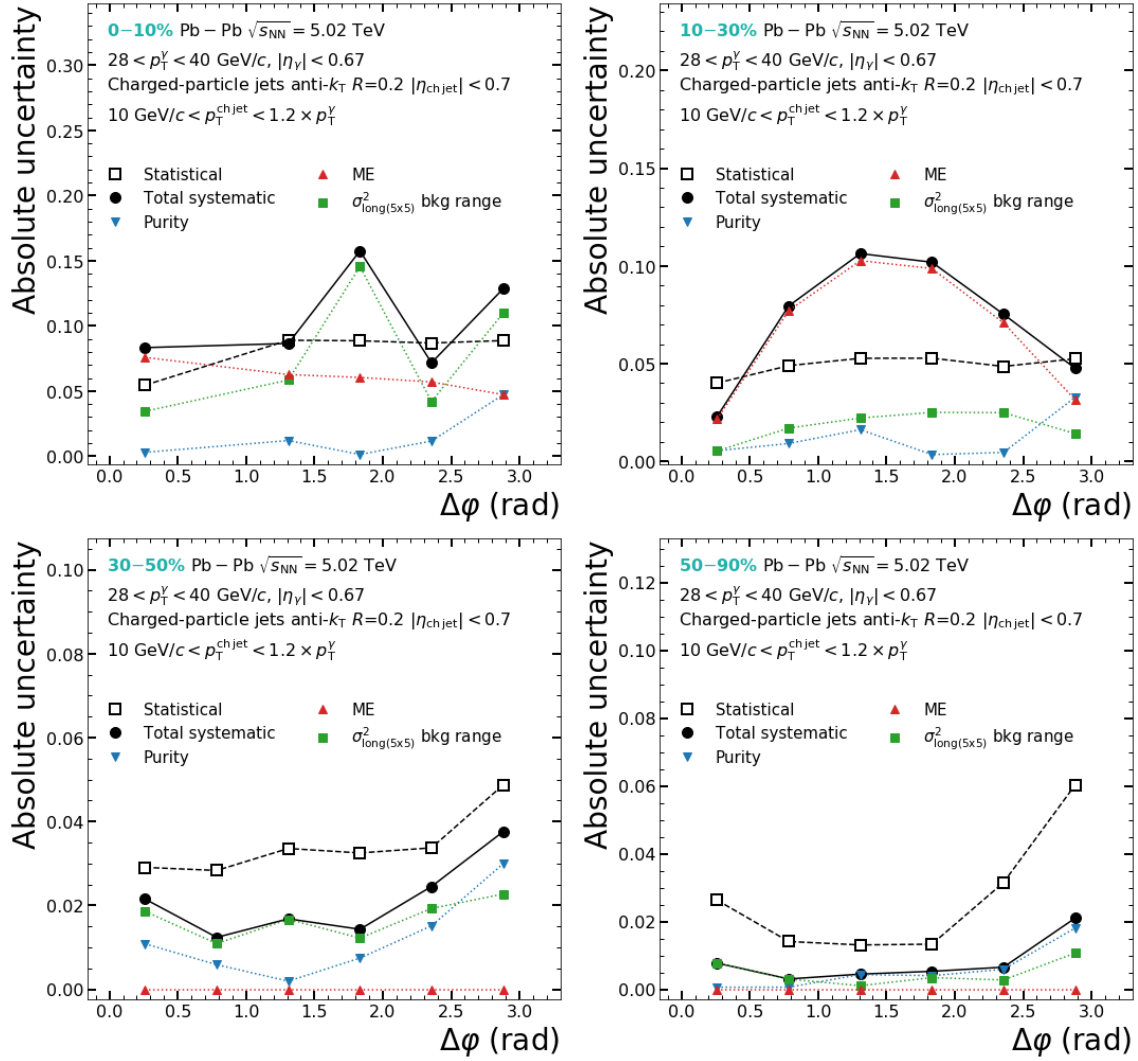
Figure 3.32: Summary of systematic uncertainties for $\Delta\varphi$
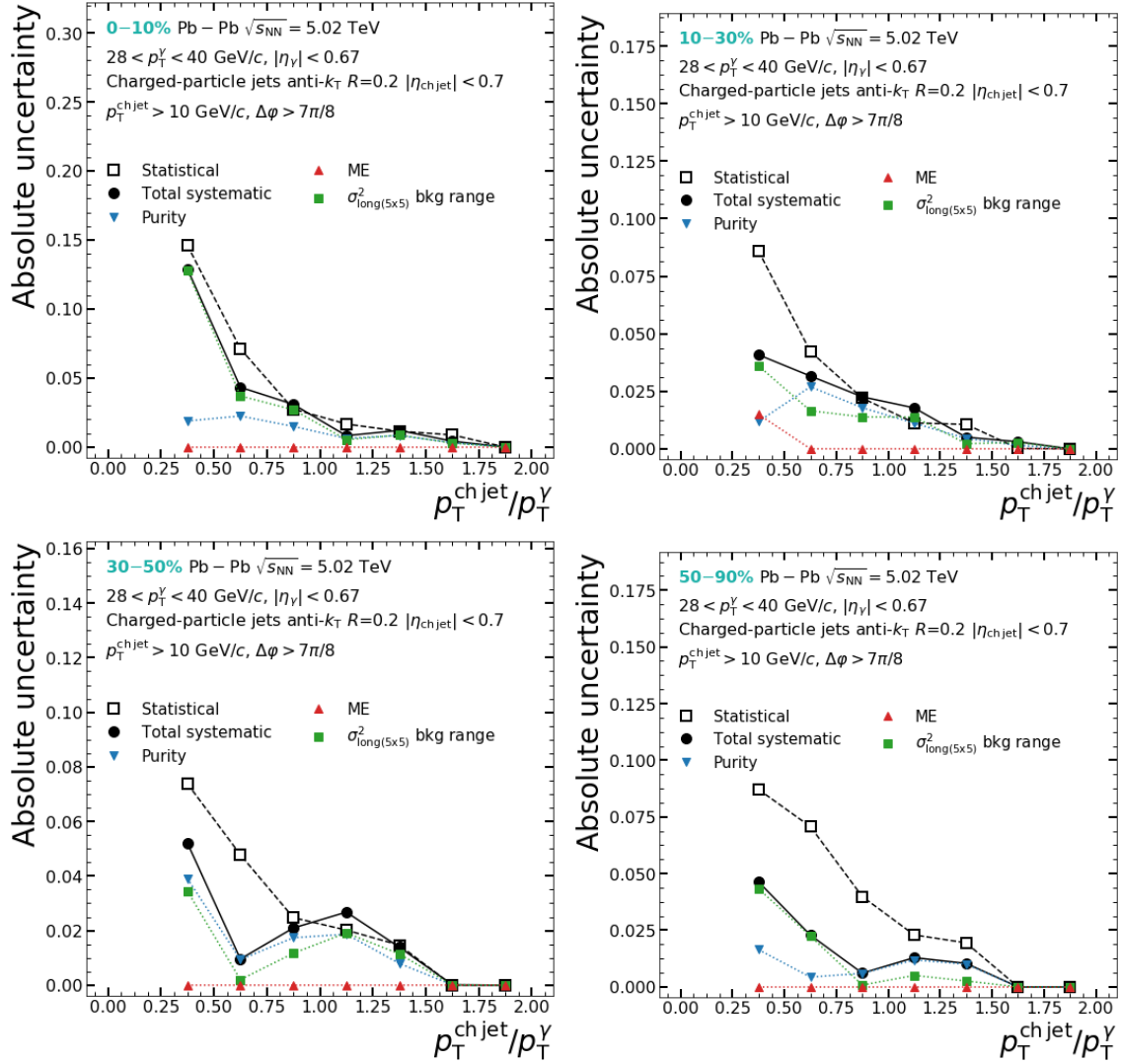
Figure 3.33: Summary of systematic uncertainties for $p_{\mathrm{T}}^{\mathrm{jet}}/p_{\mathrm{T}}^{\gamma}$

3.8 Detector response

In principle, we should unfold these distributions to account for detector effects and residual underlying event effects, including the effects of the jet energy resolution and jet energy scale. Using our embedded MC simulation, we create a response matrix to encode the relationship between the "truth" and "measured" (or "reconstructed") quantities. Unfolding then "unapplies" the detector effects via a sophisticated version of matrix inversion, typically done using RooUnfold [13], and converts a measured distribution to something closer to the distribution that would be measured with a perfect detector. Unfortunately, the attempts

at unfolding this analysis were unstable and therefore unsuccessful. Figure 3.34 shows the results of attempting to use Bayesian unfolding to unfold the data, and it is clear that the statistical uncertainties grow uncontrollably with this procedure due to the limited statistical precision of the measurement itself.
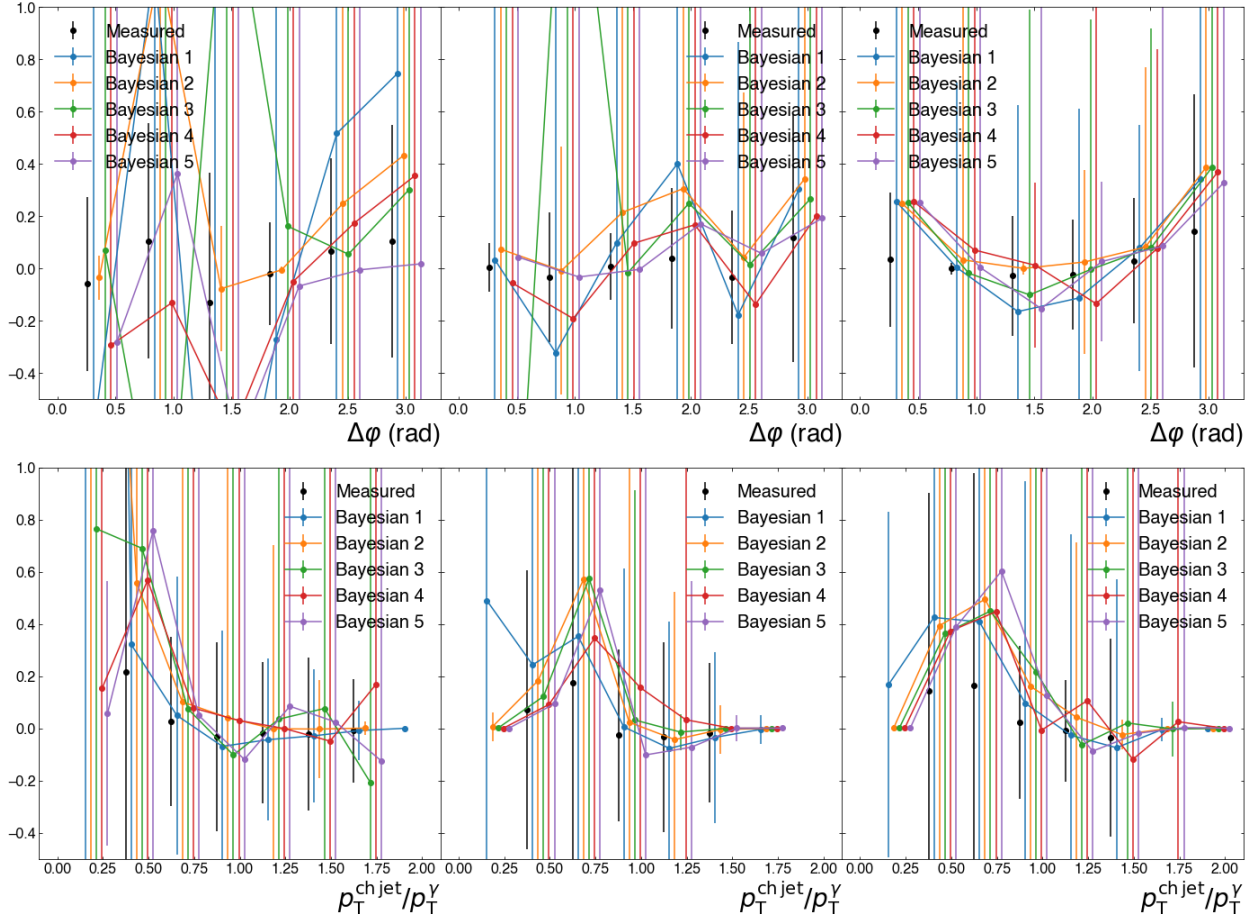
Figure 3.34: Results of attempts at using Bayesian unfolding to unfold the data; even a small number of iterations cause the uncertainties to grow uncontrollably

However, we can still compare to theory calculations by forward folding the theoretical predictions, which is essentially a straightforward matrix multiplication to apply detector effects, which means we can use the same response matrix for different calculations. In general, we want to do a 2-dimensional unfolding (or folding) in order to capture the effect of the shifts in the jet p_T. This means we have 4-dimensional response matrices where two of the axes are the truth and reconstructed charged-particle jet p_T and the other two axes are the truth and reconstructed observable ($\Delta\varphi$ or p_T^{jet}/p_T^{γ}).

Figure 3.35 shows two projections of the $\Delta\varphi$ response matrix, with the truth distribution

on the vertical axis and the reconstructed distribution on the horizontal axis. We can see that there is significant smearing in the $p_{\mathrm{T}}^{\mathrm{jet}}$ distribution but that the $\Delta\varphi$ response is fairly strongly diagonal. Therefore, we would expect that folding or unfolding a $\Delta\varphi$ distribution might result in significant changes to the yield/magnitude but relatively little change in the shape.
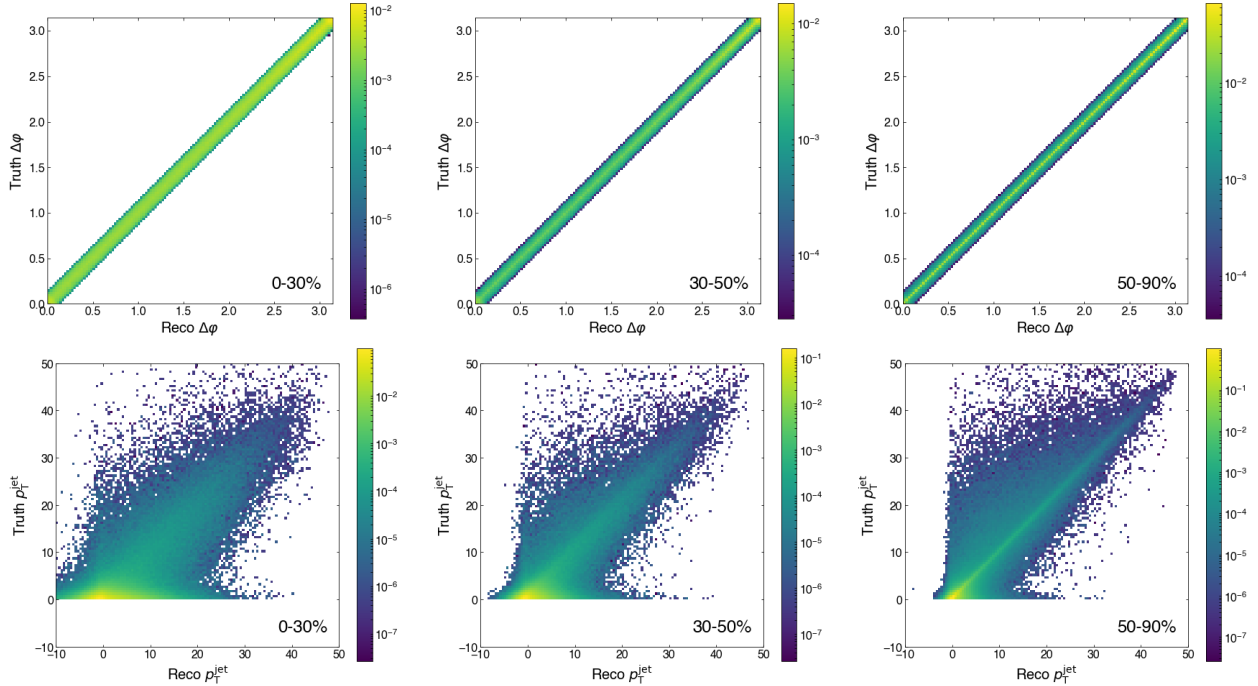
Figure 3.35: Projections of the $\Delta\varphi \otimes p_{\mathrm{T}}^{\mathrm{jet}}$ 4D response matrix. Top: reco vs truth $\Delta\varphi$. Bottom: reco vs truth $p_{\mathrm{T}}^{\mathrm{jet}}$

Figure 3.36 shows two projections of the $p_{\mathrm{T}}^{\mathrm{jet}}/p_{\mathrm{T}}^{\gamma}$ response matrix, with the truth distribution on the vertical axis and the reconstructed distribution on the horizonatal axis. Since $p_{\mathrm{T}}^{\mathrm{jet}}/p_{\mathrm{T}}^{\gamma}$ involves $p_{\mathrm{T}}^{\mathrm{jet}}$, we are not surprised to see that the response matrices look fairly similar. Looking at truth $p_{\mathrm{T}}^{\mathrm{jet}}/p_{\mathrm{T}}^{\gamma}$ vs truth $p_{\mathrm{T}}^{\mathrm{jet}}$ in Figure 3.37, we see that, as expected, there is a linear relationship between the $p_{\mathrm{T}}^{\mathrm{jet}}/p_{\mathrm{T}}^{\gamma}$ and $p_{\mathrm{T}}^{\mathrm{jet}}$, with the slope boundaries defined by the photon p_{T} range. Since neither reco-truth projection is diagonal, we might expect changes in both the magnitude and shape when folding a $p_{\mathrm{T}}^{\mathrm{jet}}/p_{\mathrm{T}}^{\gamma}$ distribution. In particular, as we see in Figure 3.38, there are a substantial number of jets with very low truth $p_{\mathrm{T}}^{\mathrm{jet}}/p_{\mathrm{T}}^{\gamma}$ that get reconstructed with a higher $p_{\mathrm{T}}^{\mathrm{jet}}/p_{\mathrm{T}}^{\gamma}$, particularly for the lowest bins of reconstructed $p_{\mathrm{T}}^{\mathrm{jet}}/p_{\mathrm{T}}^{\gamma}$ for the most central collisions. This means that when we fold a $p_{\mathrm{T}}^{\mathrm{jet}}/p_{\mathrm{T}}^{\gamma}$ distribution, we should expect to see an excess in the 0.25–0.5 bin relative to larger values of $p_{\mathrm{T}}^{\mathrm{jet}}/p_{\mathrm{T}}^{\gamma}$.
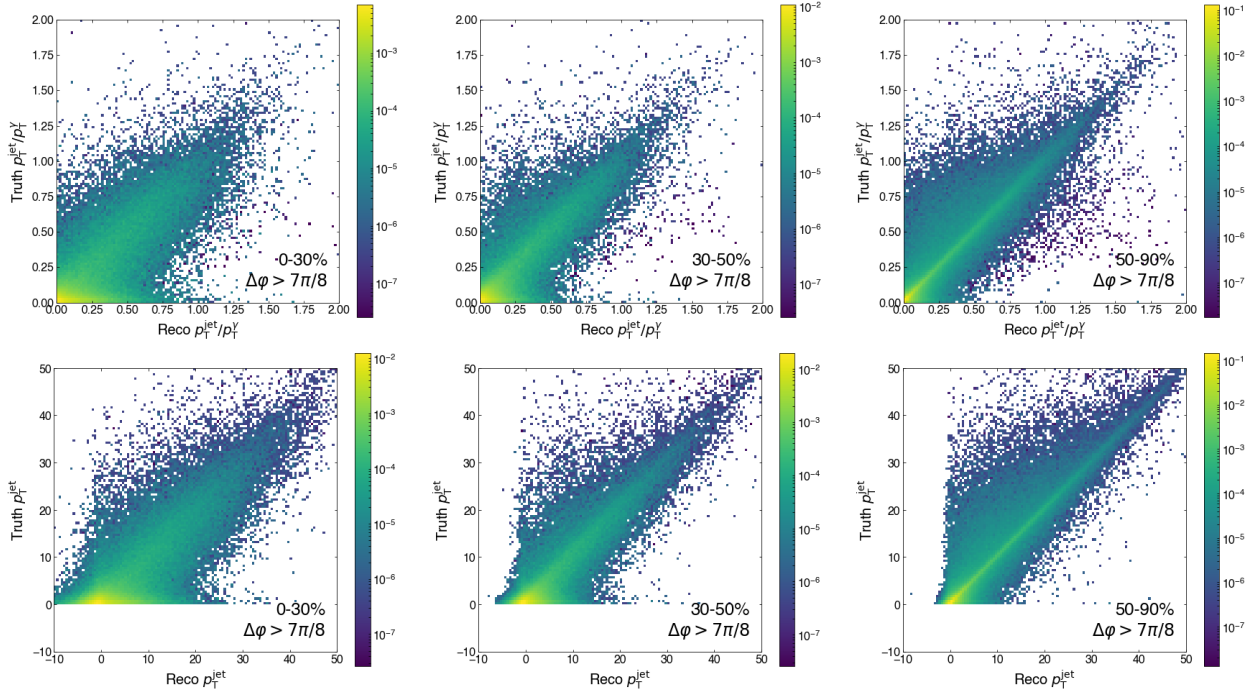
Figure 3.36: Projections of the $p_{\mathrm{T}}^{\mathrm{jet}}/p_{\mathrm{T}}^{\gamma} \otimes p_{\mathrm{T}}^{\mathrm{jet}}$ 4D response matrix. Top: reco vs truth $p_{\mathrm{T}}^{\mathrm{jet}}/p_{\mathrm{T}}^{\gamma}$. Bottom: reco vs truth $p_{\mathrm{T}}^{\mathrm{jet}}$ for back-to-back jets
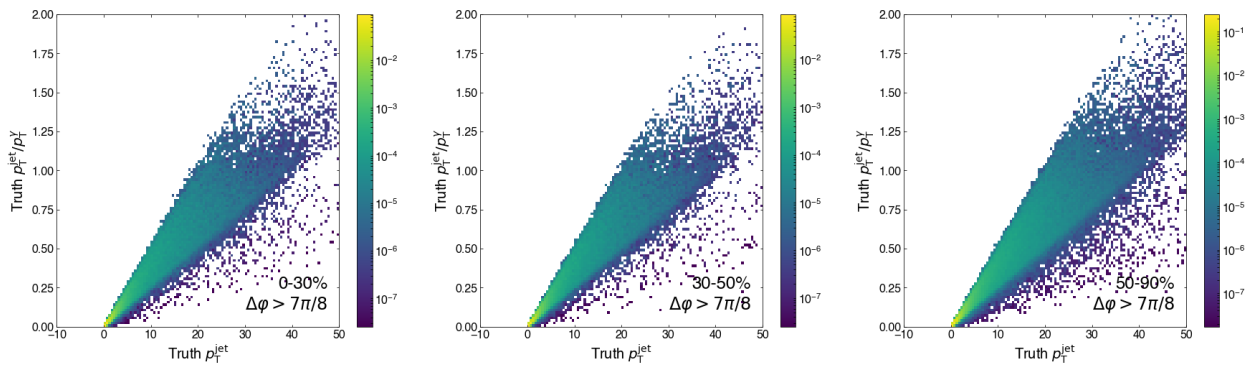
Figure 3.37: Projection of the $p_{\mathrm{T}}^{\mathrm{jet}}/p_{\mathrm{T}}^{\gamma} \otimes p_{\mathrm{T}}^{\mathrm{jet}}$ 4D response matrix, with truth $p_{\mathrm{T}}^{\mathrm{jet}}/p_{\mathrm{T}}^{\gamma}$ vs truth $p_{\mathrm{T}}^{\mathrm{jet}}$
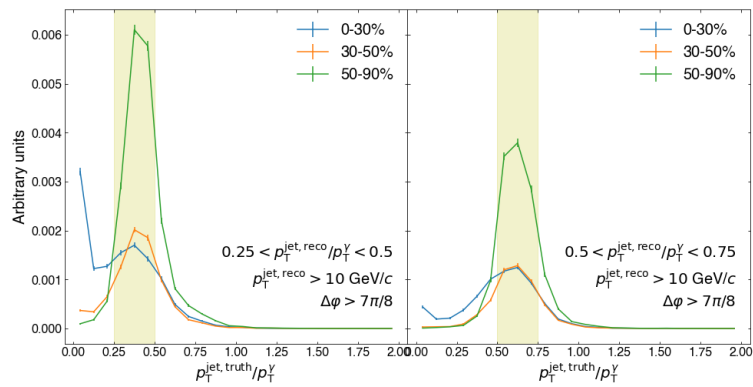
Figure 3.38: 1D projections of the $p_{\mathrm{T}}^{\mathrm{jet}}/p_{\mathrm{T}}^{\gamma} \otimes p_{\mathrm{T}}^{\mathrm{jet}}$ 4D response matrix onto the truth $p_{\mathrm{T}}^{\mathrm{jet}}/p_{\mathrm{T}}^{\gamma}$ axis, for two ranges (0.25–0.5 and 0.5–0.75) of reconstructed $p_{\mathrm{T}}^{\mathrm{jet}}/p_{\mathrm{T}}^{\gamma}$

Chapter 4

Results

The per-trigger yield of jets recoiling from isolated photons as a function of $\Delta\varphi$, also known as the angular correlations, are shown in Figure 4.1, with error bars representing the statistical uncertainty and boxes representing the systematic uncertainty. As we move from left to right, we move from more central collisions to more peripheral collisions. In all but the most central collisions (0-10%), we see a statistically significant back-to-back yield (i.e. $\Delta\varphi$ near π) and not much yield away from this peak. In the 0-10% collisions, the back-to-back yield is consistent with both 0 and with the yield in the other centralities, so we cannot draw strong conclusions from that. We also see some indications of oversubtraction in what look like negative yields, which are unphysical, but this is not uncommon for correlation analyses with large backgrounds. We do not see any trend in the magnitude of the yield as a function of centrality. The systematic uncertainties are partially correlated point-to-point. The purity systematic will shift all the points up and down together, the shower shape background range systematic is uncorrelated point-to-point, and the mixed-event systematic is partially correlated, as both the shape and the magnitude of the mixed-event correlations change with the variations (the magnitude change shifts all the points together, but the shape change does not).
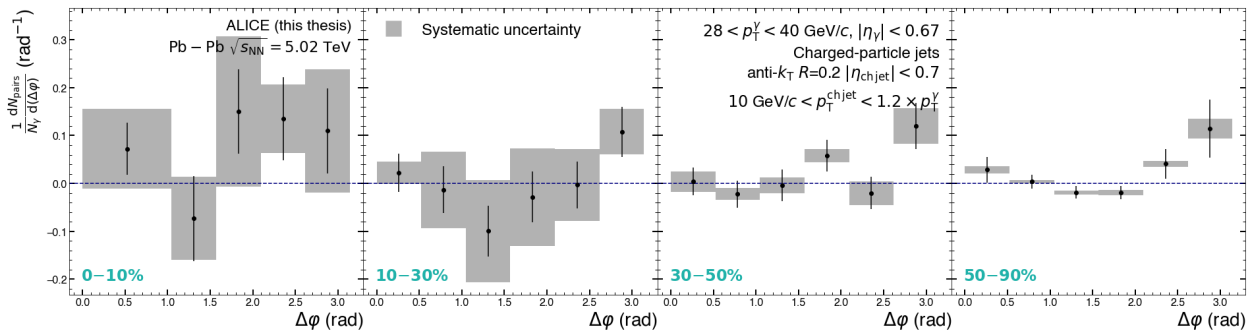
Figure 4.1: Per-trigger yields as a function of $\Delta\varphi$ for different centralities

The photon-jet momentum imbalance (p_T^{jet}/p_T^γ) for back-to-back jets ($\Delta\varphi > 7\pi/8$) is shown in Figure 4.2. As with Figure 4.1, the statistical uncertainty is represented by the error bars, the systematic uncertainty is represented by the boxes, and the panels from left to right go from more central to more peripheral collisions. The 0–0.25 bin is definitionally empty because with our kinematic cuts of $p_T^{jet} > 10$ GeV/c and $p_T^\gamma < 40$ GeV/c, p_T^{jet}/p_T^γ cannot be smaller than 0.25. Since we are considering charged-particle jets with a fairly small R, we would expect that a leading-order photon-jet pair with no energy loss would give $p_T^{jet}/p_T^\gamma \sim 0.6$. Smaller values of p_T^{jet}/p_T^γ are consistent with more jet energy loss. We see a difference in the shape of the distribution as the centrality of the collisions changes in terms of the central values, but given the statistical uncertainties, this difference is not particularly significant. Still, the trend of more peripheral collisions trending toward higher p_T^{jet}/p_T^γ is consistent with the expectation that jets lose more energy in more central collisions. Again, the systematic uncertainties are partially correlated point-to-point.
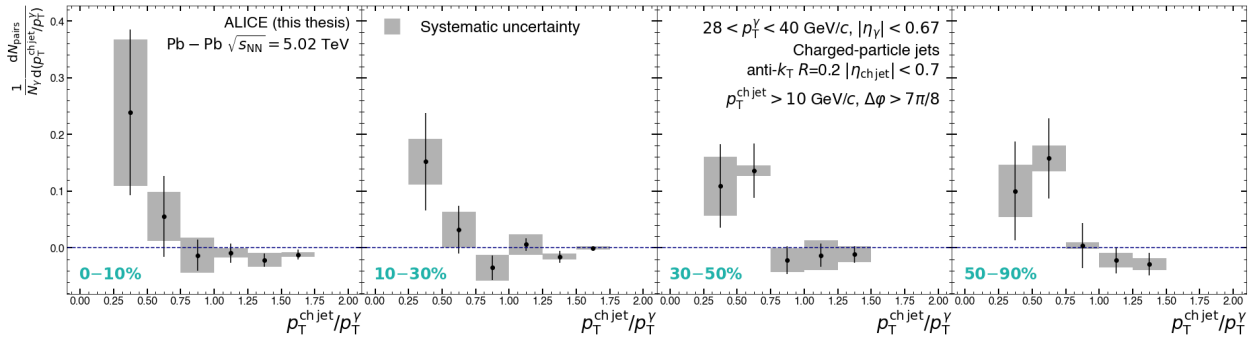
Figure 4.2: Per-trigger yields as a function of p_T^{jet}/p_T^γ for different centralities

In order to quantify the centrality-dependent energy loss, which would be seen as a shift in the shape of the distribution of the momentum imbalance, we calculate the mean of p_T^{jet}/p_T^γ within $0.25 < p_T^{jet}/p_T^\gamma < 1$, which we call the truncated mean $\left\langle p_T^{jet}/p_T^\gamma \right\rangle$. Beyond $p_T^{jet}/p_T^\gamma > 1$, there is very little signal, so we exclude it. The truncated mean $\left\langle p_T^{jet}/p_T^\gamma \right\rangle$ is shown in Figure 4.3 as a function of centrality, where the aforementioned trend in the central values of higher p_T^{jet}/p_T^γ in more peripheral collisions can be more clearly seen, though again, the uncertainties are substantial. The systematic uncertainties are not correlated point-to-point, as their effect is different for different centrality ranges. We might expect the trend to be monotonic and for the value at 0-10% to be lower than the others, rather than appearing to be higher than the value in 10-30%. However, as previously discussed, these measurements are not unfolded, so we should be wary of drawing too many conclusions from these measurements alone. Despite these limitations, in the next chapter, I will discuss how we can learn some physics from this measurement.
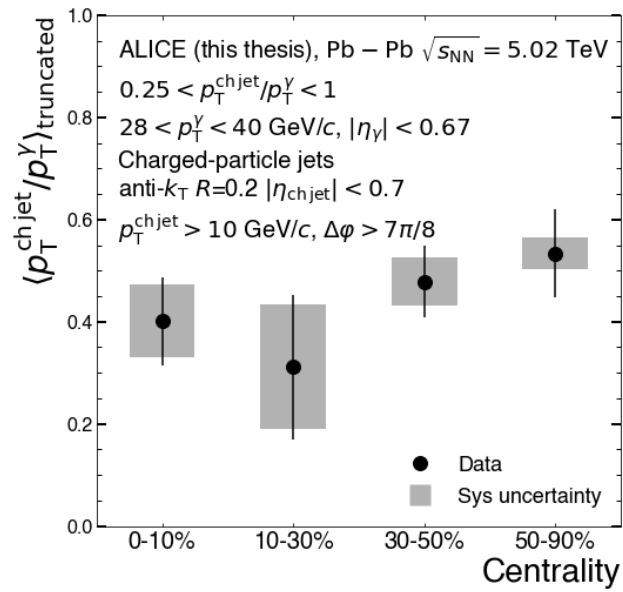
Figure 4.3: Truncated mean of $p_\mathrm{T}^\mathrm{jet}/p_\mathrm{T}^\gamma$ as a function of centrality

Chapter 5

Discussion and conclusions

The experimental results, particularly the $p_\mathrm{T}^\mathrm{jet}/p_\mathrm{T}^\gamma$ and $\left\langle p_\mathrm{T}^\mathrm{jet}/p_\mathrm{T}^\gamma \right\rangle$ distributions, suggest that jets lose more energy in more central collisions, as we expect from previous measurements and calculations of jet quenching [43, 21]. However, without unfolding, it can be difficult to determine how much of this is due to detector effects or to quantify the amount of energy loss. We can draw a number of conclusions from the results by folding theoretical calculations, which applies the response matrices discussed in Section 3.8 to otherwise clean predictions. This applies detector effects such as acceptance and efficiency, as well as residual effects from imperfect underlying event subtraction (such as those due to spatial fluctuations in the underlying event), which drive the jet energy scale and jet energy resolution. It also applies the so-called kinematic efficiency, which accounts for a type of bin migration effect, where we do not measure jets that should have been measured because of our minimum $p_\mathrm{T}^\mathrm{jet}$ cut.

We compare to two folded calculations: PYTHIA, which simulates a pp collision and has no energy loss at all (the same truth distributions are folded for each centrality) and CoLBT Pb–Pb calculations, which, as discussed in the introduction, couples hydrodynamics and LBT and therefore does predict medium modification. We also compare the $p_\mathrm{T}^\mathrm{jet}/p_\mathrm{T}^\gamma$ distributions to a pp calculation from the CoLBT framework; similar to PYTHIA, this CoLBT pp calculation has no medium-induced energy loss. The comparison to folded PYTHIA helps give a sense of how much of the difference between centralities is due to detector effects as well as a comparison to a model with no energy loss, whereas CoLBT is a fairly sophisticated model that does implement medium-induced energy loss among other aspects of the collision, and a comparison to it after folding to include detector effects is expected to be a more accurate description of jet quenching.

For the purposes of comparing to folded CoLBT, we have to combine the 0-10% and 10-30% bins into one 0-30% bin. This is because the calculations were provided in those bins, and new calculations with the separate bins were not yet available. Procedurally, this means recalculating the correlations and uncertainties with 0-30%, rather than combining the final results from the split centrality bins.

5.1 PYTHIA calculation and folding

PYTHIA itself was discussed in Section 3.3. In this case, we simulate events, each with a hard scattering that produces a photon and a jet, the types of events we aim to measure. For the purposes of this comparison, we do not need to then simulate the transport of the particles through the detector with GEANT. Instead, we apply the response matrix to fold the PYTHIA output, in order to see the potentially different effects that a higher-multiplicity event may have on the detector response.

(a) PYTHIA truth distributions

(b) PYTHIA folded distributions
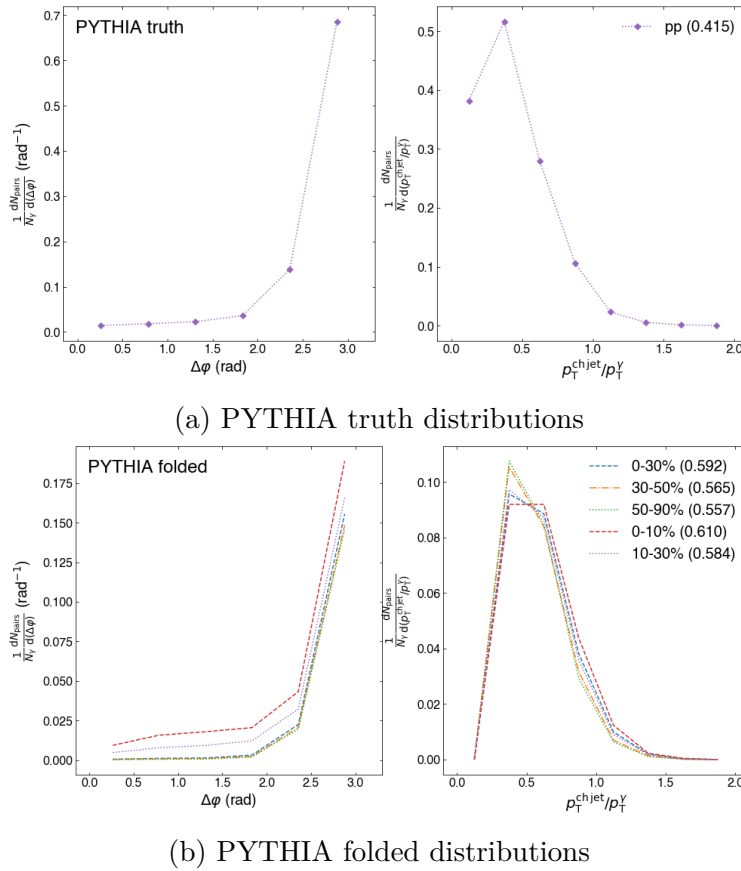
Figure 5.1: PYTHIA truth and folded distributions with $\left\langle p_{\mathrm{T}}^{\mathrm{jet}}/p_{\mathrm{T}}^{\gamma} \right\rangle$ given in parentheses in the legend

Figure 5.1a shows the predictions from PYTHIA without folding, with the $\left\langle p_{\mathrm{T}}^{\mathrm{jet}}/p_{\mathrm{T}}^{\gamma} \right\rangle$ value given in parentheses. We see a clear back-to-back signal in $\Delta\varphi$ and we see that $p_{\mathrm{T}}^{\mathrm{jet}}/p_{\mathrm{T}}^{\gamma}$ has a mean of just over 0.4. At leading order, the original parton should be produced back-to-back with the same p_{T} as the photon. However, higher-order effects, measuring only charged particles, and the relatively small jet radius of $R = 0.2$ will lead to the reconstructed

jet p_T being different from that of the photon. Particles that should be included in the jet fall outside of $R = 0.2$, and charged particles make up, on average, 60% of the particles in a jet [72]. This fraction can fluctuate jet-by-jet, so a measurement of any given charged-particle jet cannot be used to exactly calculate the amount of neutral energy not measured. A larger jet radius would allow us to measure more of the energy of the parton at the expense of more effects from underlying event fluctuations; with $R = 0.2$, we are left with a rather low value of $\left\langle p_T^{\mathrm{jet}}/p_T^\gamma \right\rangle$

Figure 5.1b shows the folded PYTHIA calculations with a different response matrix applied for each centrality, again with $\left\langle p_T^{\mathrm{jet}}/p_T^\gamma \right\rangle$ in parentheses. We see that there are slight differences in the $\Delta\varphi$ shape from detector effects alone (i.e. not from any medium-induced jet energy loss), but they are relatively small, whereas the kinematic efficiency causes the folded per-trigger yield to be significantly lower than that at truth level. This means that a significant number of jets that contribute at truth level fall below our $p_T^{\mathrm{jet}} > 10$ GeV/c cut after folding.

We also see that $\left\langle p_T^{\mathrm{jet}}/p_T^\gamma \right\rangle$ shifts to higher values as a result of the folding, with more of a shift in the more central collisions. In Figure 3.36, we saw that more central collisions cause more smearing into larger values of reconstructed $p_T^{\mathrm{jet}}/p_T^\gamma$, whereas the more peripheral collisions had a similar but smaller smearing. This would explain why the shift in $\left\langle p_T^{\mathrm{jet}}/p_T^\gamma \right\rangle$ is towards higher values, and also why there is more of a shift in the more central collisions. Comparing Figure 5.1b to Figure 5.1a, we see that the detector effects drastically reduce the magnitude of the per-trigger yield, similar to what we saw for $\Delta\varphi$.

5.2 CoLBT calculation and folding

Figure 5.2a shows the predictions from CoLBT without folding, provided by Xin-Nian Wang (one of the creators of CoLBT) and Zhong Yang (a student at Central China Normal University), again with $\left\langle p_T^{\mathrm{jet}}/p_T^\gamma \right\rangle$ in parentheses. We see that the yield decreases with increasing centrality, with about a 14% relative difference in $\left\langle p_T^{\mathrm{jet}}/p_T^\gamma \right\rangle$ between 0-30% and 50-90%. This is due to jet quenching; as jets lose more energy, fewer of them pass the minimum jet p_T cut, resulting in a lower per-trigger yield. We also see that $\left\langle p_T^{\mathrm{jet}}/p_T^\gamma \right\rangle$ decreases with more central collisions, which is also due to more jet quenching in more central collisions, and that there is quenching even in the less central collisions, as $\left\langle p_T^{\mathrm{jet}}/p_T^\gamma \right\rangle$ in the Pb–Pb collisions of all centralities is smaller than in pp. CoLBT has been compared to other AL-ICE measurements, in particular to the amount of modification in the charged hadron p_T spectrum in $\sqrt{s_{\mathrm{NN}}} = 5.02$ TeV Pb–Pb collisions for hadrons with $p_T < 20$ GeV/c, and it agrees reasonably well with the data when also including coalescence [80].

(a) CoLBT truth distributions
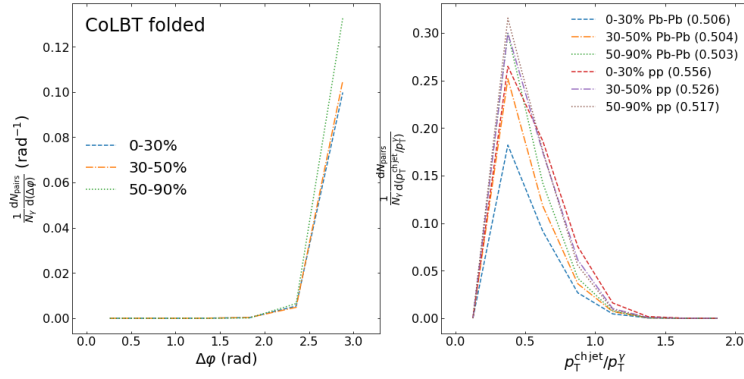
(b) CoLBT folded distributions; note that the right panel $(p_{\mathrm{T}}^{\mathrm{jet}}/p_{\mathrm{T}}^{\gamma})$ is a one-dimensional unfolding and therefore does not have the $p_{\mathrm{T}}^{\mathrm{jet}} > 10$ GeV/c cut
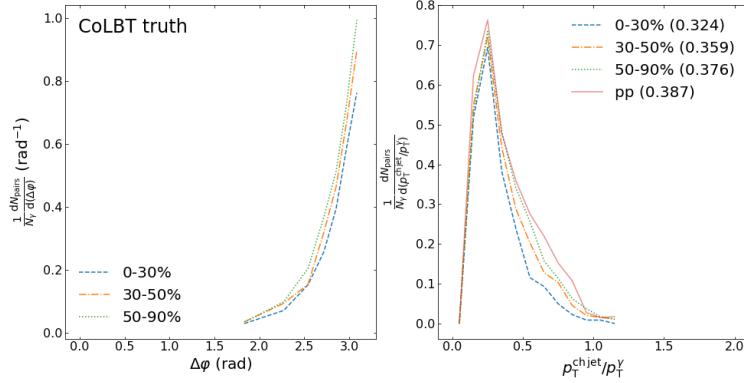
Figure 5.2: CoLBT truth and folded distributions with $\left\langle p_{\mathrm{T}}^{\mathrm{jet}}/p_{\mathrm{T}}^{\gamma} \right\rangle$ given in parentheses in the legend

It is important to note that the CoLBT calculations for the $p_{\mathrm{T}}^{\mathrm{jet}}/p_{\mathrm{T}}^{\gamma}$ distribution were provided in only one large jet p_{T} bin, for charged-particle jets with $5 < p_{\mathrm{T}} < 100$ GeV/c. For the $\Delta\varphi$ distribution, they were provided in three jet p_{T} bins, 5-10, 10-25, and 25-100 GeV/c, allowing us to do a 2-dimensional folding. This then allows us to make a cut on the folded jet p_{T} to match that used in the data, $p_{\mathrm{T}} > 10$ GeV/c. However, with only a 1-dimensional folding for the $p_{\mathrm{T}}^{\mathrm{jet}}/p_{\mathrm{T}}^{\gamma}$ distribution, we cannot make such a cut. Unfortunately, this means that the CoLBT predictions for $p_{\mathrm{T}}^{\mathrm{jet}}/p_{\mathrm{T}}^{\gamma}$ are not directly comparable with the data, but we will show the comparison nonetheless. Because the $\Delta\varphi$ can be folded in two dimensions and a cut can be made on the folded jet p_{T}, the folded CoLBT calculation is more directly comparable to the data.

Figure 5.2b shows the folded CoLBT calculations, again with $\left\langle p_{\mathrm{T}}^{\mathrm{jet}}/p_{\mathrm{T}}^{\gamma} \right\rangle$ in parentheses; as with the PYTHIA, the same pp calculation is folded with a different response matrix

for each centrality range. First, we see that the per-trigger yield drops significantly; this is again due to the kinematic efficiency. Next, we still see that there is less yield in more central collisions. Finally, we see that $\left\langle p_T^{\text{jet}}/p_T^\gamma \right\rangle$ no longer follows a distinct trend with centrality; instead, applying detector effects seems to smear out this trend and $\left\langle p_T^{\text{jet}}/p_T^\gamma \right\rangle$ ends up being about the same for all centralities. This is consistent with the smearing effect we saw when folding PYTHIA, where the $\left\langle p_T^{\text{jet}}/p_T^\gamma \right\rangle$ gets a larger upward shift for more central collisions.

5.3 Comparing data to folded calculations
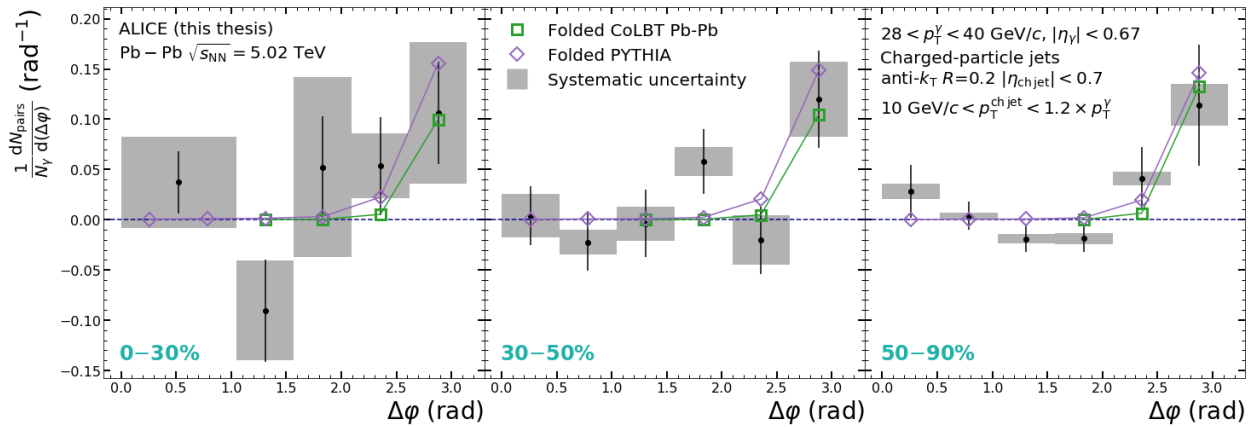
Figure 5.3: Comparison of data with folded theory calculations for $\Delta\varphi$

Figure 5.3 shows the $\Delta\varphi$ distributions in data along with the folded PYTHIA and CoLBT calculations. We see that PYTHIA is systematically higher than the central values in the data in the most back-to-back bin ($5\pi/6 < \Delta\varphi < \pi$), though it agrees with the data within statistical uncertainties. This implies that the per-trigger yield of jets after energy loss is lower than without energy loss, which is to be expected, since jet energy loss would mean that more jets fall below the $p_T^{\text{jet}} > 10$ GeV/c threshold. CoLBT is quite close to the central values in the data and agrees within the statistical uncertainties.

Figure 5.4 shows the $p_T^{\text{jet}}/p_T^\gamma$ distributions in data along with the folded PYTHIA and CoLBT calculations (both Pb–Pb and pp). In general, the first three bins ($0.25 < p_T^{\text{jet}}/p_T^\gamma < 1.0$) contain the vast majority of the signal, so we will focus on those. In all of the centrality bins, PYTHIA does not match the shape in the data. In particular, the PYTHIA has a substantial yield in $0.75 < p_T^{\text{jet}}/p_T^\gamma < 1.0$, whereas the data essentially goes to 0 in those bins. In 0-30%, it underpredicts the data in $0.25 < p_T^{\text{jet}}/p_T^\gamma < 0.5$ and overpredicts the data in $0.5 < p_T^{\text{jet}}/p_T^\gamma < 0.75$ and $0.75 < p_T^{\text{jet}}/p_T^\gamma < 1.0$. In the more peripheral bins, it matches the $0.25 < p_T^{\text{jet}}/p_T^\gamma < 0.5$ bin pretty well and is consistent within uncertainties in
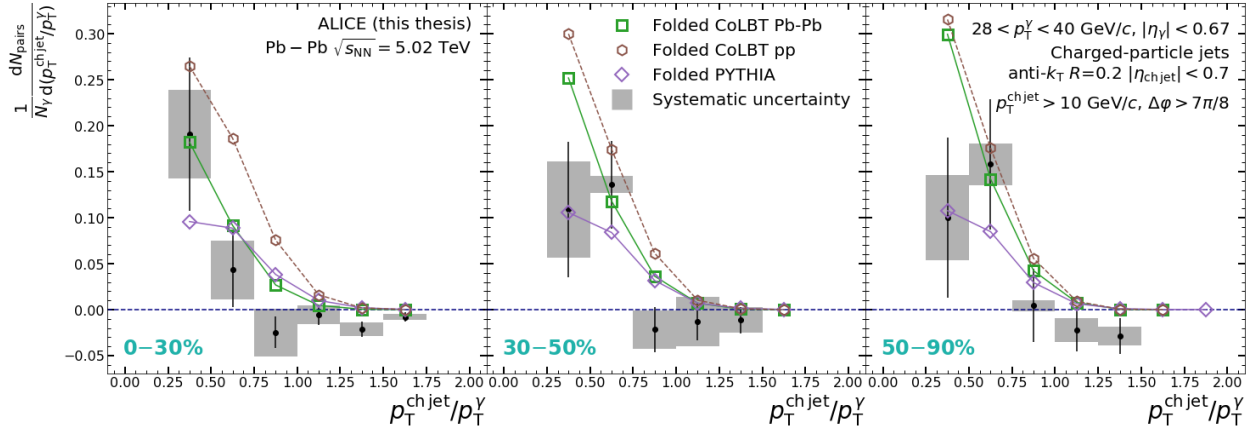
Figure 5.4: Comparison of data with folded theory calculations for $p_{\mathrm{T}}^{\mathrm{jet}}/p_{\mathrm{T}}^{\gamma}$

$0.5 < p_{\mathrm{T}}^{\mathrm{jet}}/p_{\mathrm{T}}^{\gamma} < 0.75$. Overall, we can say that the PYTHIA shape is shifted towards higher $p_{\mathrm{T}}^{\mathrm{jet}}/p_{\mathrm{T}}^{\gamma}$ relative to the data.

The CoLBT pp calculation overpredicts the data by quite a bit in almost every bin. For the Pb–Pb calculation, CoLBT is relatively consistent with the data in 0-30%, though as with the PYTHIA, it has a substantial yield in $0.75 < p_{\mathrm{T}}^{\mathrm{jet}}/p_{\mathrm{T}}^{\gamma} < 1.0$ where the data goes to zero. In 30-50% and 50-90%, CoLBT has a much higher yield in $0.25 < p_{\mathrm{T}}^{\mathrm{jet}}/p_{\mathrm{T}}^{\gamma} < 0.5$ than the data, but the same is true for the $0.75 < p_{\mathrm{T}}^{\mathrm{jet}}/p_{\mathrm{T}}^{\gamma} < 1.0$ bin. So the shape of the distributions do not match between the folded CoLBT and data, since the CoLBT falls monotonically with $p_{\mathrm{T}}^{\mathrm{jet}}/p_{\mathrm{T}}^{\gamma}$ in all centralities, whereas the data has more of a peak in the more peripheral collisions. However, as previously noted, the CoLBT underwent only a one-dimensional unfolding and so there is no cut on the folded jet p_{T}.

Figure 5.5 shows $\left\langle p_{\mathrm{T}}^{\mathrm{jet}}/p_{\mathrm{T}}^{\gamma} \right\rangle$ as a function of centrality along with a comparison to the folded calculations. In the 0-30% bin, all of the calculations have a higher $\left\langle p_{\mathrm{T}}^{\mathrm{jet}}/p_{\mathrm{T}}^{\gamma} \right\rangle$ than the central value in the data, though the folded CoLBT Pb–Pb calculation is the closest to the data. In the other centralities, all of the calculations agree with the data within the statistical uncertainties. Since the folded CoLBT Pb–Pb calculations still overpredict the data in 0-30% while agreeing in the other centralities, this hints that CoLBT predicts less energy loss than we observe in the data in the most central collisions.

Since the folding in both PYTHIA and CoLBT pp caused the $\left\langle p_{\mathrm{T}}^{\mathrm{jet}}/p_{\mathrm{T}}^{\gamma} \right\rangle$ to get shifted upwards, with a larger shift for more central collisions, we might expect that if we were able to unfold our measurement, we might see that the $\left\langle p_{\mathrm{T}}^{\mathrm{jet}}/p_{\mathrm{T}}^{\gamma} \right\rangle$ for 0-30% collisions could become significantly lower than the more peripheral collisions. Even without unfolding, there are already indications that $\left\langle p_{\mathrm{T}}^{\mathrm{jet}}/p_{\mathrm{T}}^{\gamma} \right\rangle$ is lower in 0-30% than in pp, if we compare with folded PYTHIA as a proxy for a pp measurement, whereas the less central collisions

are more consistent with the folded PYTHIA.
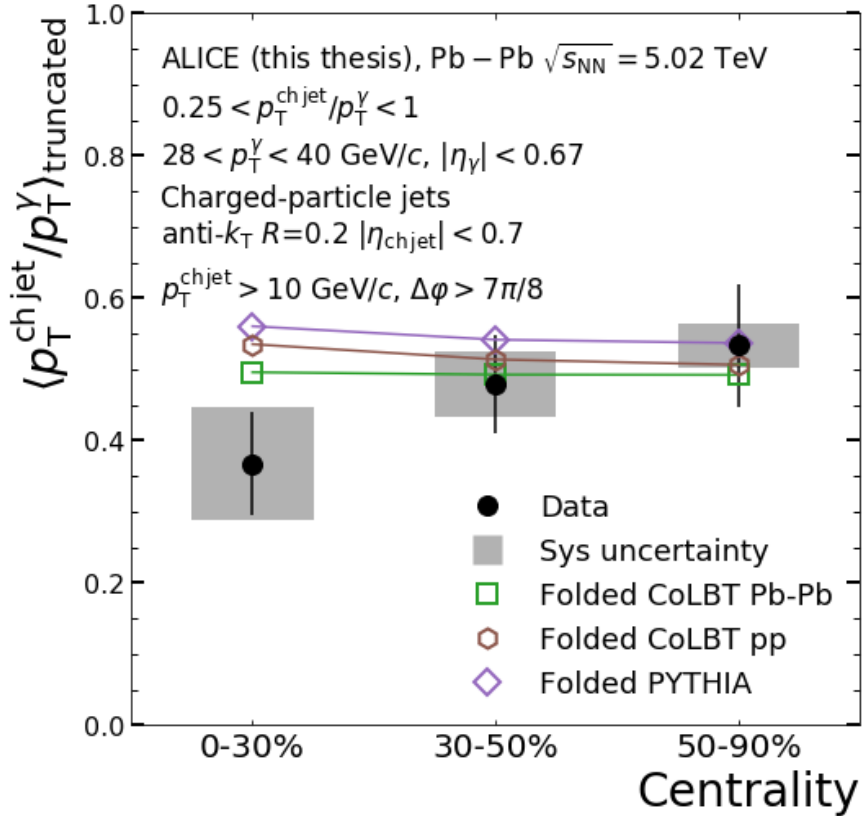
Figure 5.5: Comparison of data with folded theory calculations for $\left\langle p_{\mathrm{T}}^{\mathrm{jet}}/p_{\mathrm{T}}^{\gamma} \right\rangle$

We can further compare data to folded PYTHIA for 0-10% and 10-30%. This is shown in Figures 5.6 and 5.7. The $\Delta\varphi$ distributions tell much the same story as we saw in Figure 5.3, so we will not discuss it again here. The $p_{\mathrm{T}}^{\mathrm{jet}}/p_{\mathrm{T}}^{\gamma}$ also tells a similar story as the combined 0-30%, with an excess in $0.75 < p_{\mathrm{T}}^{\mathrm{jet}}/p_{\mathrm{T}}^{\gamma} < 1$ in folded PYTHIA relative to the data, perhaps a slight overprediction in $0.5 < p_{\mathrm{T}}^{\mathrm{jet}}/p_{\mathrm{T}}^{\gamma} < 0.75$, and perhaps a slight underprediction in $0.25 < p_{\mathrm{T}}^{\mathrm{jet}}/p_{\mathrm{T}}^{\gamma} < 0.5$. Again, this will lead to a higher $\left\langle p_{\mathrm{T}}^{\mathrm{jet}}/p_{\mathrm{T}}^{\gamma} \right\rangle$ in folded PYTHIA relative to data.

5.4 Comparing to other published measurements

We can also compare our results with both the CMS [40] and ATLAS [36] measurements. They are not directly comparable for a number of reasons, but we can see if they are conceptually consistent with each other. The major ways in which each of the analyses differ in
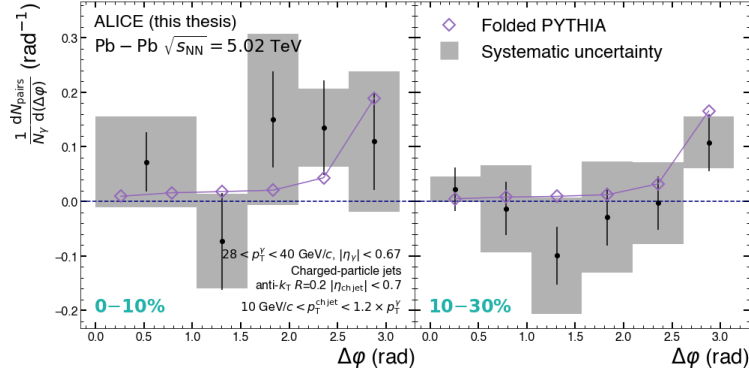
Figure 5.6: Comparison of $\Delta\varphi$ distributions in data with folded PYTHIA for centralities 0-10% and 10-30%
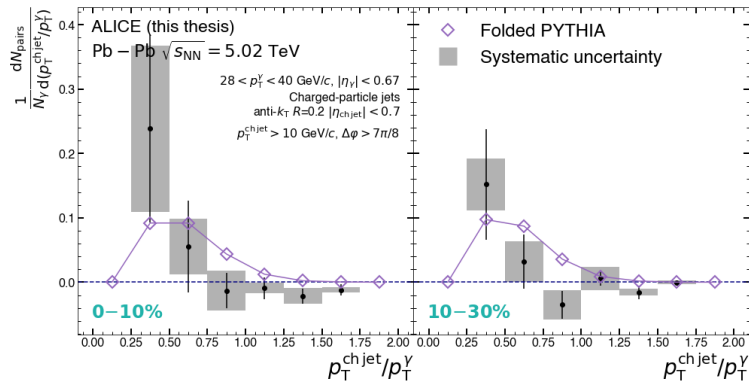
Figure 5.7: Comparison of $p_{\mathrm{T}}^{\mathrm{jet}}/p_{\mathrm{T}}^{\gamma}$ distributions in data with folded PYTHIA for centralities 0-10% and 10-30%

terms of what is plotted in Figure 5.8 is summarized in Table 5.1. All three use different jet R, only ALICE uses charged-particle jets and isolation, only ATLAS is unfolded, and while the photon and jet p_{T} thresholds are similar for CMS and ATLAS, they are much lower in our ALICE measurement.

Despite the differences between the analyses, we plot all three measurements of $\left\langle p_{\mathrm{T}}^{\mathrm{jet}}/p_{\mathrm{T}}^{\gamma}\right\rangle$ together in Figure 5.8. The x axis is $\langle N_{\mathrm{part}}\rangle$, the average number of nucleons that participate in a collision within a given centrality class, which is calculated using a Glauber model; larger values correspond to more central collisions. Because ALICE measures only the charged component of jets, we expect it to be about 60% the value of what it would be for full jets, which is approximately what we see. In the most peripheral (leftmost) bin, all three Pb–Pb measurements are consistent with their pp reference within uncertainties. In the most central (rightmost) bin, 0-10%, we see that ATLAS and CMS see a decrease in the Pb–Pb relative to

Table 5.1: Comparison of analysis parameters for isolated photon-jet correlations in Pb–Pb collisions at $\sqrt{s_{\mathrm{NN}}} = 5.02$ TeV for ALICE (this thesis), ATLAS, and CMS

Parameter	ALICE	ATLAS	CMS
Charged or full	Charged	Full	Full
Jet algorithm	anti-k_{T}	anti-k_{T}	anti-k_{T}
Jet R	0.2	0.4	0.3
Jet p_{T}	$p_{\mathrm{T}} > 10$ GeV/c	$p_{\mathrm{T}} > 31.6$ GeV/c	$p_{\mathrm{T}} > 30$ GeV/c
Jet acceptance	$|\eta| < 0.7$	$|\eta| < 2.8$	$|\eta| < 1.6$
Photon p_{T}	$28 < p_{\mathrm{T}} < 40$ GeV/c	$63.1 < p_{\mathrm{T}} < 79.1$ GeV/c	$p_{\mathrm{T}} > 60$ GeV/c
Photon acceptance	$|\eta| < 0.67$	$|\eta| < 2.37$	$|\eta| < 1.44$
Photon isolation	1.5 GeV/c, $R = 0.2$	8 GeV/c, $R = 0.3$	1 GeV/c, $R = 0.4$
Unfolded?	No	Yes	No

the pp baseline of 0.07 and 0.12 respectively for photons with $p_{\mathrm{T}} > 60$ GeV/c and jets with $p_{\mathrm{T}} > 30$ GeV/c (note that only ATLAS is unfolded). In our ALICE measurement, we see a decrease of about 0.17 relative to our pp (PYTHIA) baseline, albeit with a larger statistical uncertainty. In the next centrality bin over, which for our measurement corresponds to 10-30%, we see a decrease of about 0.24, again with a substantial statistical uncertainty. The equivalent CMS measurement sees a decrease of about 0.12 and the closest ATLAS centrality bin sees a decrease of 0.05. Our measurement therefore indicates that there is more energy loss for lower-p_{T} photons and jets, but between the uncertainties and the fact that the measurement is not unfolded, we cannot strongly draw this conclusion. However, this is consistent with lower-p_{T} partons losing a larger fraction of their energy in the QGP, at least in more central collisions.

5.5 Conclusions

We measured the isolated photon-jet correlations in 5.02 TeV Pb–Pb collisions with ALICE for photons with $28 < p_{\mathrm{T}} < 40$ GeV/c and jets with $p_{\mathrm{T}} > 10$ GeV/c in 4 centrality bins: 0-10%, 10-30%, 30-50%, and 50-90%. We see indications of centrality-dependent energy loss through the change in shape of the $p_{\mathrm{T}}^{\mathrm{jet}}/p_{\mathrm{T}}^{\gamma}$ distribution and the change in value of $\left\langle p_{\mathrm{T}}^{\mathrm{jet}}/p_{\mathrm{T}}^{\gamma} \right\rangle$ with centrality, as well as through a lower per-trigger yield in Pb–Pb relative to our folded PYTHIA reference. Within uncertainties, we do not see centrality dependence in the $\Delta\varphi$ distributions. This is similar to what CMS and ATLAS saw in their γ-jet measurements.

In the folded PYTHIA and CoLBT pp baseline, we see that $\left\langle p_{\mathrm{T}}^{\mathrm{jet}}/p_{\mathrm{T}}^{\gamma} \right\rangle$ actually increases in the more central collisions. This is opposite the direction in the data, which decreases for more central collisions, which indicates that seeing lower $\left\langle p_{\mathrm{T}}^{\mathrm{jet}}/p_{\mathrm{T}}^{\gamma} \right\rangle$ in more central collisions is actually due to energy loss, not detector effects. Without unfolding, we cannot be
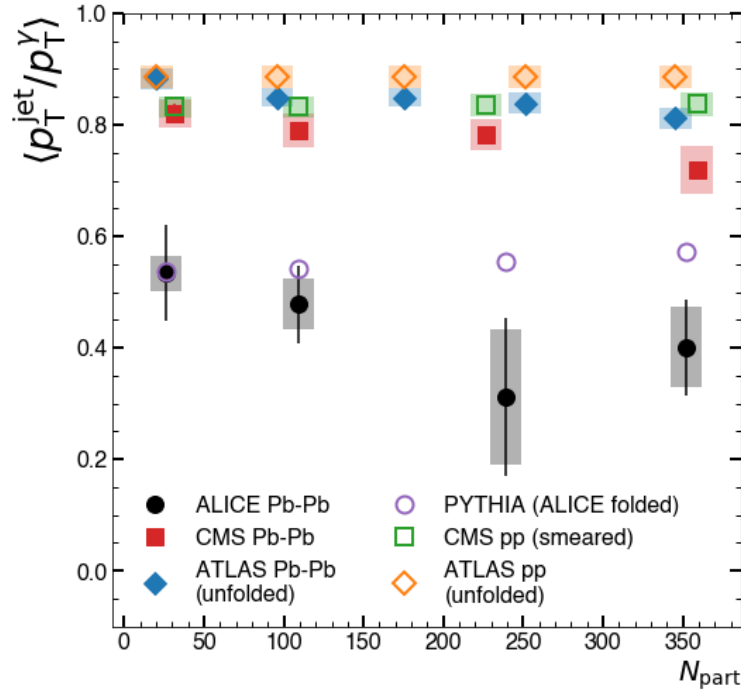
Figure 5.8: Comparison of ALICE data with measurements in Pb–Pb collisions at $\sqrt{s_{\mathrm{NN}}} = 5.02$ TeV from CMS and ATLAS. See Table 5.1 for all the ways in which the analyses differ

quantitatively precise about the amount of energy loss. However, by comparing our measurement of $\left\langle p_{\mathrm{T}}^{\mathrm{jet}}/p_{\mathrm{T}}^{\gamma} \right\rangle$ to those from CMS and ATLAS, we see hints of more energy loss for our lower-p_{T} jets in the most central collisions, keeping in mind that our measurement is not unfolded. Our measurement suggests that partons that start with smaller p_{T} lose a larger fraction of their energy when traversing the QGP.

In comparing to folded CoLBT Pb–Pb calculations (which implement medium-induced energy loss) and to folded PYTHIA and CoLBT pp calculations (which are both pp simulations with no medium-induced energy loss), we find that no calculation exactly matches the data in all points across all centralities. In particular, the folded PYTHIA has a higher back-to-back per-trigger yield and a shift in $p_{\mathrm{T}}^{\mathrm{jet}}/p_{\mathrm{T}}^{\gamma}$ towards higher values, which is to be expected as the PYTHIA has no medium-induced energy loss. The folded CoLBT Pb–Pb matches the back-to-back per-trigger yield in the data but has a fairly different shape of the $p_{\mathrm{T}}^{\mathrm{jet}}/p_{\mathrm{T}}^{\gamma}$ distribution, even if the $\left\langle p_{\mathrm{T}}^{\mathrm{jet}}/p_{\mathrm{T}}^{\gamma} \right\rangle$ is similar in the more peripheral collisions. However, in 0-30%, the folded CoLBT has a higher $\left\langle p_{\mathrm{T}}^{\mathrm{jet}}/p_{\mathrm{T}}^{\gamma} \right\rangle$ than in the data. This indicates that CoLBT predicts less energy loss than we see in the data in the most central collisions. We might also like to compare our results to other calculations with jet quenching discussed in the introduction and to compare to the ALICE measurement of inclusive jet R_{AA}.

As it stands, this measurement is limited by the amount of data ALICE was able to gather in Run 2. In Run 3, which has just begun, we expect to acquire more data and therefore be able improve the precision of this result. We may be able to be more quantitative about the amount of jet energy loss induced by the medium. It might be possible to do jet substructure measurements with these photon-triggered jets. There is also pp and p–Pb data available, both at essentially the same center-of-mass energy (5 TeV), so it would be interesting to compare this result to those as well. Photon-triggered jets are quark-enriched, which means that they can be compared to inclusive jets or heavy-flavor jets, allowing us to potentially explore differences in medium-induced energy loss for light quarks, heavy quarks and gluons.

Bibliography

[1] *ALICE Data Preparation Group.* URL: https://alice-offline.web.cern.ch/Activities/alice-data-preparation-group.

[2] *AliPhysics: EMCal embedding framework.* May 2017. URL: http://alidoc.cern.ch/AliPhysics/v5-09-07-01/_r_e_a_d_m_eemc_embedding.html.

[3] J Allen et al. *ALICE DCal: An Addendum to the EMCal Technical Design Report Di-Jet and Hadron-Jet correlation measurements in ALICE.* Tech. rep. 2010. URL: https://cds.cern.ch/record/1272952.

[4] B. Andersson et al. "Parton fragmentation and string dynamics". In: *Physics Reports* 97.2 (1983), pp. 31–145. ISSN: 0370-1573. DOI: https://doi.org/10.1016/0370-1573(83)90080-7. URL: https://www.sciencedirect.com/science/article/pii/0370157383900807.

[5] David A. Appell. "Jets as a probe of quark-gluon plasmas". In: *Phys. Rev. D* 33 (3 Feb. 1986), pp. 717–722. DOI: 10.1103/PhysRevD.33.717. URL: https://link.aps.org/doi/10.1103/PhysRevD.33.717.

[6] P. Aurenche et al. "Next to leading order bremsstrahlung contribution to prompt-photon production". In: *Nuclear Physics B* 399.1 (1993), pp. 34–62. ISSN: 0550-3213. DOI: https://doi.org/10.1016/0550-3213(93)90615-V. URL: https://www.sciencedirect.com/science/article/pii/055032139390615V.

[7] R. Baier et al. "Radiative energy loss of high energy quarks and gluons in a finite-volume quark-gluon plasma". In: *Nuclear Physics B* 483.1 (1997), pp. 291–320. ISSN: 0550-3213. DOI: https://doi.org/10.1016/S0550-3213(96)00553-6. URL: https://www.sciencedirect.com/science/article/pii/S0550321396005536.

[8] P. Berta et al. "Pileup and underlying event mitigation with iterative constituent subtraction". In: *Journal of High Energy Physics* 2019.8 (Aug. 2019). DOI: 10.1007/jhep08(2019)175. URL: https://doi.org/10.1007/jhep08(2019)175.

[9] Peter Berta et al. "Particle-level pileup subtraction for jets and jet shapes". In: *Journal of High Energy Physics* 2014.6 (June 2014). DOI: 10.1007/jhep06(2014)092. URL: https://doi.org/10.1007/jhep06(2014)092.

[10] Philip R. Bevington et al. "Data Reduction and Error Analysis for the Physical Sciences". In: *Computers in Physics* 7.4 (1993). DOI: 10.1063/1.4823194.

[11] J. P. Blaizot and Larry D. McLerran. "Jets in expanding quark-gluon plasmas". In: *Phys. Rev. D* 34 (9 Nov. 1986), pp. 2739–2745. DOI: `10.1103/PhysRevD.34.2739`. URL: `https://link.aps.org/doi/10.1103/PhysRevD.34.2739`.

[12] D. Blau. "Performance of the ALICE electromagnetic calorimeters in LHC Runs 1 and 2 and upgrade projects". In: *Journal of Instrumentation* 15.03 (Mar. 2020), pp. C03025–C03025. DOI: `10.1088/1748-0221/15/03/c03025`. URL: `https://doi.org/10.1088/1748-0221/15/03/c03025`.

[13] Lydia Brenner et al. "Comparison of unfolding methods using RooFitUnfold". In: *International Journal of Modern Physics A* 35.24 (2020), p. 2050145. DOI: `10.1142/S0217751X20501456`. eprint: `https://doi.org/10.1142/S0217751X20501456`. URL: `https://doi.org/10.1142/S0217751X20501456`.

[14] R. Brun et al. "GEANT3". In: *CERN-DD-EE-84-1* (Sept. 1987).

[15] Wit Busza, Krishna Rajagopal, and Wilke van der Schee. "Heavy Ion Collisions: The Big Picture and the Big Questions". In: *Annual Review of Nuclear and Particle Science* 68.1 (2018), pp. 339–376. DOI: `10.1146/annurev-nucl-101917-020852`. eprint: `https://doi.org/10.1146/annurev-nucl-101917-020852`. URL: `https://doi.org/10.1146/annurev-nucl-101917-020852`.

[16] Matteo Cacciari, Gavin P Salam, and Gregory Soyez. "The anti-k_t jet clustering algorithm". In: *Journal of High Energy Physics* 2008.04 (Apr. 2008), pp. 063–063. DOI: `10.1088/1126-6708/2008/04/063`. URL: `https://doi.org/10.1088/1126-6708/2008/04/063`.

[17] Matteo Cacciari and Gavin P. Salam. "Pileup subtraction using jet areas". In: *Phys. Lett. B* 659 (2008), pp. 119–126. DOI: `10.1016/j.physletb.2007.09.077`. arXiv: `0707.1378 [hep-ph]`.

[18] Matteo Cacciari, Gavin P. Salam, and Gregory Soyez. "FastJet user manual". In: *The European Physical Journal C* 72.3 (Mar. 2012). ISSN: 1434-6052. DOI: `10.1140/epjc/s10052-012-1896-2`. URL: `http://dx.doi.org/10.1140/epjc/s10052-012-1896-2`.

[19] Matteo Cacciari, Gavin P. Salam, and Gregory Soyez. "The Catchment Area of Jets". In: *JHEP* 04 (2008), p. 005. DOI: `10.1088/1126-6708/2008/04/005`. arXiv: `0802.1188 [hep-ph]`.

[20] Shanshan Cao and Abhijit Majumder. "Nuclear modification of leading hadrons and jets within a virtuality ordered parton shower". In: *Physical Review C* 101.2 (Feb. 2020). DOI: `10.1103/physrevc.101.024903`. URL: `https://doi.org/10.1103/physrevc.101.024903`.

[21] Shanshan Cao and Xin-Nian Wang. "Jet quenching and medium response in high-energy heavy-ion collisions: a review". In: *Reports on Progress in Physics* 84.2 (Jan. 2021), p. 024301. DOI: `10.1088/1361-6633/abc22b`. URL: `https://doi.org/10.1088/1361-6633/abc22b`.

[22] Shanshan Cao et al. "Linearized Boltzmann transport model for jet propagation in the quark-gluon plasma: Heavy quark evolution". In: *Physical Review C* 94.1 (July 2016). DOI: 10.1103/physrevc.94.014909. URL: https://doi.org/10.1103/physrevc.94.014909.

[23] Stefano Carrazza, Stefano Forte, and Juan Rojo. *Parton Distributions and Event Generators*. 2013. DOI: 10.48550/ARXIV.1311.5887. URL: https://arxiv.org/abs/1311.5887.

[24] A. K. Chaudhuri and Ulrich Heinz. "Effects of Jet Quenching on the Hydrodynamical Evolution of Quark-Gluon Plasma". In: *Physical Review Letters* 97.6 (Aug. 2006). DOI: 10.1103/physrevlett.97.062301. URL: https://doi.org/10.1103/physrevlett.97.062301.

[25] Wei Chen et al. "Effects of jet-induced medium excitation in γ-hadron correlation in A+A collisions". In: *Physics Letters B* 777 (Feb. 2018), pp. 86–90. DOI: 10.1016/j.physletb.2017.12.015. URL: https://doi.org/10.1016/j.physletb.2017.12.015.

[26] ALICE Collaboration. "Centrality Dependence of the Charged-Particle Multiplicity Density at Midrapidity in Pb-Pb Collisions at $\sqrt{s_{\mathrm{NN}}} = 2.76$ TeV". In: *Phys. Rev. Lett.* 106 (3 Jan. 2011), p. 032301. DOI: 10.1103/PhysRevLett.106.032301. URL: https://link.aps.org/doi/10.1103/PhysRevLett.106.032301.

[27] ALICE Collaboration. "Measurement of isolated photon-hadron correlations in $\sqrt{s_{\mathrm{NN}}} = 5.02$ TeV *pp* and *p*-Pb collisions". In: *Phys. Rev. C* 102 (4 Oct. 2020), p. 044908. DOI: 10.1103/PhysRevC.102.044908. URL: https://link.aps.org/doi/10.1103/PhysRevC.102.044908.

[28] ALICE Collaboration. "Measurement of jet suppression in central Pb-Pb collisions at $\sqrt{s_{\mathrm{NN}}} = 2.76$ TeV". In: *Physics Letters B* 746 (June 2015), pp. 1–14. DOI: 10.1016/j.physletb.2015.04.039. URL: https://doi.org/10.1016/j.physletb.2015.04.039.

[29] ALICE Collaboration. "Measurement of the inclusive isolated photon production cross section in pp collisions at $\sqrt{s} = 7$ TeV". In: *The European Physical Journal C* 79.11 (Nov. 2019). DOI: 10.1140/epjc/s10052-019-7389-9. URL: https://doi.org/10.1140/epjc/s10052-019-7389-9.

[30] ALICE Collaboration. *Performance of the ALICE Electromagnetic Calorimeter*. 2022. DOI: 10.48550/ARXIV.2209.04216. URL: https://arxiv.org/abs/2209.04216.

[31] ALICE Collaboration. "Performance of the ALICE experiment at the CERN LHC". In: *International Journal of Modern Physics A* 29.24 (2014), p. 1430044. DOI: 10.1142/S0217751X14300440. eprint: https://doi.org/10.1142/S0217751X14300440. URL: https://doi.org/10.1142/S0217751X14300440.

[32] ALICE Collaboration. "The ALICE experiment at the CERN LHC". In: *Journal of Instrumentation* 3.08 (Aug. 2008), S08002–S08002. DOI: 10.1088/1748-0221/3/08/s08002. URL: https://doi.org/10.1088/1748-0221/3/08/s08002.

[33] ALICE Collaboration. "Transverse momentum spectra and nuclear modification factors of charged particles in pp, p-Pb and Pb-Pb collisions at the LHC". In: *Journal of High Energy Physics* 2018.11 (Nov. 2018). ISSN: 1029-8479. DOI: 10.1007/jhep11(2018)013. URL: http://dx.doi.org/10.1007/JHEP11(2018)013.

[34] ALICE Collaboration. "Transverse momentum spectra and nuclear modification factors of charged particles in pp, p-Pb and Pb-Pb collisions at the LHC". In: *Journal of High Energy Physics* 2018.11 (Nov. 2018). DOI: 10.1007/jhep11(2018)013. URL: https://doi.org/10.1007/jhep11(2018)013.

[35] ATLAS Collaboration. "Comparison of Fragmentation Functions for Jets Dominated by Light Quarks and Gluons from *pp* and Pb + Pb Collisions in ATLAS". In: *Phys. Rev. Lett.* 123 (4 July 2019), p. 042001. DOI: 10.1103/PhysRevLett.123.042001. URL: https://link.aps.org/doi/10.1103/PhysRevLett.123.042001.

[36] ATLAS Collaboration. "Measurement of photon–jet transverse momentum correlations in 5.02 TeV Pb + Pb and pp collisions with ATLAS". In: *Physics Letters B* 789 (2019), pp. 167–190. ISSN: 0370-2693. DOI: https://doi.org/10.1016/j.physletb.2018.12.023. URL: https://www.sciencedirect.com/science/article/pii/S037026931830950X.

[37] ATLAS Collaboration. "The ATLAS Experiment at the CERN Large Hadron Collider". In: *Journal of Instrumentation* 3.08 (Aug. 2008), S08003–S08003. DOI: 10.1088/1748-0221/3/08/s08003. URL: https://doi.org/10.1088/1748-0221/3/08/s08003.

[38] CMS Collaboration. "Jet Shapes of Isolated Photon-Tagged Jets in Pb-Pb and *pp* Collisions at $\sqrt{s_{NN}} = 5.02$ TeV". In: *Phys. Rev. Lett.* 122 (15 Apr. 2019), p. 152001. DOI: 10.1103/PhysRevLett.122.152001. URL: https://link.aps.org/doi/10.1103/PhysRevLett.122.152001.

[39] CMS Collaboration. "Observation of Medium-Induced Modifications of Jet Fragmentation in Pb-Pb Collisions at $\sqrt{s_{\mathrm{NN}}} = 5.02$ TeV Using Isolated Photon-Tagged Jets". In: *Phys. Rev. Lett.* 121 (24 Dec. 2018), p. 242301. DOI: 10.1103/PhysRevLett.121.242301. URL: https://link.aps.org/doi/10.1103/PhysRevLett.121.242301.

[40] CMS Collaboration. "Study of jet quenching with isolated-photon+jet correlations in PbPb and pp collisions at sNN=5.02 TeV". In: *Physics Letters B* 785 (2018), pp. 14–39. ISSN: 0370-2693. DOI: https://doi.org/10.1016/j.physletb.2018.07.061. URL: https://www.sciencedirect.com/science/article/pii/S0370269318306245.

[41] CMS Collaboration. "The CMS experiment at the CERN LHC". In: *Journal of Instrumentation* 3.08 (Aug. 2008), S08004–S08004. DOI: 10.1088/1748-0221/3/08/s08004. URL: https://doi.org/10.1088/1748-0221/3/08/s08004.

[42] LHCb Collaboration. "The LHCb Detector at the LHC". In: *Journal of Instrumentation* 3.08 (Aug. 2008), S08005–S08005. DOI: 10.1088/1748-0221/3/08/s08005. URL: https://doi.org/10.1088/1748-0221/3/08/s08005.

[43] PHENIX Collaboration. "Formation of dense partonic matter in relativistic nucleus–nucleus collisions at RHIC: Experimental evaluation by the PHENIX Collaboration". In: *Nuclear Physics A* 757.1-2 (Aug. 2005), pp. 184–283. DOI: 10.1016/j.nuclphysa.2005.03.086. URL: https://doi.org/10.1016/j.nuclphysa.2005.03.086.

[44] PHENIX collaboration. "Centrality dependence of $\pi^{\pm}$, $K^{\pm}$, p and $\bar{p}$ production from $\sqrt{s_{\mathrm{NN}}} = 130$ GeV Au + Au collisions at RHIC". In: 88.24 (May 2002). DOI: 10.1103/physrevlett.88.242301. URL: https://doi.org/10.1103/physrevlett.88.242301.

[45] Francesco D'Eramo et al. "Momentum broadening in weakly coupled quark-gluon plasma (with a view to finding the quasiparticles within liquid quark-gluon plasma)". In: *Journal of High Energy Physics* 2013.5 (May 2013). DOI: 10.1007/jhep05(2013)031. URL: https://doi.org/10.1007/jhep05(2013)031.

[46] G Dellacasa et al. *ALICE time projection chamber: Technical Design Report.* Technical design report. ALICE. Geneva: CERN, 2000. URL: http://cds.cern.ch/record/451098.

[47] Eric Drexler. *Elementary particle interactions in the Standard Model.* Distributed under a CC0 1.0 license. 2014. URL: https://commons.wikimedia.org/wiki/File:Elementary_particle_interactions_in_the_Standard_Model.png.

[48] Joshua P. Ellis. "TikZ-Feynman: Feynman diagrams with TikZ". In: *Computer Physics Communications* 210 (2017), pp. 103–123. ISSN: 0010-4655. DOI: https://doi.org/10.1016/j.cpc.2016.08.019. URL: https://www.sciencedirect.com/science/article/pii/S0010465516302521.

[49] Jacob J. Ethier and Emanuele R. Nocera. "Parton Distributions in Nucleons and Nuclei". In: *Annual Review of Nuclear and Particle Science* 70.1 (2020), pp. 43–76. DOI: 10.1146/annurev-nucl-011720-042725. eprint: https://doi.org/10.1146/annurev-nucl-011720-042725. URL: https://doi.org/10.1146/annurev-nucl-011720-042725.

[50] Tom Fawcett. "An introduction to ROC analysis". In: *Pattern Recognition Letters* 27.8 (2006). ROC Analysis in Pattern Recognition, pp. 861–874. ISSN: 0167-8655. DOI: https://doi.org/10.1016/j.patrec.2005.10.010. URL: https://www.sciencedirect.com/science/article/pii/S016786550500303X.

[51] R. Frühwirth. "Application of Kalman filtering to track and vertex fitting". In: *Nuclear Instruments and Methods in Physics Research Section A: Accelerators, Spectrometers, Detectors and Associated Equipment* 262.2 (1987), pp. 444–450. ISSN: 0168-9002. DOI: https://doi.org/10.1016/0168-9002(87)90887-4. URL: https://www.sciencedirect.com/science/article/pii/0168900287908874.

[52] M. Göckeler et al. "Determination of the Lambda parameter from full lattice QCD". In: *Phys. Rev. D* 73 (1 Jan. 2006), p. 014513. DOI: `10.1103/PhysRevD.73.014513`. URL: `https://link.aps.org/doi/10.1103/PhysRevD.73.014513`.

[53] FRANK E. HARRELL and C. E. DAVIS. "A new distribution-free quantile estimator". In: *Biometrika* 69.3 (Dec. 1982), pp. 635–640. ISSN: 0006-3444. DOI: `10.1093/biomet/69.3.635`. eprint: `https://academic.oup.com/biomet/article-pdf/69/3/635/590991/69-3-635.pdf`. URL: `https://doi.org/10.1093/biomet/69.3.635`.

[54] Yayun He et al. "Linear Boltzmann transport for jet propagation in the quark-gluon plasma: Elastic processes and medium recoil". In: *Physical Review C* 91.5 (May 2015). DOI: `10.1103/physrevc.91.054908`. URL: `https://doi.org/10.1103/physrevc.91.054908`.

[55] Ulrich Heinz and Raimond Snellings. "Collective Flow and Viscosity in Relativistic Heavy-Ion Collisions". In: *Annual Review of Nuclear and Particle Science* 63.1 (Oct. 2013), pp. 123–151. DOI: `10.1146/annurev-nucl-102212-170540`. URL: `https://doi.org/10.1146/annurev-nucl-102212-170540`.

[56] Ernst Hellbär. *The ALICE TPC: Optimization of the Performance in Run 2 and Developments for the Future.* 2019. DOI: `10.48550/ARXIV.1909.03746`. URL: `https://arxiv.org/abs/1909.03746`.

[57] *History of the Universe Poster.* 2014. URL: `https://particleadventure.org/history-universe.html`.

[58] John E. Huth et al. "Toward a standardization of jet definitions". In: *1990 DPF Summer Study on High-energy Physics: Research Directions for the Decade (Snowmass 90)*. Dec. 1990, pp. 0134–136.

[59] Raphaëlle Ichou and David d'Enterria. "Sensitivity of isolated photon production at TeV hadron colliders to the gluon distribution in the proton". In: *Phys. Rev. D* 82 (1 July 2010), p. 014015. DOI: `10.1103/PhysRevD.82.014015`. URL: `https://link.aps.org/doi/10.1103/PhysRevD.82.014015`.

[60] Barbara V. Jacak and Berndt Müller. "The Exploration of Hot Nuclear Matter". In: *Science* 337.6092 (2012), pp. 310–314. DOI: `10.1126/science.1215901`. eprint: `https://www.science.org/doi/pdf/10.1126/science.1215901`. URL: `https://www.science.org/doi/abs/10.1126/science.1215901`.

[61] Zi-Wei Lin et al. "Multiphase transport model for relativistic heavy ion collisions". In: *Physical Review C* 72.6 (Dec. 2005). DOI: `10.1103/physrevc.72.064901`. URL: `https://doi.org/10.1103/physrevc.72.064901`.

[62] Ewa Lopienska. "The CERN accelerator complex, layout in 2022. Complexe des accélérateurs du CERN en janvier 2022". In: (2022). General Photo. URL: `https://cds.cern.ch/record/2800984`.

[63] Antonin Maire and David Dobrigkeit Chinellato. "ALICE sub-detectors highlighted (LHC runs 1+2 // runs 3+4)". General Photo. 2017. URL: `https://cds.cern.ch/record/2302924`.

[64] Michael L. Miller et al. "Glauber Modeling in High-Energy Nuclear Collisions". In: *Annual Review of Nuclear and Particle Science* 57.1 (2007), pp. 205–243. DOI: `10.1146/annurev.nucl.57.090506.123020`. eprint: `https://doi.org/10.1146/annurev.nucl.57.090506.123020`. URL: `https://doi.org/10.1146/annurev.nucl.57.090506.123020`.

[65] Gavin P. Salam. "Towards jetography". In: *The European Physical Journal C* 67.3-4 (May 2010), pp. 637–686. DOI: `10.1140/epjc/s10052-010-1314-6`. URL: `https://doi.org/10.1140/epjc/s10052-010-1314-6`.

[66] Björn Schenke, Charles Gale, and Sangyong Jeon. "MARTINI: An event generator for relativistic heavy-ion collisions". In: *Phys. Rev. C* 80 (5 Nov. 2009), p. 054913. DOI: `10.1103/PhysRevC.80.054913`. URL: `https://link.aps.org/doi/10.1103/PhysRevC.80.054913`.

[67] Torbjörn Sjöstrand, Stephen Mrenna, and Peter Skands. "A brief introduction to PYTHIA 8.1". In: *Computer Physics Communications* 178.11 (June 2008), pp. 852–867. DOI: `10.1016/j.cpc.2008.01.036`. URL: `https://doi.org/10.1016/j.cpc.2008.01.036`.

[68] P. Skands, S. Carrazza, and J. Rojo. "Tuning PYTHIA 8.1: the Monash 2013 tune". In: *The European Physical Journal C* 74.8 (Aug. 2014). DOI: `10.1140/epjc/s10052-014-3024-y`. URL: `https://doi.org/10.1140/epjc/s10052-014-3024-y`.

[69] Ole Tange. *GNU Parallel 2018*. Ole Tange, Mar. 2018. ISBN: 9781387509881. DOI: `10.5281/zenodo.1146014`. URL: `https://doi.org/10.5281/zenodo.1146014`.

[70] Arturo Tauro. "ALICE Schematics". General Photo. 2017. URL: `https://cds.cern.ch/record/2263642`.

[71] *Technical proposal: L3*. Tech. rep. 1983. URL: `https://cds.cern.ch/record/297266`.

[72] Mark Thomson. *Modern particle physics*. New York: Cambridge University Press, 2013. ISBN: 978-1-107-03426-6.

[73] *TWiki - ALICE EMCal Trigger Offline*. Mar. 2021. URL: `https://twiki.cern.ch/twiki/bin/viewauth/ALICE/EMCalTriggerOffline`.

[74] *TWiki - ALICE Trigger Coordination*. Dec. 2020. URL: `https://twiki.cern.ch/twiki/bin/viewauth/ALICE/TriggerCoordination`.

[75] Xin-Nian Wang and Yan Zhu. "Medium Modification of γ-jets in High-Energy Heavy-Ion Collisions". In: *Physical Review Letters* 111.6 (Aug. 2013). DOI: `10.1103/physrevlett.111.062301`. URL: `https://doi.org/10.1103/physrevlett.111.062301`.

[76] J. Wenninger. "Machine Protection and Operation for LHC". In: (Aug. 2016). DOI: `10.5170/CERN-2016-002.377`.

[77] J. Wenninger. "Machine Protection and Operation for LHC". In: (Aug. 2016). DOI: 10.5170/CERN-2016-002.377.

[78] Korinna Zapp. "JEWEL 2.0.0: directions for use". In: *The European Physical Journal C* 74.2 (Feb. 2014). DOI: 10.1140/epjc/s10052-014-2762-1. URL: https://doi.org/10.1140/epjc/s10052-014-2762-1.

[79] Korinna Zapp et al. "A Monte Carlo model for 'jet quenching'". In: *The European Physical Journal C* 60.4 (Mar. 2009). DOI: 10.1140/epjc/s10052-009-0941-2. URL: https://doi.org/10.1140/epjc/s10052-009-0941-2.

[80] Wenbin Zhao et al. "From Hydrodynamics to Jet Quenching, Coalescence, and Hadron Cascade: A Coupled Approach to Solving the $R_{AA} \otimes v_2$ Puzzle". In: *Physical Review Letters* 128.2 (Jan. 2022). DOI: 10.1103/physrevlett.128.022302. URL: https://doi.org/10.1103/physrevlett.128.022302.

[81] Ren-Yuan Zhu. "A Very Compact Crystal Shashlik Electromagnetic Calorimeter for Future HEP Experiments". In: *Journal of Physics: Conference Series* 928 (Nov. 2017), p. 012015. DOI: 10.1088/1742-6596/928/1/012015. URL: https://doi.org/10.1088/1742-6596/928/1/012015.

[82] P.A. Zyla et al. "Review of Particle Physics". In: *PTEP* 2020.8 (2020). and 2021 update, p. 083C01. DOI: 10.1093/ptep/ptaa104.